FACULDADE DE ENGENHARIA DA UNIVERSIDADE DO PORTO

# Development of a Railway Traction Control Unit

**Pedro Azevedo Moço**

Mestrado em Engenharia Eletrotécnica e de Computadores

Supervisor: Prof. Doutor Agostinho Manuel Afonso da Rocha

July 1, 2022

# Resumo

A União Europeia navega pelo século XXI com uma grave crise climática, sendo forçada a introduzir mudanças para aliviar as consequências e, simultaneamente, reduzir a pegada carbónica dos seus estados membros. Uma das medidas amplamente adotada é a aposta do transporte ferroviário, considerado por muitos o modo de transporte mais ecológico, devido ao seu baixo atrito de rolamento, economias de escala e eletrificação simplificada. Muitos operadores de comboios europeus têm vindo a recorrer à renovação das suas frotas de modo a aumentar a vida útil e melhorar os seus desempenhos. É neste contexto que foi proposto ao mestrando, por parte da *Nomad Tech*, o desenvolvimento de uma atualização da Unidade de Controlo de Tração (UCT) da série 2300/2400 da *Siemens*, cujas unidades tipicamente circulam numa das linhas mais ocupadas de Portugal, a linha de Sintra, onde a pontualidade e fiabilidade dos comboios é de grande relevo.

Os objetivos principais da dissertação são a identificação, modelação e simulação de uma UCT, bem como as suas leis de controlo. De seguida, a implementação das mesmas num microcontrolador, adaptado ao uso em ambiente ferroviário, permite a validação experimental do esquema de controlo desenvolvido. As atuais medições e ferramentas de atuação/interfaces têm de ser mantidas, de modo a garantir a retro compatibilidade do sistema. Como resultado do trabalho desenvolvido, o comboio deve melhorar a sua eficiência energética, empregando um CPU moderno com novas leis de controlo implementadas.

Através do estudo teórico de simulação da cadeia de tração com as novas leis de controlo, foi alcançado um controlo de binário adequado ao ambiente ferroviário. Para tal, foi necessário ajustar o controlo de corrente da máquina de indução, cujos resultados são considerados sólidos. As estimações de fluxo e binário foram também fulcrais para o alcançar dos objetivos delineados. O passo seguinte da dissertação, a validação experimental, permitiu demonstrar o emprego do esquema de controlo num ambiente físico, através do controlo de corrente com sucesso numa carga passiva.

Em suma, pela realização da dissertação, foi delineado um caminho claro e sustentado para a ultrapassagem do problema da obsolescência, através da arquitetura de controlo realizada e validada, tanto em simulações como em ambiente prático.

# Abstract

As the European Union drives through the 21st century with a grave climate change issue, it is forced to take measures to alleviate its consequences, as well as to drastically reduce its member states' carbon footprint. One of the measures being widely adopted is the return of the railway, considered by many the most ecological way of transportation, due to its low rolling friction, economies of scale and easy electrification. Many train operators in the EU have been resorting to refurbishment of their trains in order to obtain longer lifespans and performance gains. It is in this context that the student was asked, by *Nomad Tech*, to develop a Traction Control Unit (TCU) overhaul for the *Siemens* Series 2300/2400, whose usual running area is one of the busiest lines in Portugal, Sintra line, where punctuality and reliability of trains is of the upmost importance.

The main objectives of the dissertation are the modeling, identification and simulation of a TCU, together with its control laws. Nextly the portability of these to a microcontroller, adapted to railway usage, allows the experimental validation of the control scheme developed. It should be noted that the present measuring and actuating tools/interfaces must be kept, with the objective of maintaining the retro compatibility of the system. As a result of the work developed, the train should improve its energy efficiency and passenger comfort, whilst having a modern CPU with the new control laws implemented.

Through the theoretical simulation studies of the traction chain with the new control laws, a torque control scheme adequate to the railway environment was achieved. To accomplish this, it was necessary to adjust the current control of the induction machine, whose results are considered solid. The flux and torque estimations were also essential to the realisation of the objectives. The next step in the dissertation, the experimental validation, allowed to demonstrate the employment of the control scheme onto a physical environment, through the successful current control in a passive load.

Concluding, through the development of the dissertation, a clear and demonstrated path was laid on to overcome the obsolescence issue, as a result of the successfully developed and validated control architecture, in simulations and physical evaluations.

# Agradecimentos

Em primeiro lugar, tenho de agradecer a todos aqueles que lidaram comigo no dia-a-dia deste período tão fulcral do meu percurso pessoal. À minha família, à minha namorada e aos amigos que sempre me ajudaram a todos os níveis, seja com umas palavras de encorajamento ou com uma bela jantarada.

Aos meus orientadores, Agostinho e Vítor, por toda a atenção e cuidado que tiveram com o projeto, e por toda a motivação transmitida. Ao meu parceiro de trabalho, Rui, além dos "finos", devo um obrigado. Também tenho de agradecer à *Nomad Tech* por todo o apoio fornecido; houve sempre uma postura de total compreensão e ajuda por parte de todos os colegas com quem eu tive a oportunidade de partilhar momentos.

Pedro Moço

*"The saddest aspect of life right now is that science gathers knowledge faster than society gathers wisdom"*

Isaac Asimov

# Contents

# List of Figures

# List of Tables

# Abreviaturas e Símbolos

| | |
|---|---|
| AC | Alternating Current |
| ADC | Analog to Digital Converter |
| CP | Comboios de Portugal |
| CPU | Central Processing Unit |
| DB | Deutsche Bahn |
| DC | Direct Current |
| DCM | Direct Calculation Method |
| DFOC | Direct Field Oriented Control |
| DTC | Direct Torque Control |
| EKF | Extended Kalman Filter |
| EMF | Electromotive Force |
| EMI | Electromagnetic Interference |
| EMU | Electrical Multiple Unit |
| FIR | Finite Impulse Response |
| FOC | Field Oriented Control |
| FSM | Finite State Machine |
| GTO | Gate Turn Off |
| IDE | Integrated Development Environment |
| IFOC | Indirect Field Oriented Control |
| IGBT | Insulated Gate Bipolar Transistor |
| IIR | Infinite Impulse Response |
| IM | Induction Machine |
| LPF | Low-Pass Filter |
| MPTC | Model Predictive Torque Control |
| MRAS | Model Reference Adaptive System |
| MTPA | Maximum Torque per Ampere |
| PCB | Printed Circuit Board |
| PI | Proportional-Integral |
| PMSM | Permanent Magnet Synchronous Motor |
| PWM | Pulse-Width Modulation |
| SHE | Selective Harmonic Elimination |
| SiC | Silicon Carbide |
| SVM | Space-Vector Modulation |
| SVPWM | Space-Vector Pulse Width Modulation |
| SYNRM | Synchronous Reluctance Motor |
| TCU | Traction Control Unit |
| THD | Total Harmonic Distortion |
| UCT | Unidade de Controlo de Tração |
| VSI | Voltage Source Inverter |

# Chapter 1

# Introduction

## 1.1 Context of the Dissertation

In a context of increased railway utilisation in both people and goods transportation, and considering the recent technological evolutions made in power electronics, signal processing and microprocessors, it is only reasonable to assume that the railway sector must be keeping up with the industry. Several key upgrades include, but are not limited to, semiconductor design process maturation and increased processing capability in mobile and industrial CPUs. Furthermore, it is of the utmost importance to lower the running costs of the trains (by reducing energy consumption and decreasing the costs related to maintenance) for a strong and healthy competition between road and air transportation modes, the latter considered to be highly inefficient and polluting.

In the case being studied, trains from *CP Series 2300/2400* are being due to a "half-life" revision, where a large number of components are replaced, namely the traction motors and converters. It was found that the TCUs of the trains are antiquated, and no longer sold on the market. Therefore, there is a necessity to replace these components with newer technologies, to avoid shortening the life-span of the trains.

## 1.2 Main goals of the project

Introduced by *Nomad Tech* jointly with FEUP, the topic of the dissertation includes a few main objectives with the accomplishment of the project:

- Analysis of a railway Traction Control Unit (TCU) chain, and its main requirements;
- Definition of the dynamic model of the system, by the study of the traction motor, as well as the Voltage Source Inverter and the control laws;
- Implementation and simulation of the traction chain with the new control laws developed;
- Experimental validation of the control scheme developed.

## 1.3 Structure of the Document

The following items are discussed in this document:

- In chapter **2**, a review of the State of Art related to Traction Control Units is done. In it an overview of the different options for traction motors is presented and anti-slip control techniques are described. Moreover, the general electrical structure of an electric train is shown, with an emphasis on the components of which a TCU is made up of; a detailed and comprehensive analysis is made regarding the main control laws families applied in a railway scenario. Lastly, sensorless control and speed estimation techniques are approached, as well as the essential modulation techniques.

- In chapter **3**, a theoretical background of the concepts explored during the dissertation development is presented. Firstly, a brief examination over the current Traction Control Unit in the train unit to be refurbished is reported; afterwards, a study on IM modelling is presented. The control method FOC is detailed and explained, as well as the SVPWM technique, essential in these types of motor drives. At last, some mechanical considerations regarding the traction resistive forces are exposed, and a theoretical background in regard to thermal studies of the semiconductors is delineated.

- Chapter **4** details the simulation work developed. First of all, the subsystems used for the simulations are specified, namely the IM simulation block. Then, the control architecture was defined, and the basis for the thermal studies laid upon. At last, the results regarding current and torque control of the IM are presented and discussed; in addition, the thermal studies results are also shown.

- Chapter **5** describes the procedures for the experimental validation of the control scheme. The test bench is detailed, as well as the microcontroller programming, including digital filters and interrupts configuration. Afterwards, the acquisition tests are presented, together with a SVPWM test. Lastly, the current control results are exhibited and discussed.

- The last chapter in this document, **6**, summarises the works developed, and gives an insight into future possible developments of the topics addressed.

# Chapter 2

# Literature Review

## 2.1 Railway Motors

Ever since the systemic abandonment of steam engines as the main workhorse for the railway industry, the electric motor has been the main solution to operators worldwide, where electrified lines are available. In the rest of cases, the diesel-electric power cars reign the rails. There are some hybrid solutions, employing both diesel-electric and pure electric motors, that use the pantograph to feed the main transformer where the catenary is available, and the fossil fuel engine for the other areas. Currently, since the industry is moving in the direction of decarbonization, some solutions for *last-mile* traction have been developed, such as battery electric trains, or even hydrogen ones. Some typical performance requirements of traction motors include power under 1000 kW, at 3000 rpm, [1].

### 2.1.1 Direct Current Motor

From over a century, and up until the 1990s, the DC motor was the most used propulsion system, due to its high torque from low speeds and simple control methods, [2]. A lot of research was done on these motors in order to increase compactness and reliability, with success. However, the high maintenance requirements due to the brushes degradation over time and the trouble to obtain a spark-free commutation over the full speed and torque range, [3], has lead the industry to develop Alternating Current solutions.

### 2.1.2 Alternating Current Motor

#### 2.1.2.1 Induction Motor

The dominant technology in railways nowadays is the Induction Motor. Its mechanical robustness, coupled with its good capability of overloading, low cost and mature technology, [3], forced its widespread utilisation. Moreover, the minor, if nonexistent, maintenance demands put pressure on the DC motor reign.

An IM is fed AC current in their stator windings, which due to their strategic placement generate a rotating magnetic field. This field interacts with the rotor conductors, and induces currents, that in their turn generate a magnetic field which opposes the one generated by the stator. The interaction between these two fields generates electromagnetic torque at the rotor. Additionally, the rotor field always rotates at a different speed as of the stator field, this characteristic being named as slip.

There is a possibility to feed two to four motors with each inverter, resulting in lower costs and weight of the application. This can happen due to the intrinsic slip characteristics of these machines, enabling them to compensate different wheel speeds due to defective wheel diameters (as a result of degradation, for example). A characteristic system designers must be aware of is the material of the rotor cage. It can either be made of copper or aluminium; the copper counterpart exhibits less Ohmic losses, thus needing less ventilation. However, its higher cost may force some systems to use aluminium. If the motor has a fully or semi-closed design, with lower self-ventilation properties, then the lower power losses of the copper are necessary. For example, light rail vehicles are usually of a low-floor topology, forcing the motors to be closer to the ground, and more exposed to the environment characteristics. As a result, a closed or semi-closed motor is desirable, therefore forcing the lower rotor losses with the copper conductors, [1].

#### 2.1.2.2 Permanent Magnet Synchronous Motor

While the gross of the market is keen on IMs, some solutions have been developed with Permanent Magnet Synchronous Motors (PMSM), namely in High-Speed Rail (HSR) and also Light Rail. This type of synchronous motor offers higher torque density, higher efficiency, and better power factor. but has a few drawbacks comparing it to the IM, such as the cost of the rare-earth materials used for the permanent magnet rotor, or the possibility of demagnetization by high currents and/or temperature, [1].

PMSMs do not need rotor external excitation since the use of the permanent magnets ensures the creation of the flux, as opposed to the IM. Since there are no induced currents in the rotor, Ohm losses are eliminated. Neodymium magnets are usual in railway applications, but their price uncertainty has led the industry to move away from these motors. Moreover, the inability to couple one or two pairs of motors to a single inverter increases costs, once again. However, requirements of great performance at all speed ranges in HSR trains still create some demand for PMSMs, [3]. An example of a High-Speed train using this type of motor is Italo's AGV, manufactured by Alstom, [4]. Some Light Rail vehicles in Japan also employ the PMSM.

#### 2.1.2.3 Synchronous Reluctance Motors

The Synchronous Reluctance Motor (SYNRM) is one of the great advancements in recent motor technology. It replaces the rotor losses present in the rotor of the IM, and the rare-earth magnets in the PMSM for a complex rotor design, shown in figure 2.1. However, even if rotor losses are removed, the SYNRM needs more current to fulfil the same torque as an equivalent IM, [5], thus increasing stator windings losses. Moreover, the control methods for this motor are more sophisticated compared to other motors mentioned. Nonetheless, SYNRM with permanent magnets is an emerging technology that can tackle some issues like efficiency and torque density, [6]. Nowadays, this motor is not employed in any railway application, but it is foreseeable that in the near future some solutions may appear.

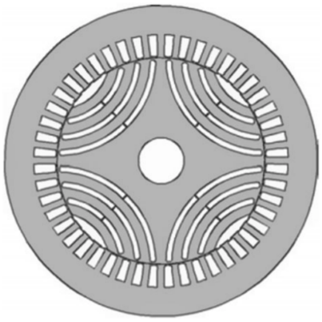

Figure 2.1: Profile view of a SYNRM structure. Extracted from [7].

### 2.1.3 Motor regions of operation

Typically, an electric motor presents three operation regions: one that corresponds to constant torque, one to constant power, and the last named as natural region. In figure 2.2, up until the end of the first region, which is delimited by the base speed, the motor delivers its rated torque, while running at its rated flux and current, since torque is proportional to those variables; its voltage must increase with a rise in speed, due to the increase of the back-emf, which must be countered. In the following region, the constant power region (which begins right after the base speed), the flux and torque must be diminished with an increase in speed. Torque decreases inversely with the rotor speed. This region is obtained in motors through the field-weakening operation. The last region, usually named natural region, or in the case of IMs, constant slip, sees a steeper reduction in torque and current, [8], [9].

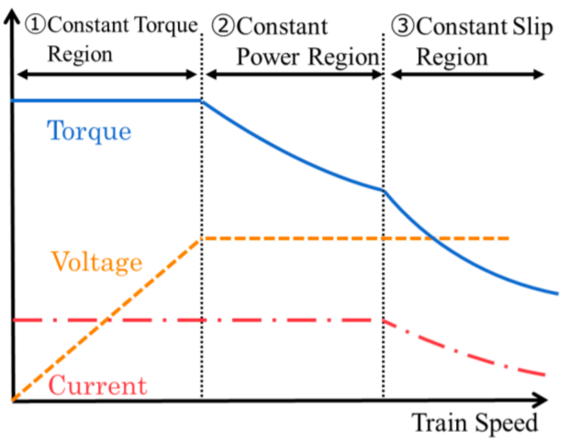


Figure 2.2: Typical torque-speed curve associated with an IM. Extracted from [9].

## 2.2 Anti-Slip Control

In order to maintain an adequate level of performance in breaking and traction, as well as avoiding damages to the wheels and rails, slip at the wheel-rail interface must be avoided at all costs. Historically, locomotives were equipped with sandboxes, which contained dry sand to be injected with compressed air at the wheel-rail junction in order to increase the grip of the wheel, [10]. Lately, modern electric locomotives incorporate more sophisticated methods of anti-slip detection and control, by the use of electronic circuitry and microprocessor control, whilst maintaining the sandboxes.

Firstly, a few theoretical concepts must be defined. Wheel slip velocity ($v_s$) is calculated using equation 2.1:

$$v_s = r_w \omega_w - v_t \tag{2.1}$$

Where $r_w$ is the radius of the wheel, $\omega_w$ the angular velocity, and $v_t$ the speed of the vehicle. Furthermore, the tangential force ($f_\mu$) is defined in figure 2.3.

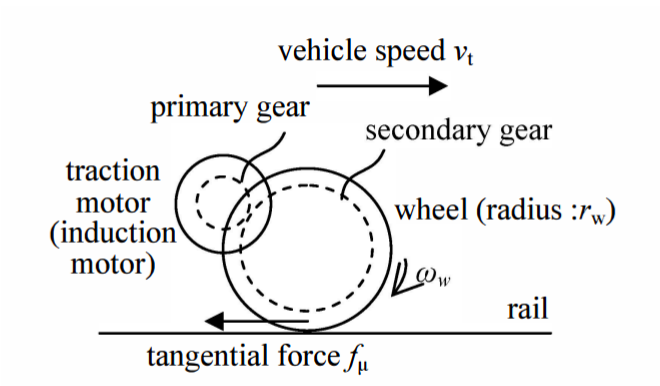


Figure 2.3: Scheme of the tangential force. Extracted from [11].

The same force can be obtained using equation 2.2:

$$f_\mu = \mu_a \cdot mg \tag{2.2}$$

Where $\mu$ is the adhesion coefficient, $m$ is the mass of the vehicle, and $g$ the gravitical acceleration. The best region for operation would be in the stable region, whilst maintaining the optimal slip velocity, corresponding to the maximum adhesion coefficient for the best tractive effort, [12]. Figure 2.4 plots a generic adhesion coefficient over different slip velocities, graphically showing the concepts regarded.

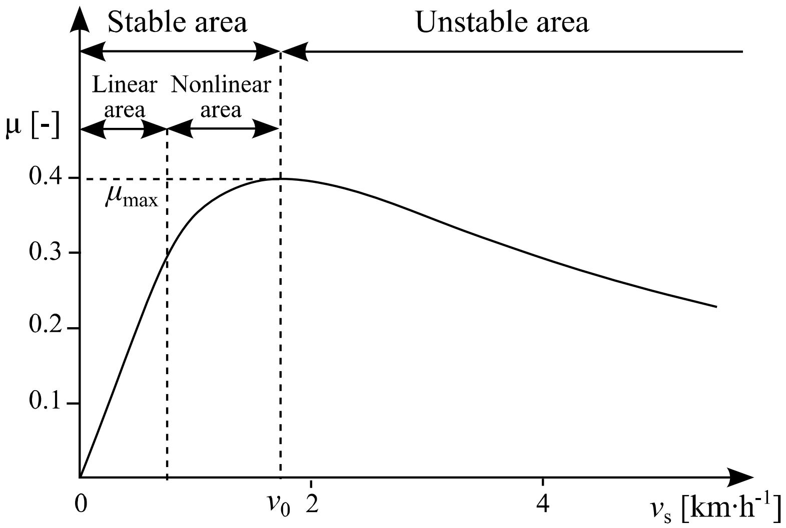


Figure 2.4: Plot showing correlation between wheel slip velocity and adhesion coefficient. Extracted from [12].

However, the correlation between speed and the coefficient is highly variable due to the external uncertainties of the environment of the track. For example, a wet rail presents a different optimal slip velocity. Also, the condition of the track and of the wheels will also impact this ratio. Thus, the optimal operating point cannot be calculated beforehand, and the only variable that is possible to be controlled is the slip velocity, which is controlled by the torque produced by the motor. Figure 2.5 displays different adhesion coefficients for different track conditions.

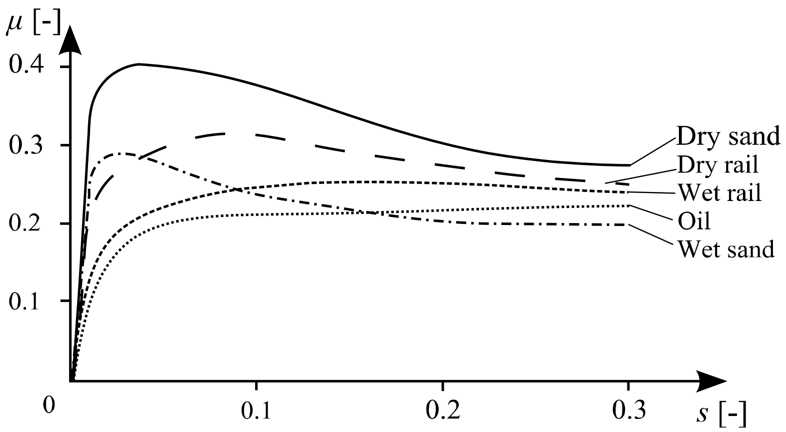


Figure 2.5: Different behaviours of the adhesion coefficient with different conditions. Extracted from [13].

In order to obtain the information if the train is suffering from slip, it is very important to obtain the exact speed of the train. The most obvious way to gather this value is through the measured angular speed, using an encoder, at a non-driven shaft, and to multiply it by the radius of the wheel being driven. However, most modern trains do not possess a "free" shaft, thus proving that this method is unpractical, [14]. To overcome this, the most used solution is to measure the speed of all of the driving axles of the train, or locomotive, and set the speed reference, $v_{ref}$, as the lowest value measured, **yuREADHESIONCONTROLRAILWAY**, [14], [15]. To obtain the slip velocity in a given wheel, equation 2.3 is used:

$$v_s = \omega r - v_{ref} \tag{2.3}$$

It is usual to set a threshold to determine when slip is happening. One of the most common ones is 0.1 km/h, however it can go up to 2 km/h, [15].

As a study for the state of art of anti-slip control methods, the following list will be presented:

- *Control of the Slip Velocity to a constant value*

  It is mostly still used in older DC motor locomotives, and is considered to be an obsolete method. The main operating characteristic is a fixed slip velocity, because it assumes that the maximum value of the slip coefficient happens at the same velocity, regardless of track condition or environmental status. Therefore, it is an unreliable method for slip control in modern railway applications, since the optimal slip speed chosen is not appropriate for all possible physical scenarios.

- *Search of the maximum value of the adhesion coefficient*

  This method is based on the search of the inflexion point of the slip velocity-adhesion coefficient graph. In order to obtain this, the tangential force is derivated; if the value of the derivation is positive, then the point analysed is in the stable region; if it is negative, then it can be concluded that the point is in the unstable region; lastly, if the derivative is zero, then the point is at the peak of the coefficient. However, this method may fail if the characteristic curve has a big plateau: in this case, the optimal point detected has higher than desired slip velocity, thus causing instability. Consequently, this method is usually used together with other methods, [13].

Other methods currently used by the industry involve the use of speed controllers to keep the slip speed at a certain value, thus controlling it at any desired range of the adhesion coefficient. Another approach is based on the determination of the adhesion-slip characteristic slope. To combine all of those mentioned into a well integrated system, it is frequent to use a hybrid method, that arbitrates the most suitable method based on the current slip level **yuREADHESIONCONTROLRAILWAY**, [13]. The method is illustrated at figure 2.6.

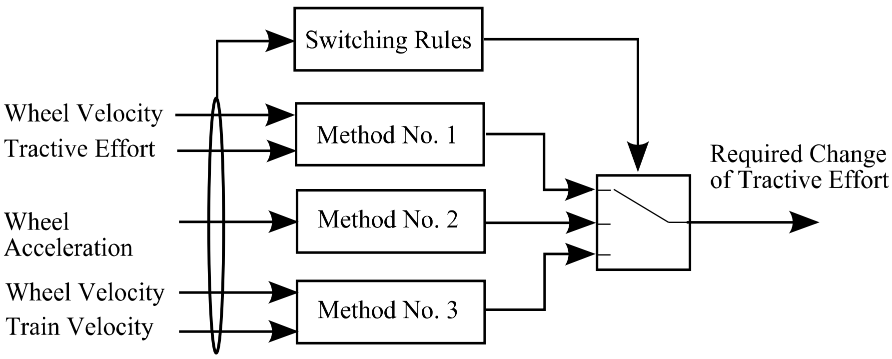


Figure 2.6: Block diagram of a hybrid anti-slip control method. Extracted from [13].

## 2.3 General Structure of the Train Electrical Scheme

Under this section, different electrical structures present in different train schemes will be presented and compared. It is relevant to have an idea of how the voltage passes from the catenary wire, through the pantograph and into the power converters. Additionally, a deeper overview will be made on the typical traction converter configuration, essential for the work to be developed, as well as its control unit. Finally, a remark on semiconductors is also presented.

### 2.3.1 Electric Locomotives

Typically, heavy-rail electric locomotives employ the scheme shown in figure 2.7a. The main high voltage is transformed to a lower voltage for the traction converter, through the main transformer. There are also a number of auxiliary converters used to feed secondary loads, such as battery chargers or air-conditioning units.

### 2.3.2 Electric Multiple Units

A prominent and rising in popularity solution in railways is the use of Electric Multiple Units (EMU). In opposition with the famous locomotive in conjunction with many carriages, the traction motors are distributed throughout the composition. This allows for more usable space inside the train, and lower reverse times, since there is a cabin at each end of the train.

Essentially, these trains are composed by a variable number of cars, namely motor coaches and trailling coaches. The high-voltage equipment is placed in a specific enclosure in motor coaches, and it is connected to the motors directly in the bogies. The axles on the remaining non-motor coaches are non-powered, [16].

One main difference between this topology and the locomotive is that the four-quadrant converter feeds a DC-to-DC converter, aside from feeding the traction inverter, that can also provide power to auxiliary loads, as can be observed in figure 2.7b. The traction converter ultimately feeds two motors, one per axle of the bogie, [16].

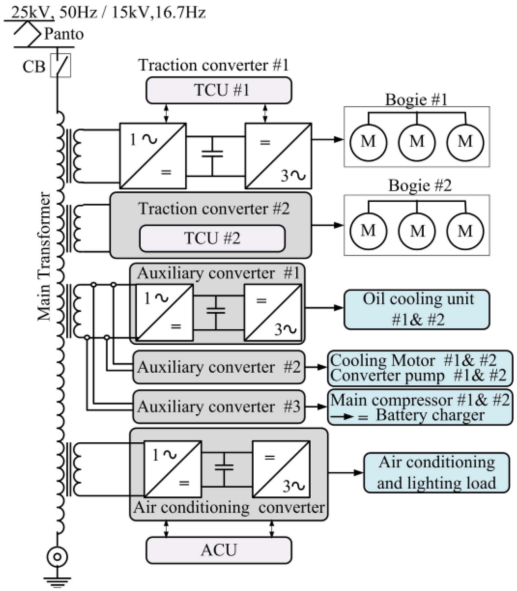


(a) Block diagram of a typical electric locomotive power structure. Extracted from [16].

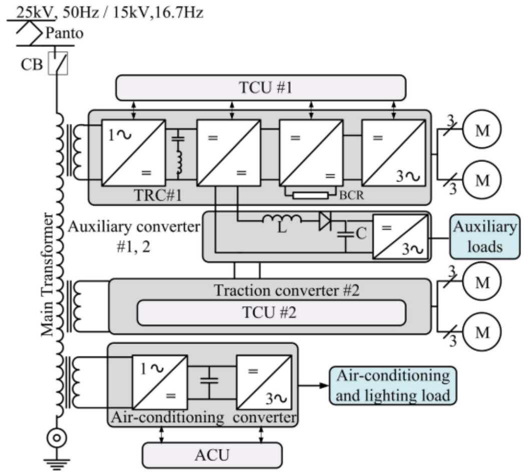


(b) Block diagram of a typical electric multiple unit power structure. Extracted from [16].

Figure 2.7: Block diagrams of electric locomotives and EMUs.

### 2.3.3 Traction Converter Topology

The traction converter usually employs the following stages in the design consideration:

- First phase: The main transformer converts the high-voltage obtained at the overhead lines by the pantograph;
- Second phase: The lower voltage is rectified; usually there is a DC link capacitor and a series resonant filter;
- Third phase: Three-phase inverter, used to drive traction motors;

The current is fed into a four-quadrant converter, that allows the rectification of the AC current, but also allows bidirectional power flow (for regenerative braking); then it is filtered through a series resonant circuit and a DC link capacitor; lastly, fed into a typically three-phase inverter, [16]. This traction circuit can then feed multiple IMs. The traction control unit controls the three-phase VSI, in order to obtain a certain speed or torque desired. It can also control the four-quadrant converter, with the objective of outputting the same DC voltage under pantograph voltage variations. In the scope of the dissertation, only the control of the VSI will be discussed. Figure 2.8 shows a typical block diagram of the said configuration.

Different manufacturers, such as ABB, Siemens or Alstom, apply diverse techniques in this end, such as different medium-frequency transformer operating frequencies or the use of modular multilevel converters in favour of cascaded H-bridges, [16].

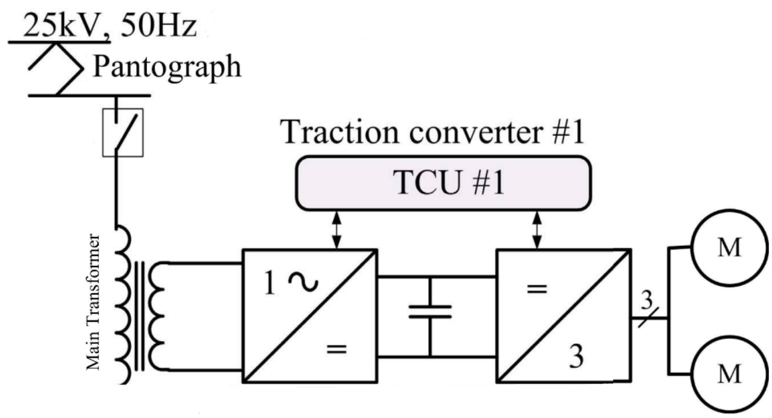


Figure 2.8: Block diagram of a typical traction converter topology. Adapted from [16].

### 2.3.4 Inverters and Semiconductors

In the field of semiconductors, the use of Gate Turn Off (GTO) thyristors was exceedingly common in railway applications. Aside from removing the constant maintenance issue that the DC motor's brushes brought, in the case of AC motors, the inverters using this technology, coupled with Pulse-Width Modulation (PWM) control of microcontrollers, increased the power factor of the feeding circuit, putting it close to 1.0, thus increasing the amount of active power delivered to the motors, [17].

Whilst proving to be a revolution in the Power Electronics field, GTO semiconductors did have a few disadvantages such as low switching frequency (typically up to 500Hz), complex gate driving circuits and a low reliability record, [16]. In the 2000's, Insulated Gate Bipolar Transistor (IGBT) based semiconductors proved themselves to be a second revolution in the field. They offered higher switching frequencies (up to 2kHz), lower switching losses, package footprint and simpler gate electronics, [16], [17].

The current trend in the field is to increase the power density and efficiency of the converters even further. IGBT based power devices face the issue of poor performance at higher temperatures, thus requiring more sophisticated cooling solutions. This has led the industry to follow the development of Silicon Carbide (SiC) as a wide-bandgap material. Semiconductors using this technology are able to work with a higher breakdown voltage, thus enabling the reduction in thickness of the body diode, resulting, in theory, lower running resistance on them, [18]. These advantages can be seen in figures 2.9 and 2.10.

Currently, the use of SiC-based anti-parallel body diode in conjunction with IGBT semiconductors, usually named as a hybrid solution, poses a serious alternative to pure IGBT configurations, due to their lower switching losses as compared to a pure IGBT solution. However, SiC semiconductors devices in a standalone configuration cannot be employed, since they are still in their infancy stage of development, and their maximum voltages do not yet reach the standards needed for rail technology. It could be said, however, that due to the promising results shown,

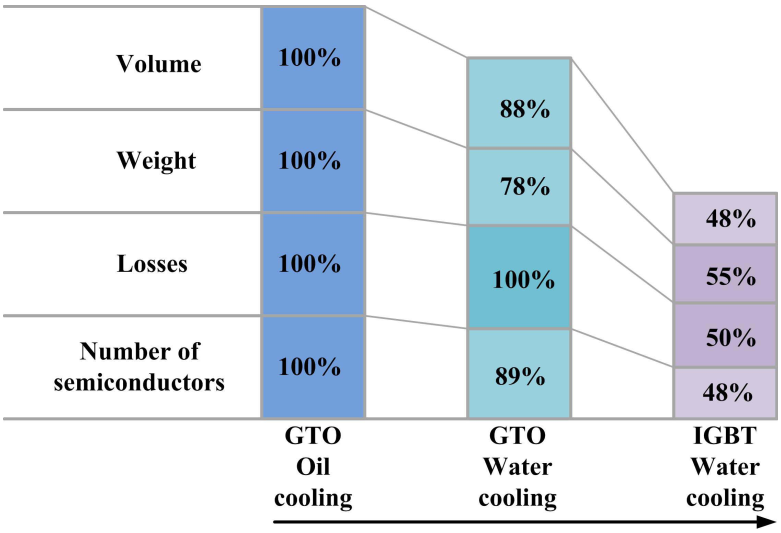


Figure 2.9: Image depicting the evolution from GTO to IGBT. Extracted from [16].

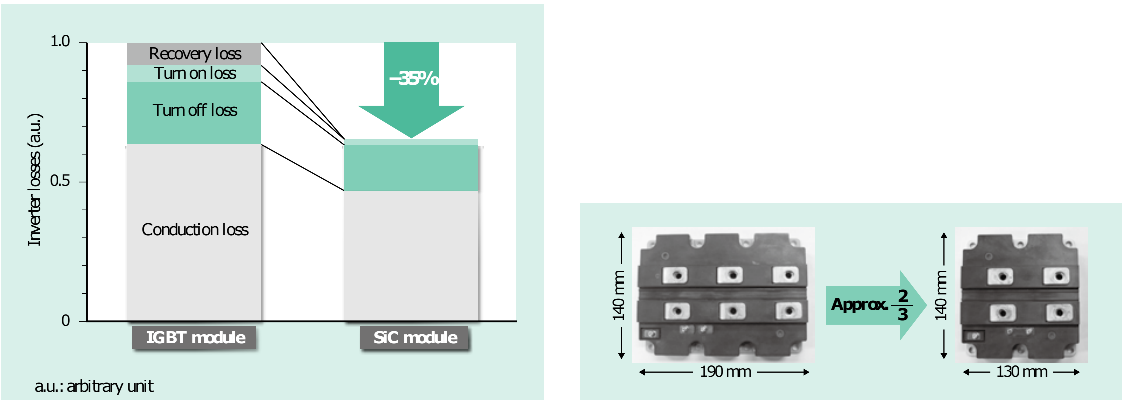


(a) Losses reduction of SiC based solutions over IGBT based ones.

(b) Size difference of SiC based solutions over IGBT based ones.

Figure 2.10: Illustration of the advantages of SiC based solutions. Extracted from [18].

after the voltage restrictions are overpast, a big portion of the market can be shifted towards this kind of semiconductor technology.

### 2.3.5 Traction Control Unit

Usual motor drive applications utilise cascaded control loops in order to obtain the different desired performance set-points given by the user, in this case the train driver. In figure 2.11, a direct torque reference is sent to the control module, which will ensure the motor will develop it. However, a speed controller can be used, where a speed command is received and compared against its current value, and a torque command is generated by it. The slip controller can also influence the torque reference sent.

The Flux Selection block creates a flux command based on different techniques that can be applied, such as Maximum Torque per Ampere (MTPA). Operation in high speed leads to a much higher back-electromotive force, which in itself requires running the motor at a reduced torque. Flux weakening, for example, could be processed in this control stage. The inner control loops transform the torque and flux commands, together with the measurements needed from the motor, into voltage commands, that will be modulated for semiconductor switching in the VSI, [8].

The drive must comply with different requirements set by the manufacturer. In terms of performance, torque-speed characteristic, maximum speed and torque can be imposed; some requirements like the efficiency of the inverter and motor, operating temperatures and others may influence the performance of the electric drive; lastly, the fulfilment of the imposed norms with regard to electromagnetic interference of even acoustic noise levels, [8], must be considered in the design phase of the drive. However, many of these requirements can induce conflicts, such as the case of the operating temperature. VSI losses can be reduced by a reduction of the switching frequency; this can also lead to higher current ripples and subsequent torque ripples, that can produce undesired electromagnetic interference and even reduced passenger comfort, [8]. As a result, many compromises between requirements must be made, and systems designers must take a careful look into how to manage all of the trade-offs.

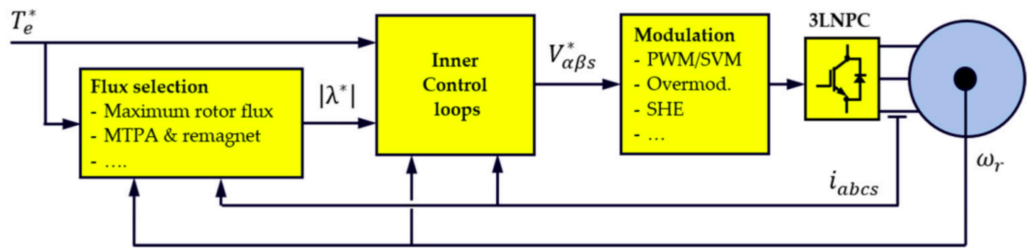


Figure 2.11: Generic cascaded control loops for a traction motor drive. Extracted from [8].

## 2.4 Traction Motor Control

The evolution of Electric Drives has been deeply influenced by the *state-of-art* of semiconductor and microprocessing technologies. In the early days of motor control, the most used solutions were DC motors coupled with analogical voltage regulation circuits for easy rotor speed variation. However, the DC motor suffers from degrading performance in harsh environments, and constant maintenance requirements due to its inherent build with the brushes deteriorating constantly during operation, [19]. As such, there was demand from industry and scientific community to develop AC motor drives. The advancements in semiconductor technology led to more complex solutions, ranging from simple voltage over frequency variations to methods applying Artificial Intelligence or meta-heuristic algorithms. In this section, a brief overview of the most used control methods will be done, along with their advantages and disadvantages.

### 2.4.1 Scalar Control

The first method to be approached is also one of the oldest in motor control theory. They first arrived when microcontrollers available did not possess high frequency operation; consequently, it is relatively simple and computationally light, as an adaptation for the environment where it would perform. Scalar Control based methods rely on the motor steady-state equivalent circuit, and they work properly when dynamic changes to the operating conditions are slow, [8].

#### 2.4.1.1 V/F control

Firstly, this method was applied with an open-loop concept. Essentially, it varies the voltage and frequency of the supply of the stator, but maintains a constant ratio between those two, resulting in a constant flux. However, some drawbacks to this method include poor speed control precision due to slip (in the case of IMs), and in the case of any parameter variation, such as a DC voltage change or even a higher torque demand can modify the operating point of the motor, thus being too unreliable, [8].

A more reliable method, widely used in many simple motor control solutions, uses V/F methodology, but closes the loop by adding a speed controller, as shown in figure 2.12.

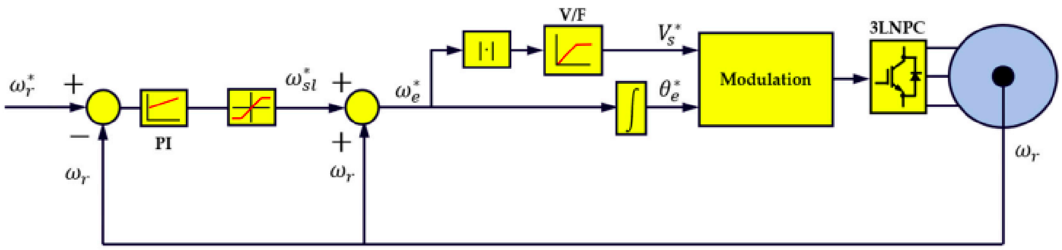


Figure 2.12: General topology for closed-loop V/F control. Extracted from [8].

### 2.4.2 Field Oriented Control

In the field of motor Vector Control, *Field Oriented Control* (FOC) is one of the most used methods. It is based on the principle that the electromagnetic torque and flux can be controlled independently, thus resembling the simple control of a DC motor. However, in the DC motor the brushes are assembled in a way that makes them permanently orthogonal to the magnetic field created by the permanent magnet, leading to the following torque equation 2.4.

$$T_e = K\psi_m i_a \tag{2.4}$$

By observing it, it is clear that the electromagnetic torque generated by the motor is directly proportional to the armature current, $i_a$, since the flux, $\psi$, is constant. To get a mathematically similar behaviour in an AC motor, a rotating reference must be applied. This method is computationally heavy, since a few complex mathematical operations must be performed thousands of times in a single second. The most essential operation is regarded as *Park and Clarke* transform, graphically illustrated in fig. 2.13. The mathematical equivalence is depicted in 2.5.

$$\begin{bmatrix} i_d \\ i_q \\ i_0 \end{bmatrix} = \begin{bmatrix} cos(\theta) & cos(\theta - \frac{2\pi}{3}) & cos(\theta + \frac{2\pi}{3}) \\ -sin(\theta) & -sin(\theta - \frac{2\pi}{3}) & -sin(\theta + \frac{2\pi}{3}) \\ \frac{1}{2} & \frac{1}{2} & \frac{1}{2} \end{bmatrix} * \begin{bmatrix} i_a \\ i_b \\ i_c \end{bmatrix} \tag{2.5}$$

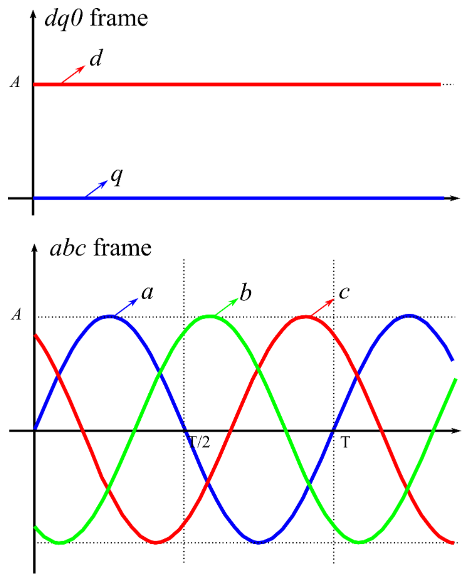


Figure 2.13: Visualisation of a Park-Clarke transform. Extracted from [20]

Commanded by the above equation, this methodology enables the transformation of a three-phase system (such as the currents in a stator of a three-phase motor) into a two-component system, of fixed quantities. The aforementioned components are named *direct* and *quadrature*. There are a few variations of the FOC method regarding its reference frame. In order to keep the *d-q* components of the current read from the stator windings as a scalar value, a rotating reference frame must be defined, since these values do not actually exist, but are a product of the *Park-Clarke* transformation. In essence, in an IM, there are three alternatives for this purpose: rotor flux, stator flux and air-gap flux, [21]. The most common method is the one using the rotor flux due to its simplicity, [22]. In this case, the *d-q* axis must be rotating at the speed of the rotor flux linkage, and the d-axis will be aligned with the position of the rotor flux linkage vector, [21]. Additionally, it is the most well documented and researched variation.

In figure 2.14, the general topology of this method exemplifies the usual strategy used in this type of application. Stator currents are measured and transformed to the rotating reference frame; the direct and quadrature currents are controlled, commonly using PI controllers, according to their commands. After this, they are transformed once more to a three-phase system from the *d-q* frame, where they control the gating signals for the PWM inverter that feeds the motor.

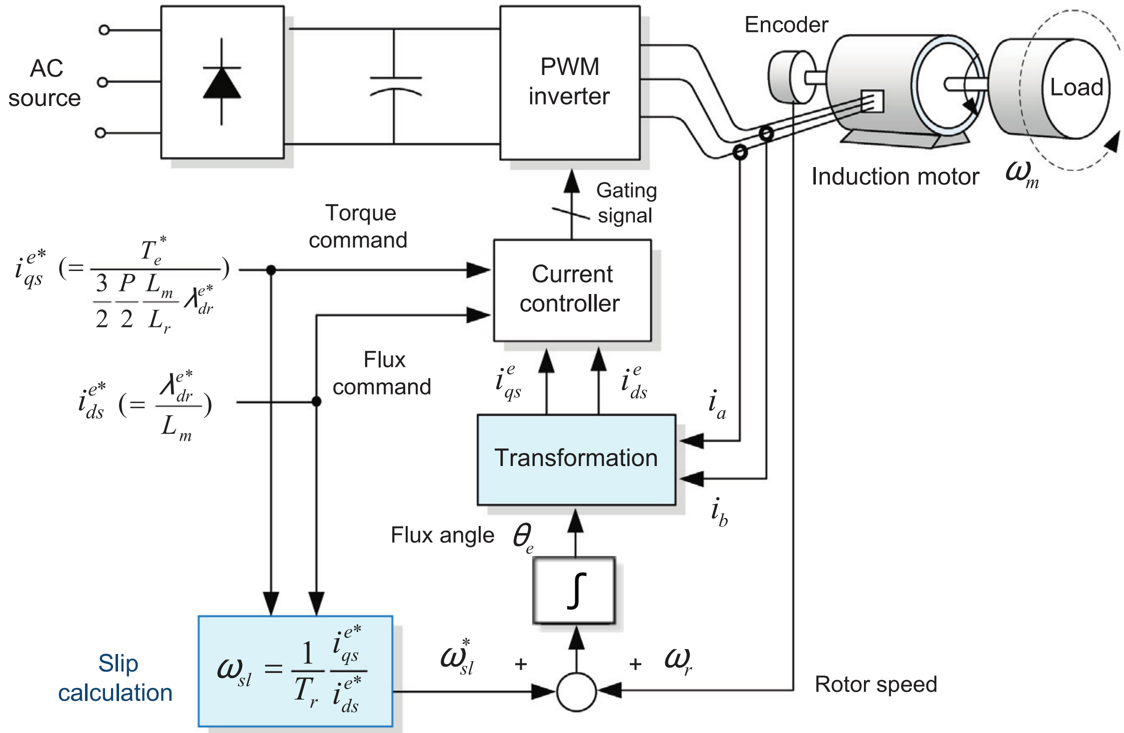


Figure 2.14: General topology of a Rotor Field Oriented Control (RFOC) method. Edited from [21].

As can also be seen at figure 2.14, the direct and quadrature stator current components control the flux linkage and the electromagnetic torque produced by the motor, respectively. One usual application for torque is the employment of cascaded control, with an outer speed controller comparing actual and reference speeds, and generating a torque command for the quadrature current controller.

In equation 2.5, it can be noted that the theta angle is of the utmost importance to the attainment of an accurate reference transformation, with obvious performance degradation in case of poor angle attainment. There are multiple ways to obtain this parameter.

According to the method of speed/position obtainment, FOC can be classified in different approaches. Direct FOC (DFOC) obtains the rotor position directly by means of a flux sensor (for example, a Hall effect sensor or optical rotor position), or by estimation means. However, in practical terms, the employment of a sensor is not practical due to the device requiring space, thus increasing the overall system size, and its reliability issues, [21], [23]. Due to the naming complexity presented in different sources, as well as a lack of standardisation in industry, figure 2.15 is presented to establish the different FOC variants.

Indirect FOC (IFOC) uses the mechanical rotor and slip angular speeds to obtain the flux angle. By summing these two terms, and integrating them over time, one can obtain the angle. To obtain the slip, a *feed-forward* of the stator *d-q* currents is necessary; additionally, the rotor time constant is also used:

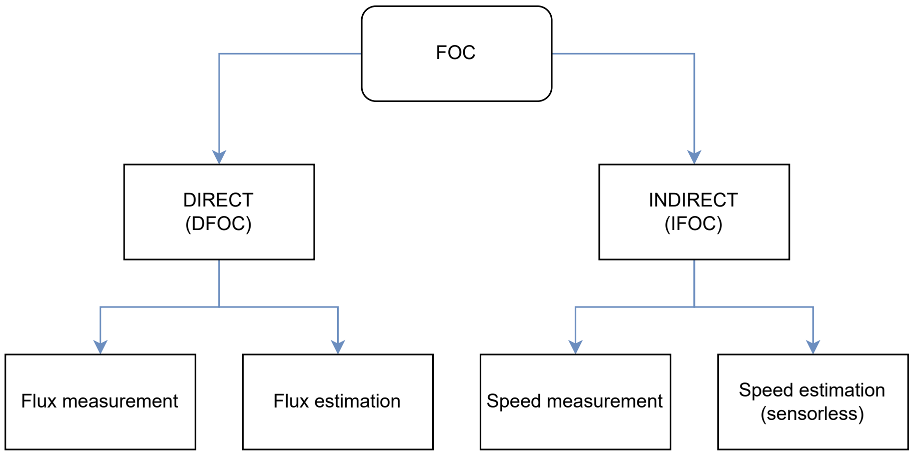


Figure 2.15: Diagram clarifying the different FOC variations.

$$\omega_s = \frac{1}{T_r}\frac{i_{qs}^e}{i_{ds}^e} \tag{2.6}$$

$$\theta = \int \omega dt = \int (\omega_s + \omega_r)dt \tag{2.7}$$

The obtainment of the speed can be done by an encoder or resolver placed on the motor shaft. This sensor, as the case with DFOC, is costly, somewhat unreliable and increases the cost and complexity of the system. To counter this, recent approaches to obtain the angular speed using estimation techniques have been gaining traction, usually named as *sensorless* techniques. This will be explored in section 2.5.

A frequent criticism of IFOC is due to the inherent characteristic that the model depends on the machine equivalent resistances and inductances. More specifically, the estimated rotor flux angle depends on the rotor time constant, that is due to variation by a natural temperature increase of the conductors. As such, if there is not an online parameter estimation adaptation, the method can suffer from significant angle deviation, resulting in poor speed and torque precision, [21].

DFOC and IFOC can be compared regarding their performance. Whilst IFOC can draw better speed performance at low speeds, DFOC is more suited for base speed operation, [23]. With regards to the use of sensors or estimation, [24] has found that sensorless operation can be adequate for a railway usage. However, it was also found that sensored operation saved a significantly higher amount of energy as compared with the speed estimation variant used, particularly in the regenerative braking quadrant.

FOC is very common in different train traction applications, namely in HSR, in the speed region under the base speed, due to its issues in high-speed operation, such as the lack of voltage margin in the inverter, and distortions in the currents as a result of overmodulation, [21].

### 2.4.3 Direct Torque Control

It is possible to write the electromagnetic torque of an IM as equation 2.8.

$$T_e = \frac{L_m}{\sigma L_s L_r} \lambda_s \lambda_r sin(\delta) \tag{2.8}$$

And, if the stator resistance is neglected, the stator flux is equal to the stator voltage integrated over time, [8]. As such, it can be seen that the torque can be controlled by the stator flux magnitude, as well as the angle $\delta$, which represents the angle between stator current and rotor flux, as seen in figure 2.16.

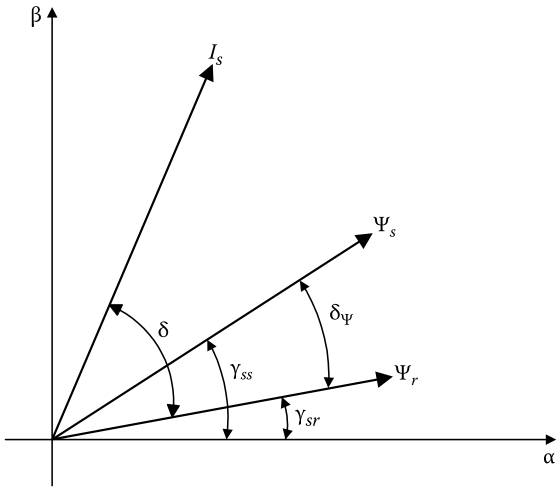


Figure 2.16: Reference frame of an IM in $\alpha - \beta$ coordinate system. Extracted from [22].

Essentially, this control methods works by comparing torque and stator flux magnitude references to their estimated values. To obtain the last two, estimators are used. The output of the torque and flux comparisons are fed into hysteresis controllers, whose outputs, combined by the sector detection, by means of $\alpha - \beta$ stator flux estimations, determine the switching state desired. These switching states are stored in a vector selection table, which are pre-defined voltage vectors, corresponding to different possible inverter states, [22].

Figure 2.17 illustrates a block diagram of a typical DTC method. As a result of the operation described, the control method does not have a fixed operating frequency, and overmodulation mode is complex; this leads to it not being suitable for high power drives, namely in railway applications, [8].

Some improvements have been investigated to the simple DTC, such as the employment of Space-Vector Modulation (SVM), usually regarded as DTC-SVM, in replacement of the simple look-up table. With this strategy, the DTC can work with a fixed switching frequency; during a sampling period, the desired voltage vector is calculated, and then synthesised at the SVM block. Additionally, the hysteresis controllers are eliminated in favour of PI controllers, that sets the torque angle to control the motor torque. This implementation retains the high dynamics of regulation as the regular DTC, whilst operating at a fixed frequency, but keeps its overmodulation issues, [8].

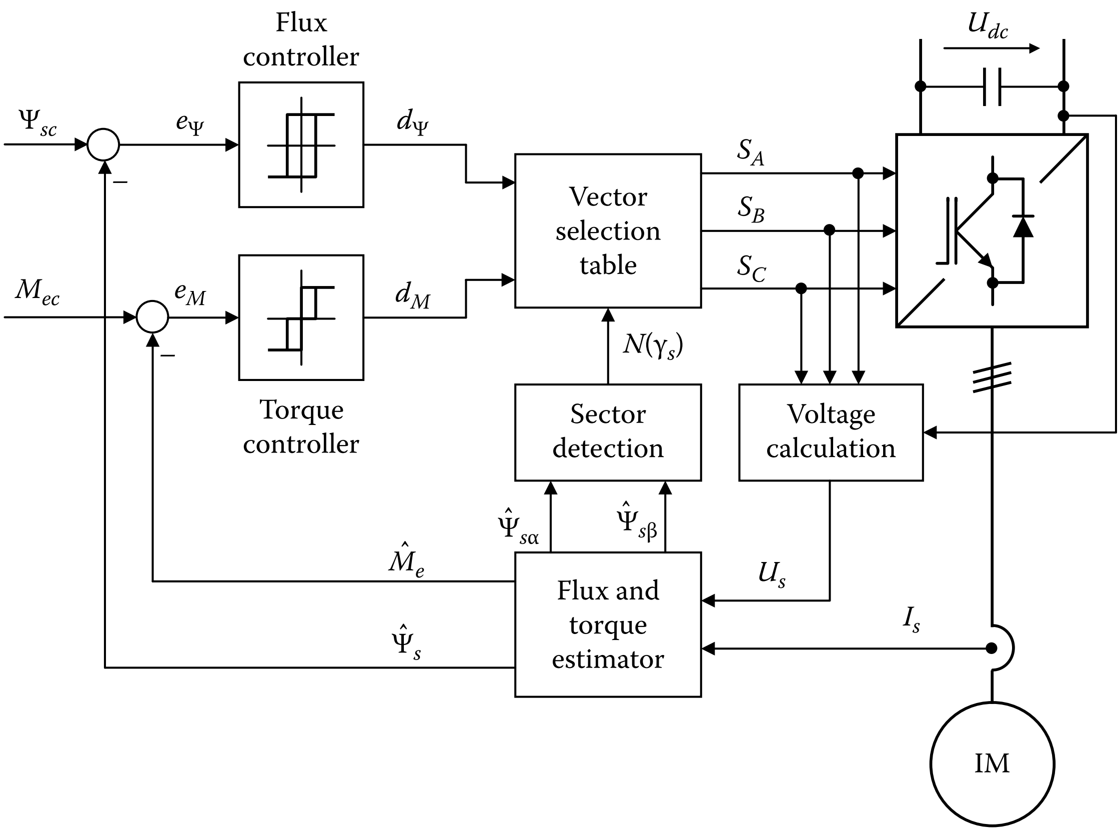


Figure 2.17: Generic DTC control schematics. Extracted from [22].

### 2.4.4 Model Predictive Control

Considered to be a good alternative to DTC, Model Predictive Torque Control, as is usually named when applied to motor drives, employs a cost function with regards to torque and flux errors, and selects the appropriate voltage vector that minimises it, as opposed to a deterministic approach made by the DTC.

The reference torque (in the case of figure 2.18, it is obtained by a speed controller) and flux are obtained and compared against the estimated and predicted torque and flux of the electric motor. To obtain these, it is necessary to employ a state observer, that uses a gain matrix for further tuning of the model. The cost function also uses a weighting factor for the flux difference, which can be very difficult to obtain and tune, [25].

MPTC suffers from model tuning high sensitivity and weak operation during faults. However, while comparing it to DTC, it was concluded that it followed the torque and flux references with higher precision; with regards to FOC, it was also concluded that, while it kept a similar steady-state performance, the settling time was faster, [25].

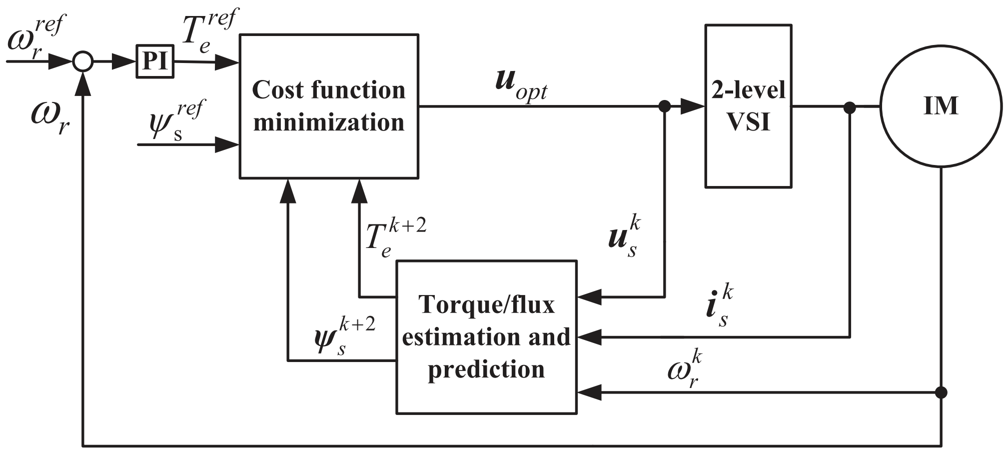


Figure 2.18: Schematic for a generic MPTC implementation. Extracted from [25].

## 2.5 Sensorless control and speed estimation techniques

A trend in the current electric drives field investigation is the use of sensorless control. This is justified by the fact that, usually, for the employment of speed or torque control techniques in electric motors, a measurement of speed and/or position is necessary, specially in the case of FOC. The mentioned measurement can be done by different devices, such as a resolver or a rotary encoder, [21], and by further signal processing. However, these sensors are very prone to electromagnetic interference by other power lines, and in a railway scenario, with many systems working simultaneously (communication, signaling, power delivery through the catenary), the performance derived from these can be impacted. Moreover, the addition of the measuring equipment increases the overall system complexity and cost, whilst not forgetting the higher maintenance needs, [21].

Sensorless control techniques are usually divided in two main classes: the first is characterised by signal injection and later signal processing; the other one uses the electric motor steady state equivalent circuit equations, and a combination of prediction techniques. A generic characterisation tree diagram can be seen in figure 2.19.

In this work, a review of three Machine Model-Based Methods will be done in the current section.

### 2.5.1 Direct Calculation Method (DCM)

The technique used is based on the flux estimation through the voltage equations. The speed is obtained by a direct manipulation of the equations of the stator voltages. While it can be characterised by being a relatively simple to implement technique, and of fast calculation, [26], [27], it also suffers from deviation errors, expressly in low speed operation due to the reliance on the stator resistance, and its inherent variation due to temperature; the use of an ideal integral can also be a difficulty in implementation works, whilst the measurement of the stator voltage can impose challenges due to the PWM switching characteristics delivering a waveform unsuitable for proper processing, [26].

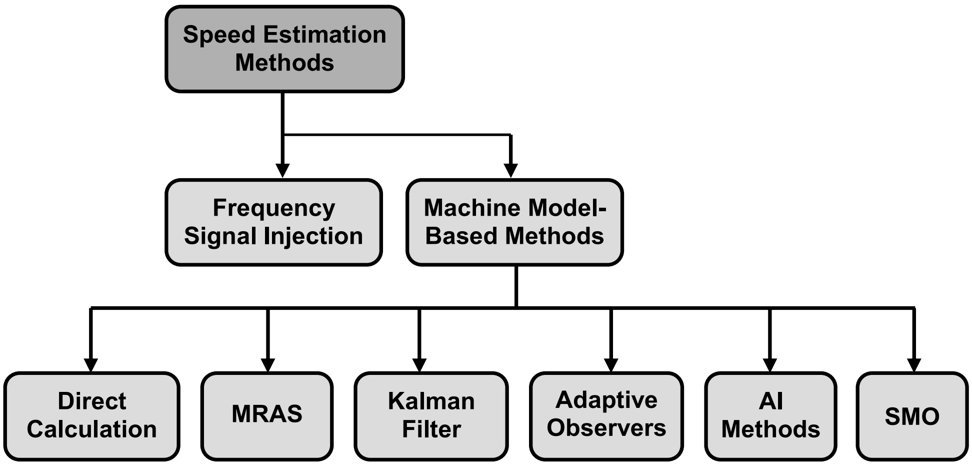


Figure 2.19: Figure showing the main speed estimation techniques. Adapted from [26].

### 2.5.2 Model Reference Adaptive System (MRAS)

MRAS-based approaches to speed estimation include three main parts: a reference model, an adjustable model and an adaptation mechanism. They are interconnected in the way shown in figure 2.20.

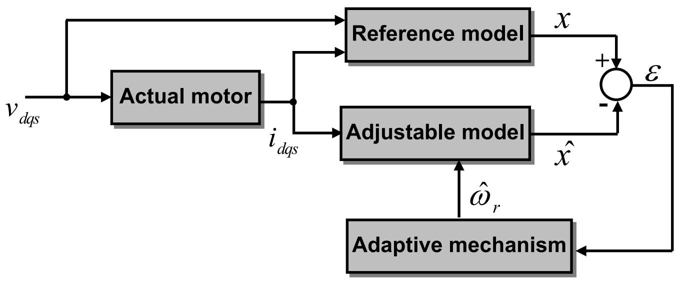


Figure 2.20: Implementation schematic of a MRAS-based implementation. Extracted from [26].

The reference model uses the stator voltages and currents to calculate the state variable, $x$, in a similar way to how it is done in the Direct Calculation Method. Furthermore, the adjustable model relies on the estimated speed to calculate its own output. The outputs of the two models are compared, and the difference is sent into the adaptation mechanism, which fulfils the function of outputting the estimated speed, to then be used in the adjustable model, thus closing the loop on the feedback system. The adaptation mechanism should be designed in a way that ensures system stability as well as a high adaptation rate, [28]. Based on the state variable being calculated and estimated, the MRAS type changes. The most common ones are rotor flux, back electromotive force (EMF) and stator current based MRAS, with different implementations, as well as advantages and disadvantages for each one, [26].

Whilst keeping the small computational load of the DCM, the MRAS adds robustness and accuracy in low-speed regions depending on the type chosen. However, it is still sensitive to model inaccuracies and noise, and the adaptation mechanism design can be difficult to tune, [26].

### 2.5.3 Extended Kalman Filter (EKF)

The strength of the EKF approach lies in its noise and modelling error or inaccuracy rejection. The implementation is usually done by having a prediction model which is an observer of the actual physical process, and comparing the estimation to the actual output. The error of the observer and its estimated state variable are fed into a Kalman Filter Correction, delivering the estimated speed. A typical implementation diagram is present in figure 2.21.

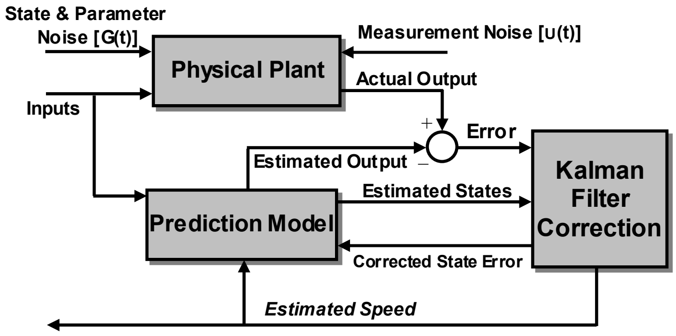


Figure 2.21: Implementation schematic of a EKF-based implementation. Extracted from [26].

While it can be said that the EKF is the most robust methodology in Machine Model-Based Methods, it also carries a high computational load, and with it, a high processing time, demanding great performance from the CPU in order to fulfil real-time operation constraints, [26].

## 2.6 Modulation Techniques

Due to the switching frequencies limitations present in railway traction drives (usually under 1000 Hz in IGBT drives, even lower in GTO drives) to reduce switching losses, some issues appear: high current ripples, which translate into high torque ripples. These ripples can cause high stress on the mechanical system, reduced passenger comfort and even difficulty in standard compliance (as a result of the harmonic production), [8]. As such, high torque ripples must be traded off with high switching losses. A solution commonly used to reduce these problems is to dynamically change the modulation techniques, switching frequency and even control strategies over different speed ranges. In figure 2.22, the pulse mode of the 700 series *Sinkansen* High-Speed train, [29], is presented, where it can be observed how the traction control unit trades different modulation techniques depending on the train's speed.

### 2.6.1 Asynchronous PWM

In the case of the Asynchronous PWM, the modulation index, defined as the ratio between the frequencies of the carrier and modulation waves, is not an integer. The most used PWM technique is the Sinusoidal, where the carrier wave is a sine wave, and the modulation wave a triangular one. The PWM signal is obtained by the comparison of the two waves. Other techniques, such

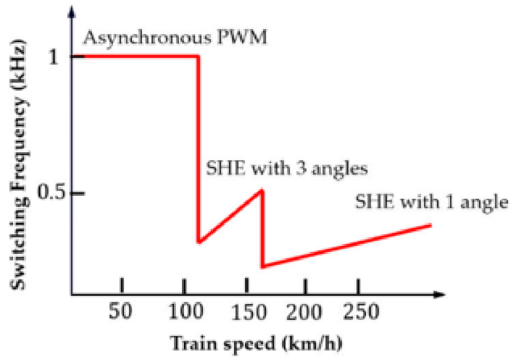


Figure 2.22: Different modulation techniques over a speed range in the Sinkansen train. Extracted from [8].

as the Third Harmonic injection, change the carrier wave to a sine wave with a third harmonic component, leading to higher output amplitude and a better DC bus utilisation, [30].

Space-Vector Modulation is another widely used technique. The inverter is seen as a state space machine, with eight different combinations of switches turned on or off. Six of these correspond to active, since each of them produces a different voltage, and two of them as zero, since both of them produce zero voltage output. Each state is modelled by the output voltage it produces, regarding what semiconductors are conducting or blocking the current. When the voltage output is zero, the current flows in the freewheeling diodes.

If all state vectors are drawn in a $\alpha-\beta$ reference frame, figure 2.23 is obtained:

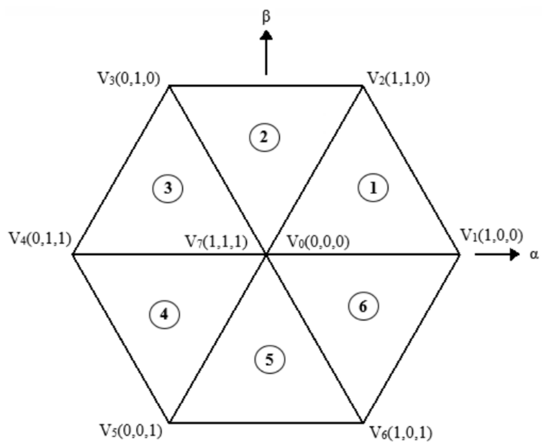


Figure 2.23: Different space vectors plotted in the $\alpha-\beta$ plane. Extracted from [31].

Since the $\alpha-\beta$ plane is used, the Clarke transformation is therefore used for this method. It can be observed that the zero and seven vectors are the zero vectors mentioned, and the other ones the active vectors. Between each active vector there is a 60 º angle, corresponding to a sector; in total, six sectors compose the plane. When a voltage command is obtained at the modulation level, it can be mapped inside one of the sectors. The SVPWM method ensures the calculation, over a modulation period, of the duty cycles of the two active vectors and the zero vector closest to where the command vector is located in the plane, which corresponds to looking at the sector defined by these three. After having determined these values, the last step in the algorithm is to choose an appropriate sequence of applied voltages. Since the objective is to obtain, over a modulation period, an average voltage equal to the command voltage, then the order of appearance of each voltage vector is transparent to this requirement. There are various methods in this chapter, that can improve EMI or efficiency, by reducing the number of commutations. Comparing this method to conventional PWM, the SVPWM increases the DC bus utilisation, lowers the THD and can be more efficient, [22], [31].

### 2.6.2 Synchronous PWM-Selective Harmonic Elimination (SHE)

This operation regime controls the number of commutations performed per quarter of the fundamental cycle, in order to reduce the switching losses of the semiconductors. The angles at which they occur are pre-calculated using a Fourier analysis, optimised for reducing lower order harmonics at the output. In the example illustrated in figure 2.22, three angles are calculated in medium-high speed ranges, while at higher speed ranges the modulation changes to one angle calculation; this results in lower switching losses since fewer commutations per cycle are executed, [8].

# Chapter 3

# Theoretical Background

As mentioned in the introduction, the work developed focuses on the refurbishment of the *Siemens* series 2300/2400 TCU. The units 2414 and 2413 are shown in figure 3.1.


Figure 3.1: Photograph of two EMU 2400 units. Taken from [32].

After some research done in conjunction with *Nomad Tech*, the characteristics obtained are presented in section 3.1.

## 3.1 Present Power Structure

The current power structure is very similar to the one presented in 2.8, where the main transformer feeds a four-quadrant converter, which through a DC link capacitor transfers the power to a VSI, driving two motors in parallel, as can be seen in figure 3.2. Additionally, there are a few protection measures, such as a thyristor shorting the VSI terminals when the DC voltage is too high, avoiding further damages.

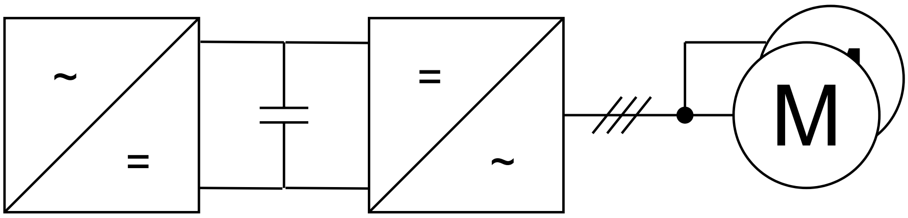


Figure 3.2: Power structure driving the IMs in the 2300/2400 EMU.

It should be noted, however, that even though the train still uses GTO for the semiconductors, the dissertation will not focus on them since the fleet will be modernised (and is currently being) to IGBT switches. The dissertation will focus on the control of the inverter, where the control laws for the motor will be applied and tested. The motors used in this train unit are IMs, and the acquired motor characteristics are shown in section 3.1.1.

### 3.1.1 Motor characteristics

The following motor characteristics were provided by CP:

Table 3.1: Traction Motor (Induction) Characteristics

| Parameters | Value |
|---|---|
| Nominal voltage (V) | 1638 |
| Nominal current (A) | 190 |
| Nominal frequency (Hz) | 97 |
| Nominal speed (rpm) | 1920 |
| Power factor | 0.77 |
| Nominal power (kW) | 393 |
| Maximum speed (rpm) | 4000 |

Unfortunately, the equivalent circuit parameters were not provided. As such, in the future, static tests could be performed on the motor to obtain these.

The IM has a squirrel-cage construction, which means the rotor is made up of several metallic bars (usually copper or aluminium) in a diagonal disposition. These bars are then electrically connected in their terminals using short circuit rings. A diagram illustrating these aspects can be seen in figure 3.3.

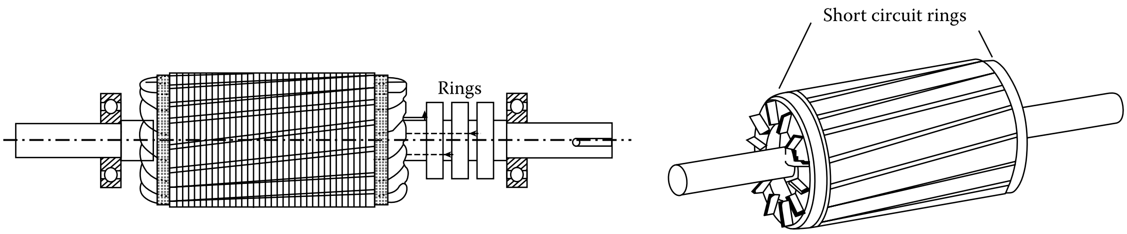


Figure 3.3: Lateral and diagonal views of the squirrel-cage rotor. Taken from [22].

### 3.1.2 Sensorization

Currently, the sensorization offer is ample, since there is a number more than sufficient of measurements taken. The TCU has access to the DC link voltage, that can vary by some pre-established boundaries. Additionally, there are current measurements in the three phases of the inverter outputs, that correspond to the motors' stator windings inputs. These measurements are essential to the control logic applied. There are also temperature readings from the inverter and motors, that can be used to determine possible current/power limitations due to safety concerns (i.e., it may be established that the IGBT switches cannot exceed a certain temperature, and a limit on output power must be made in case the current temperature reaches the imposed limit).

### 3.1.3 Control Method

According to the research made, the control unit currently divides itself in three operating regimes, according to speed. In the first one, from standstill to low speeds, the motor is actuated by use of V/f control, that varies the voltage and frequency in a fixed ratio to vary the speed. The following stage is comprised of vector control. After the train reaches a high speed, "block" control is implemented, essentially to reduce the number of commutations performed in the GTO based inverter, and lower its heat emission. This strategy is used since the current flowing through them is very high at this stage due to the motors' high power demand, leading to high conduction losses. By decreasing switching losses, it is possible to control the temperature of the devices.

The switching frequency is set at 300Hz. One of the purpose of the dissertation is to introduce a higher frequency, that enables tighter control. Unfortunately, current GTO offer cannot support these values. Fortunately, it is known beforehand that the these semiconductors will be replaced by modern IGBT devices, thus overcoming this problem up to a certain level

## 3.2 Induction Motor Modelling

In order to understand the behaviour of the IM, a T model of the machine is presented in figure 3.4.

This circuit models the electrical behaviour of the IM in a steady-state scenario. Due to the inherent squirrel-cage construction, the rotor current and voltage readings are inaccessible. As such, these can be indirectly determined with the help of the circuit presented. It should be noted that the rotoric parameters are modelled after their effect on the stator.

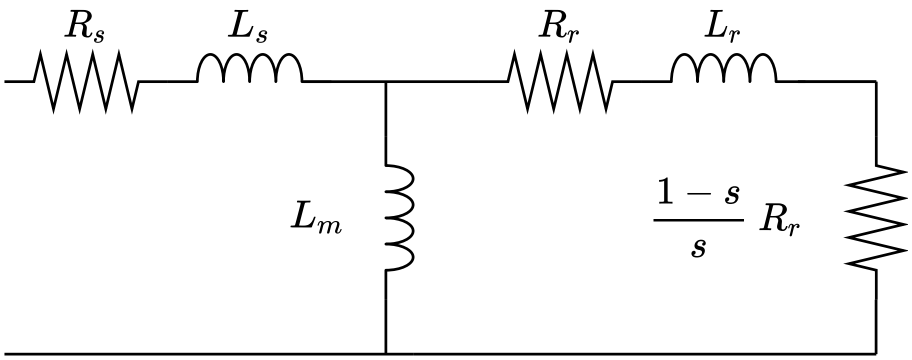


Figure 3.4: Steady-state equivalent circuit of an Induction Machine, where $s$ indicates the slip.

The slip can be defined as:

$$s = \frac{n_{sync} - n_{rotor}}{n_{sync}} \tag{3.1}$$

Where $n_{rotor}$ is the rotor speed. The synchronous speed, $n_{sync}$, is determined by the stator frequency ($f_s$), and pole pairs ($p$) by 3.2.

$$n_{sync} = \frac{60 f_s}{p} \tag{3.2}$$

Furthermore, the electrical frequency of the rotor ($f_r$) and stator ($f_s$) are related by means of the slip, $s$:

$$f_r = s\ f_s \tag{3.3}$$

Regarding the power considerations, the supply power, $P_s$ can be written as a function of the stator voltage, current and the phase difference between these; $V_s$, $I_s$ and $\phi_s$, respectively:

$$P_s = 3\ V_s\ I_s\ cos\phi_s \tag{3.4}$$

However, the power transferred ($P_t$) to the rotor can only be a part of this value due to the Joule losses ($P_{js}$) in the stator windings and in the iron core, $P_{fe}$.

$$P_t = P_s - P_{js} - P_{fe} \tag{3.5}$$

Where the stator Joule losses are dependent on the stator resistance, $R_s$, and current, $I_s$, and the iron core losses dependent on the stator EMF ($E_s$) and the iron resistance, $R_{ir}$.

$$P_{js} = 3 R_s I_s^2, P_{fe} = 3\frac{E_s^2}{R_{ir}} \tag{3.6}$$

It can be stated that the values attributed to these parameters deeply influence the simulation of the motor, as well as possible control methods applied to it and their performance. As such, there are empirical methods dedicated to determine these.

### 3.2.1 Parameter Determination

Dedicated to sole purpose of parameter determination in three-phase rotor squirrel cage IM, the method described is divided into three main steps:

- Measurement of the DC resistance of the stator windings: the measurements should be done in each phase-to-phase terminals (UV, VW, WU). The stator resistance, $R_s$, is obtained by summing the three values obtained, and diving them by six.

- No-load test: Applying the rated stator voltage, and letting the rotor spin, the nominal speed is quickly obtained. In this scenario, the slip is very small. Thus, the circuit presented in 3.4 can be simplified to 3.5:

$$s \approx 0 \Rightarrow \frac{1-s}{s} R_r \approx \infty \tag{3.7}$$

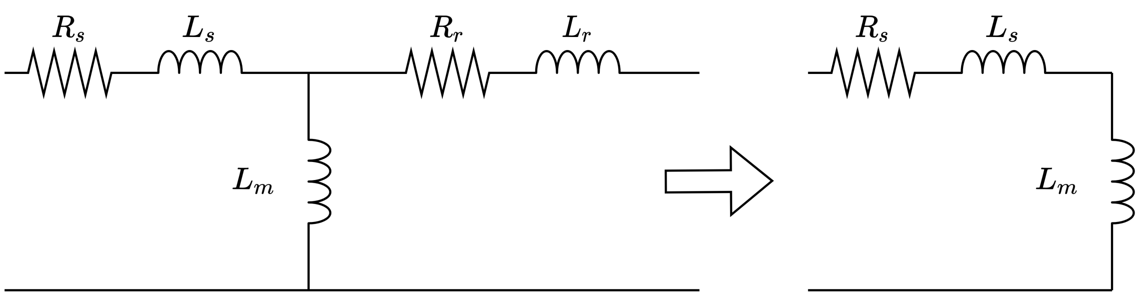


Figure 3.5: IM equivalent circuit under no-load test.

With the measurement of the voltages and currents at the stator windings, at different current points, and with further processing, the parameters for the stator can be obtained, as well as the magnetizing inductance. The no-load impedance can be determined with equations 3.8 and 3.9. The resistive and inductive components can be found with 3.10, with the use of the angle between voltage and current, $\phi$.

$$Z_{nl} = R_s + j\omega(L_s + L_m) \tag{3.8}$$

$$Z_{nl} = V_{nl}/I_{nl} \tag{3.9}$$

$$R_{nl} = R_s = Z_{nl} cos\phi \ , \ X_{nl} = Z_{nl} sin\phi \tag{3.10}$$

- Blocked rotor test: this test is done by assuring the rotor speed is zero, by blocking it, and feeding it with a fixed frequency and variable voltage. This equates to the slip being one. It can be electrically compared to the short circuit test on a transformer. The start-up torque can also be obtained. The equivalent IM circuit is simplified to 3.6:

$$s = 1 \Rightarrow \frac{1-s}{s} R_r = 0 \tag{3.11}$$

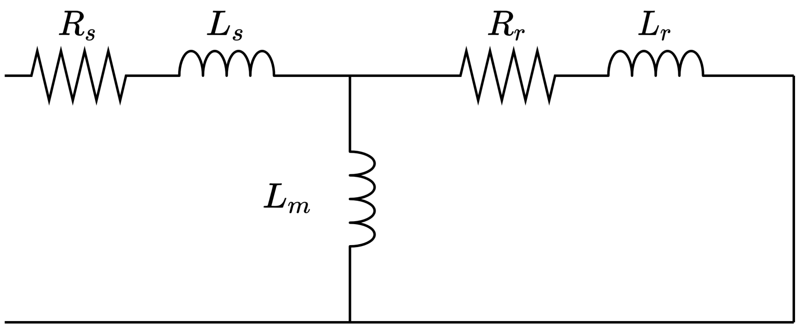


Figure 3.6: IM equivalent circuit under blocked rotor test.

The equivalent impedance seen from the stator, $Z_{br}$, is the stator impedance in series with the rotor impedance summed in parallel with the magnetizing inductance, as written in equation 3.12.

$$\begin{aligned} Z_{br} &= R_s + jX_s + [jX_m || (R_r + jX_r)] \\ &= R_s + R_r \frac{X_m^2}{R_r^2 + (X_m + X_r)^2} + j\left(X_s + \frac{X_m(R_r^2 + X_r(X_m + X_r))}{R_r^2 + (X_m + X_r)^2}\right) \end{aligned} \tag{3.12}$$

By assuming $X_m >> R_r$ (which holds true for the majority of IM), equation 3.12 can be simplified to:

$$Z_{br} \approx R_s + R_r \left(\frac{X_m}{X_m + X_r}\right)^2 + j\left(X_s + X_r \frac{X_m}{X_r + X_m}\right) \tag{3.13}$$

The resistance and reactance at rated frequency under the blocked-rotor tests can then be assigned as the real ($R_{br}$) and imaginary ($X_{br}$) part, respectively, of the equation 3.13. The rotor resistance and reactance are found in 3.14.

$$\begin{aligned} X_r &= (X_{br} - X_s)\left(\frac{X_m}{X_m + X_s - X_{br}}\right) \\ R_r &= (R_{br} - R_s)\left(\frac{X_r + X_m}{X_m}\right)^2 \end{aligned} \tag{3.14}$$

From equation 3.8, it can be seen that the no-load reactance is equal to the sum of the stator reactance and the magnetizing reactance. Replacing it in equation 3.14 yields:

$$X_r = (X_{br} - X_s)\left(\frac{X_{nl} - X_s}{X_{nl} - X_{br}}\right) \tag{3.15}$$

The rotor reactance can be found using the data extracted from the two tests, and with the stator reactance. However, this parameter is still unknown. The IEEE Standard 112 dictates that the relationship between the stator and rotor reactances vary according to the motor class [33]. Commonly, assuming the motor class is not known, these values are set to equal. From this assumption, equation 3.15 can be solved to obtain the rotor reactance, followed by the magnetizing inductance. After these calculations, the rotor resistance can then be computed through 3.14.

Through the employment of the described method, the parameters of the tested IM are obtained in an empirical and tested approach. The tests can increase their accuracy if temperature readings are done throughout the experiments, and resistance values are adjusted according to equation 3.16:

$$R_{t=T} = R_{ref}[1 + \alpha(T - T_{ref})] \tag{3.16}$$

Where $\alpha$ indicates the temperature coefficient of resistance, that varies according to the material of the conductor used.

A typical test setup for conducting the referred assays can be found in 3.7:

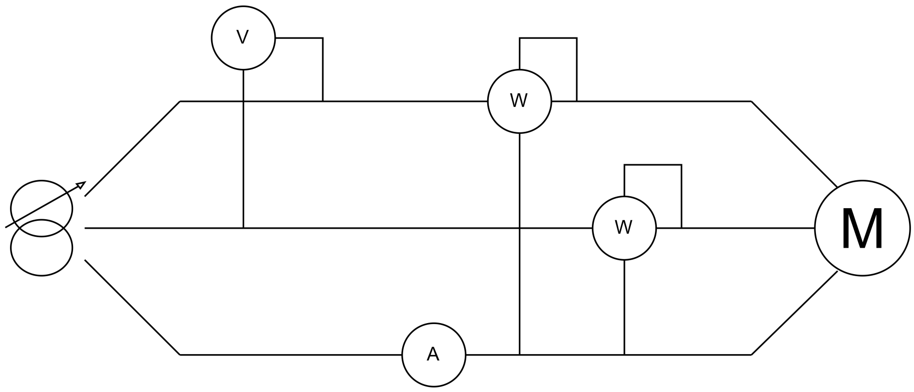


Figure 3.7: Variac, three-phase IM and measuring instruments diagram.

The voltmeter measures the phase-to-phase voltage, while the ammeter obtains the line current. The wattmeters ensure the measurement of the power.

### 3.2.2 Torque-Speed Characteristic Determination

In order to fully understand the expected behaviour of the motor being studied, it is common to draw the torque-speed curve, where several conclusions can be extracted, such as the peak torque and the slip that it occurs at. It is usual to determine the Thevenin equivalent of the stator impedance and magnetizing reactance. These values can be obtained with equations 3.17,3.18:

$$V_{eq} = \frac{V_s}{(R_s + jX_s) + jX_m} jX_m \tag{3.17}$$

$$Z_{eq} = \frac{(R_s + jX_s)\,jX_m}{(R_s + jX_s) + jX_m} \tag{3.18}$$

After the simplifications, the equivalent circuit can be drawn as figure 3.8.

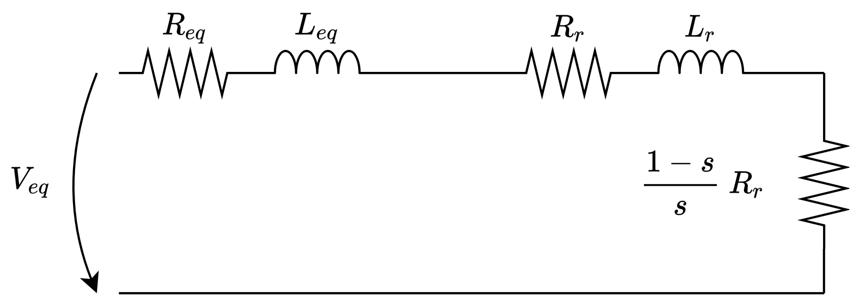


Figure 3.8: Thevenin equivalent circuit of the IM.

The electromagnetic torque can be calculated using 3.19:

$$T_e = 3V_{eq}^2 \frac{p}{\omega_s} \frac{R_r/s}{(R_{eq} + (R_r/s))^2 + (X_{eq} + X_r)^2} \tag{3.19}$$

By computing the torque at different slip points, the desired torque-speed curve is obtained. As an example, figure 3.9 draws a typical curve for an IM.

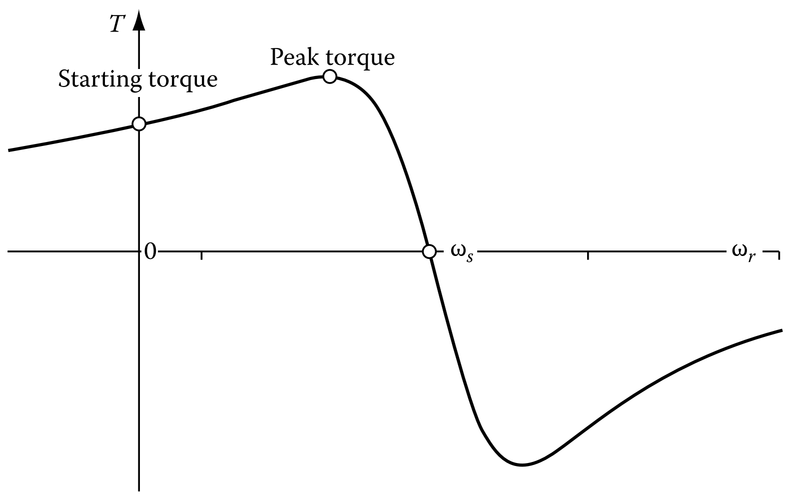


Figure 3.9: Typical torque-speed curve of an IM. Extracted from [22].

## 3.3 Field-Oriented Control

To improve the current performance of the trains, a refurbishment of the control laws is essential. As such, it is proposed to use vector control, more specifically Field-Oriented Control. Additionally, it is necessary to define which variation of FOC should be used. It was decided to choose the IFOC implementation, due to its simplicity and high performance in all speed ranges.

Some considerations must also be made regarding the switching frequency. Whilst increasing the current value (around 300 Hz) will most definitely improve the dynamic performance of the train and lower the torque ripples, consequently increasing passenger comfort and decreasing the wear and tear of the traction chain, it is extremely relevant to take into account the increased semiconductor losses, even though the new topology used supports the use of higher switching frequencies. It is then proposed to conduct a thermal study of the test bench, as an initial validation of the traction control method refurbishment. Additionally, conflicts between the electromagnetic interference (EMI) generated by the PWM switching can deteriorate or even disrupt the normal functioning of other systems essential to train circulation, such as the signaling or Convel system, which monitors and controls the trains speeds. It was then proposed by *Nomad Tech* to study a switching frequency multiple of the actual value (1200 Hz).

For an effective Field-Oriented Control theoretical background, the IM's equivalent circuit under the *d*-*q* frame must be introduced. In figure 3.10, a graphical representation of the mentioned concept is presented. It should be reminded that, in order to obtain this reference frame, the Park-Clarke transformation is needed.

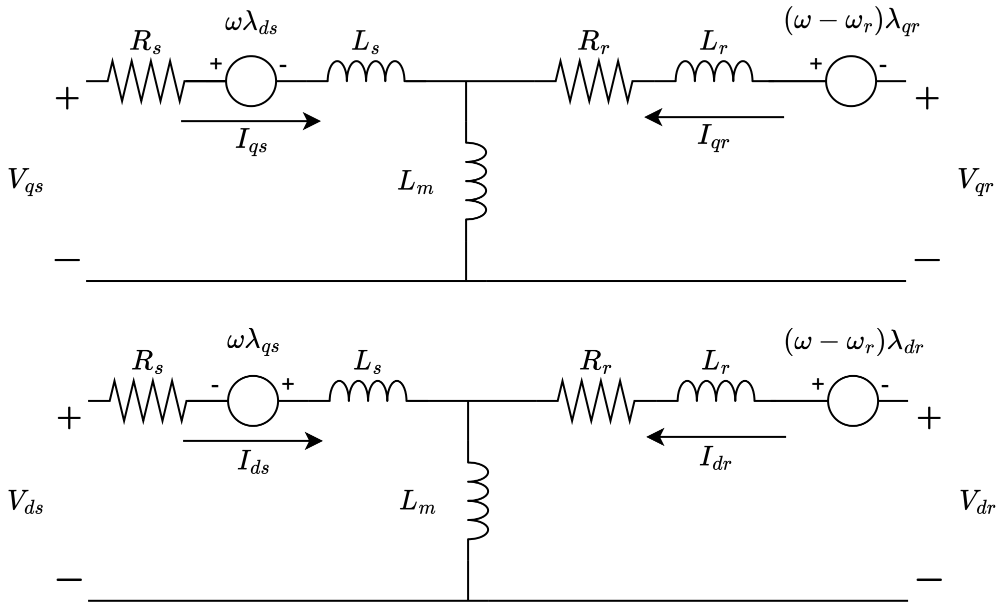


Figure 3.10: IM equivalent circuit in *q* (top) and *d* (bottom) frame.

$\omega$ refers to the reference frame angular velocity, while $\lambda$ indicates the corresponding flux component, depending on its index (for example, $\lambda_{qs}$ refers to the stator flux's *q* frame component), the same way the currents and voltages are described.

Furthermore, the steady-state equivalent voltage and flux equations are presented in 3.20.

$$\begin{cases} V_{qs} = R_s i_{qs} + \frac{d\lambda_{qs}}{dt} + \omega\lambda_{ds} \\ V_{ds} = R_s i_{ds} + \frac{d\lambda_{ds}}{dt} - \omega\lambda_{qs} \\ V_{qr} = R_r i_{qr} + \frac{d\lambda_{qr}}{dt} + (\omega - \omega_r)\lambda_{dr} \\ V_{dr} = R_r i_{dr} + \frac{d\lambda_{dr}}{dt} - (\omega - \omega_r)\lambda_{qr} \\ \lambda_{ds} = L_s i_{ds} + L_m i_{dr} \\ \lambda_{qs} = L_s i_{qs} + L_m i_{qr} \\ \lambda_{dr} = L_r i_{dr} + L_m i_{ds} \\ \lambda_{qr} = L_r i_{qr} + L_m i_{qs} \end{cases} \tag{3.20}$$

One important characteristic in the voltage equations is the cross-coupling effect of the flux linkages, where the opposite axis' flux times the speed influences the voltage of the said axis. Additionally, since in a squirrel-cage IM the rotor bars are all connected through the short circuit rings in their ends, their voltages equal to zero.

The electromagnetic torque produced by the machine can be expressed by 3.21.

$$T_e = \frac{3}{2}\frac{P}{2}\frac{L_m}{L_r}(\lambda_{dr} i_{qs} - \lambda_{qr} i_{ds}) \tag{3.21}$$

As previously stated in 2.4.2, the main goal of FOC is to apply a similar torque behaviour of a DC motor to an IM, through the decoupling control of flux and torque. As can be noted in the torque equation of a DC motor, 2.4, it is directly proportional to the armature current applied since, in steady-state, the flux is constant. Additionally, due to the construction of the motor, the magnetomotive force is constantly 90 electrical degrees apart from the flux, thus always maximising the torque output, [21]. By the instantaneous control of the armature current, the torque is consequently instantaneously controlled.

However, in the case of the IM, these requirements are not always met. Due to the nature of its three-phase current supply, the torque and flux producing currents are not always 90 electrical degrees apart, nor can they be controlled independently. Through the application of the *Park-Clarke* transformation, the *abc* currents are transformed into a *d*-*q* frame, inherently 90 degrees apart from each other. Commonly, the *d* axis is designated to be the flux producing one, while the *q* axis is assigned to the torque producing one, as can be seen in 3.11. To ensure a correct application, the *d* axis must be coincident with the flux vector. This way, the currents are simultaneously kept 90 degrees apart and can be independently controlled, due to no cross-coupling effects. $i_{qs}$ controls the torque, whilst $i_{ds}$ controls the magnitude of the flux vector. To assure the instantaneous control of the torque producing current, it is common to apply a PI controller to it.

Due to the alignment of the *d*-axis, the *q* flux component becomes null, while the *d* component absorbs the totality of the flux vector. This has deep influences in the torque control. Revisiting equation 3.19, a definitive parallel between this equation and the DC motor torque equation can be drawn.

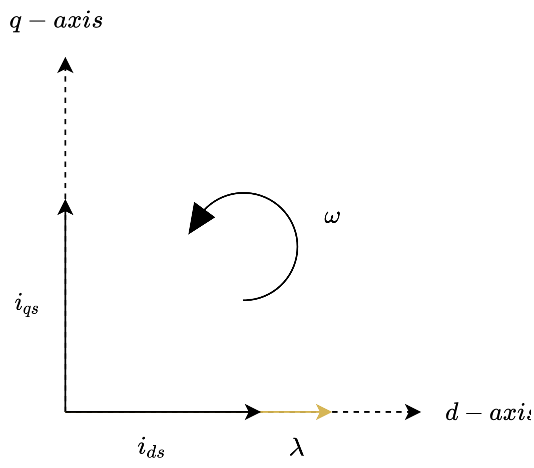


Figure 3.11: Reference *d*-*q* frame rotating at $\omega$ speed, with the current and flux vectors.

$$T_e = \frac{3}{2}\frac{P}{2}\frac{L_m}{L_r}(\lambda_{dr}i_{qs} - \lambda_{qr}i_{ds}) = \frac{3}{2}\frac{P}{2}\frac{L_m}{L_r}|\lambda|i_{qs} \tag{3.22}$$

As mentioned in 2.4.2, the obtainment of the theta angle can be done through different ways. The choice of the method used will thoroughly impact the performance of the control method, since it is of the utmost importance to keep the *d*-axis aligned with the flux vector. The slightest deviation in this step will result in significant control degradation. With these steps in mind, it is possible to setup current regulators for the desired performance of the motor. A typical implementation block diagram of this application can be found in 2.14.

### 3.3.1 Flux and Torque estimation

To employ an accurate and responsive control for the IM, an estimator for flux is a regular option in many control systems. The methods used for the estimation use the measured current, voltages and speed in order to compute the estimated value.

There are two main approaches to the flux estimation in an IM:

- *Voltage model*

  This model uses the stator voltage equations to derive the stator flux linkages, which in turn are used to obtain the rotor flux linkages. Essentially, the method uses the integration of the back-emf of the motor:

$$\lambda_{s\alpha\beta} = \int (V_{s\alpha\beta} - I_{s\alpha\beta}R_s)dt \tag{3.23}$$

  The flux angle is calculated as:

$$\theta = tan^{-1}\frac{\lambda_{s\alpha}}{\lambda_{s\beta}} \tag{3.24}$$

And finally, the torque can be estimated with 3.25:

$$T_e^{est} = \frac{3}{2}\frac{P}{2}(\lambda_{s\alpha}I_{s\beta} - \lambda_{s\beta}I_{s\alpha}) \tag{3.25}$$

Alternatively, in the *d*-*q* frame, the equation in 3.26 can also be used.

$$T_e^{est} = \frac{3}{2}\frac{P}{2}\frac{L_m}{L_r}\lambda_{dr}i_{qs} \tag{3.26}$$

This method suffers from a problem due to the pure integrator. When there is an offset error in the measurement of the back-EMF, the integrator saturates and produces an unacceptable DC offset in its output. Additionally, when implemented digitally, the integrator adds a drift. This is usually fixed by using a High-pass filter at the output of the integrator, or by replacing it with a Low-pass filter. It can be observed in 3.27 the equality between these two alternatives. However, this approach adds a phase and gain error, so the design process of the cutoff frequency should be careful. Since back-emf increases with speed, and at low speeds it is low, this method suffers from some inaccuracy in the lower speed regions [21], [34].

$$H(s) = \frac{1}{s}\frac{s}{s+\omega_0} = \frac{1}{s+\omega_0} \tag{3.27}$$

- *Current model*

Looking at the voltage equations present on 3.20, it is possible to obtain the flux linkages through the substitution of the rotor currents by the rotor flux linkages as shown in 3.28 and 3.29:

$$\frac{d\lambda_{dr}}{dt} = -R_r i_{dr} + (\omega - \omega_r)\lambda_{qr} \tag{3.28}$$

$$i_{dr} = \frac{\lambda_{dr} - L_m i_{ds}}{L_r} \Longleftrightarrow \lambda_{dr} = L_r i_{dr} + L_m i_{ds} \tag{3.29}$$

The *q*-axis flux linkage can be obtained through a similar manner. However, there is still the effect of the cross-coupling between the *d*-*q* axes. Therefore, in order to null this effect, if the rotor reference frame is chosen, then these terms will be null. This results in the differential equation shown in 3.30. The last variables to be computed are the stator currents in the rotor reference frame, that can be obtained though the transformation mentioned in 3.31:

$$\frac{d\lambda_{dr}}{dt} = -\frac{R_r}{L_r}\lambda_{dr} + \frac{R_r}{L_r}L_m i_{ds} \tag{3.30}$$

$$\begin{cases} i^r_{ds} = i^s_{ds}cos\theta_r + i^s_{qs}sin\theta_r \\ i^r_{qs} = -i^s_{ds}sin\theta_r + i^s_{qs}cos\theta_r \end{cases} \tag{3.31}$$

Where the rotor angle is obtained simply by the integration of the rotor speed. After the solving equation 3.30, the last step to be taken involves the inverse transformation of the rotor fluxes into the original stator reference frame, as shown in 3.32:

$$\begin{cases} \lambda^s_{dr} = \lambda^r_{dr}cos\theta_r - \lambda^r_{qr}sin\theta_r \\ \lambda^s_{qr} = \lambda^r_{dr}sin\theta_r + \lambda^r_{qr}cos\theta_r \end{cases} \tag{3.32}$$

Whilst the knowledge of the rotor resistance is essential to this method, and that this parameter can change substantially in different motor regimes due to higher temperatures, it behaves better in low-speed regions than the voltage model, [21]. It also requires the knowledge of the speed, thus further increasing the complexity of it.

## 3.4 Space-Vector Modulation

As previously stated in 2.6.1, the Space-Vector Modulation inserts the desired voltage vector inside its $\alpha - \beta$ reference frame, whilst determining the sector where it fits. From this point, the model calculates the times corresponding to the three vectors that define the sector where the voltage vector is inserted. Considering that the sum of the three times obtained must equal to a switching period, then the average voltage over a period can be written as equation 3.33:

$$V_s = \frac{1}{T_m}(t_1V_1 + t_2V_2 + t_0V_0) \tag{3.33}$$

Where $T_m$ is the switching period, equal to the sum of the three times. The times for each vector can be computed using the equations found on 3.34, which were obtained resorting to trigonometric relations, [22].

$$\begin{cases} t_1 = \frac{3T_m|V_s|}{2V_{dc}}cos(\theta - \theta_k) \\ t_2 = \frac{3T_m|V_s|}{V_{dc}}\frac{sin(\theta-\theta_k)}{\sqrt{3}} \\ t_0 = T_m - t_1 - t_2 \end{cases} \tag{3.34}$$

Where $\theta$ is the angle between the $\alpha$ axis and the reference voltage vector, and $\theta_k$ the angle between the $\alpha$ axis and the vector $k$.

The last step to take in the SVPWM model is to select the switching sequence that will determine the sequence of voltage outputs at the VSI. One common technique takes advantage of center-weighted PWM to achieve the desired voltage at the output. Each sector has a pre-defined pattern for each of the three SVPWM signals, that operate according to the times previously computed. As can be seen in figure 3.12, for the case of the sector 1, the sequence of the voltage vectors 0, 1, 2 and 7 (it should be noted that both the vector 0 and 7 produce a 0 V output, thus being identical in this view) is coded, only varying the duty cycles of each individual vector.

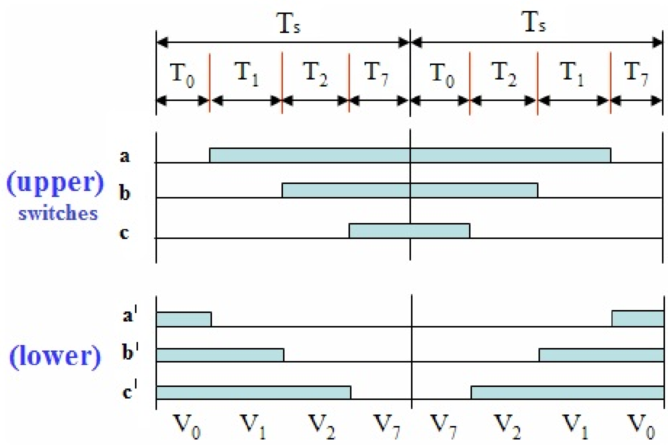


Figure 3.12: Switching sequence of sector 1. Taken from [35].

To deeply analyse the concepts regarded previously, a simple PSIM software was built with a three-phase VSI feeding a RL load, whilst being commanded with SVPWM. The DC link voltage was set to 100 V, and the switching frequency at 10 kHz.

Firstly, the output voltage waveform of one of the phases can be seen in figure 3.13. The maximum voltage observed corresponds to $\frac{2}{3}V_{dc}$, which in this case is equivalent to around 66.7 V.

In figure 3.14, the switching commands for the three upper semiconductors can be observed. It should be noted that the lower switches are commanded with the inverse signals, as can be stated from figure 3.12.

In terms of harmonic content, in figure 3.15 a Fast Fourier Transform of the output voltage is presented.

It can be extracted that the switching harmonics appear at integer multiple values of the switching frequency (in this case, 10 kHz). Furthermore, the center harmonic is not present, thus reducing its Total Harmonic Distortion as compared to other traditional methods, such as Sine-Triangle PWM. The bottom two graphs highlight the two first harmonics (excluding the fundamental component at 50 Hz), that exemplify this concept. Moreover, it can be stated that the second switching harmonic has a higher amplitude than the first one. This can lead to easier filter design due to lower need of a low cut-off frequency.

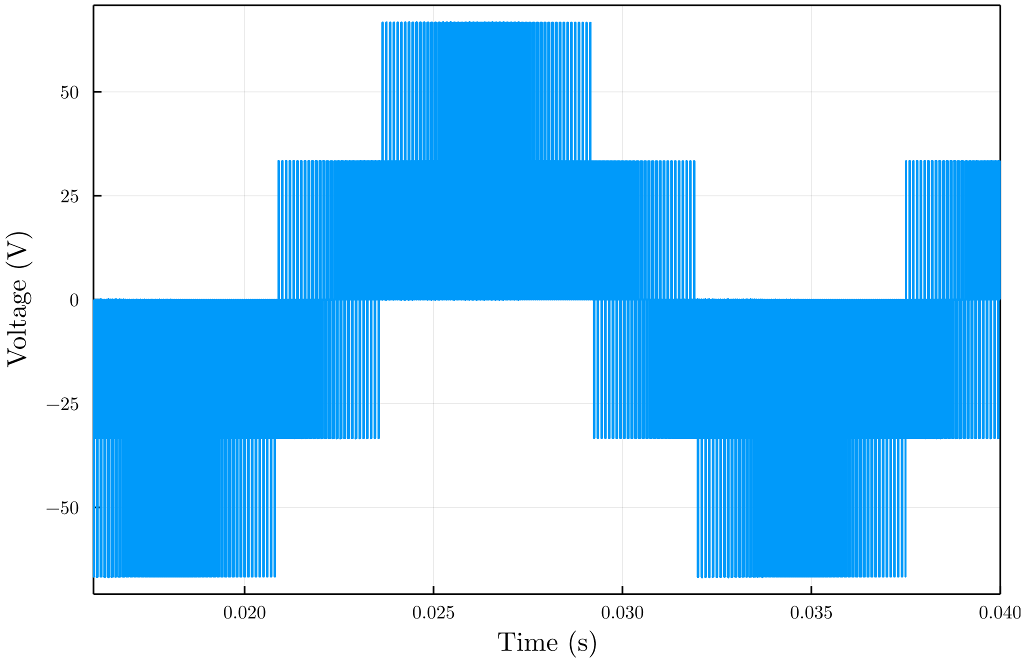


Figure 3.13: Voltage output of a three-phase VSI under SVPWM.

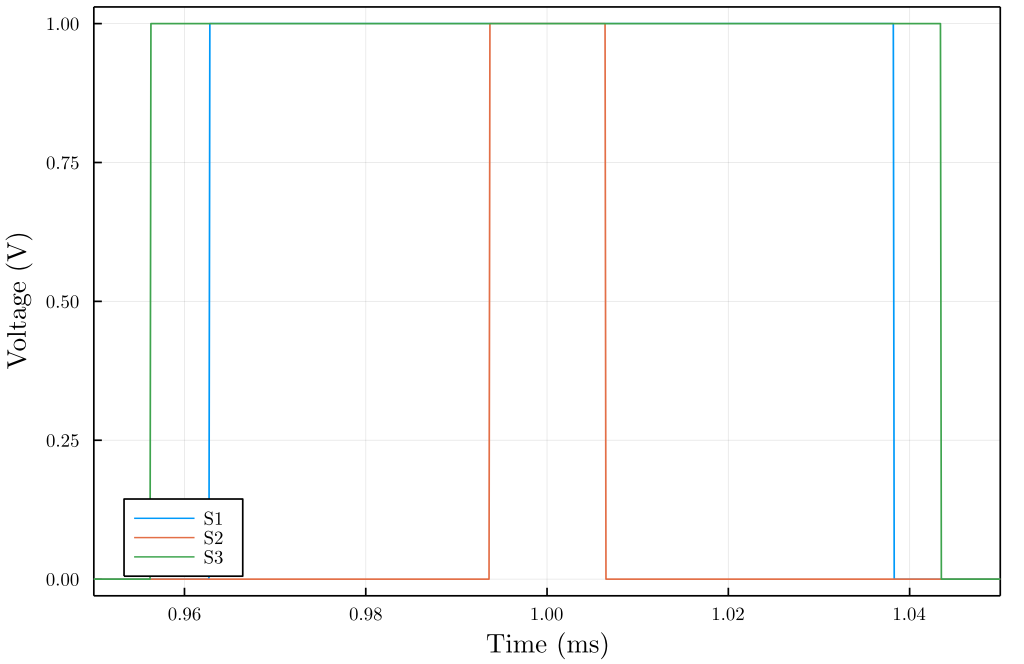


Figure 3.14: Switching waveforms for the three upper switches.

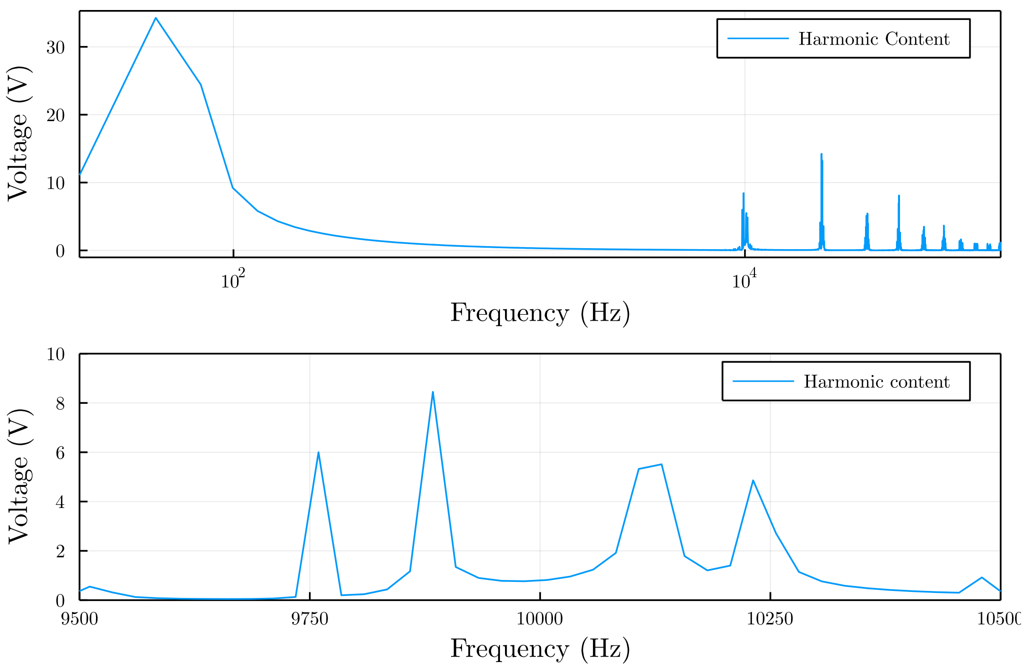


Figure 3.15: Harmonic content of the output voltages of the VSI under SVPWM.

## 3.5 Train Mechanical Considerations

To understand clearly the traction mechanical efforts a train faces, a few aspects will be discussed in this section, namely the load a generic train is subject to while on a normal ride.

In terms of traction, the speed attained by the train can be obtained with 3.35.

$$J\frac{d\omega}{dt} = T_e - T_l \tag{3.35}$$

Where $J$ is the moment of inertia, in $Kg.m^2$, $\omega$ the motor speed, $T_e$ the electromagnetic torque produced by the motors and $T_l$ the load torque (i.e., the resistive forces the train is subject to). It can be noted that, with higher $J$, the train has a higher difficulty in changing speed (i.e., accelerating or decelerating), but this variable is not controlled by the train driver. The only controllable aspect by the driver is the electromagnetic torque, which is used to control the vehicle speed.

Under driving, a train experiences multiple resistive forces. The total resistance can be decomposed as the sum of running resistance, $F_r$, curving resistance, $F_c$, and gravitational components, $F_g$, which is shown in equation 3.36.

$$F_{tr} = F_r + F_c + F_g \tag{3.36}$$

### 3.5.1 Running Resistance

Running resistance is composed of rolling resistance and air resistance. Due to the high difficulty in modelling these parameters, the work developed by William Davis resulted in the Davis equation, which approximates these components in a simple yet effective way. It has been used as an industry standard for a prolonged period, with several variation occurring for different railway operators [36]. The equation presented in 3.37 illustrates the concepts approached. In it, the running resistance, in $N$, is dependent on the regression coefficients $A$ $(N)$, $B$ $(N\ s/m)$ and $C$ $(N\ s^2/m^2)$. $A$ refers to the total train mass and the number of axles, whilst $B$ models the flanging friction. $C$ refers to the air resistance, thus its weight in the total resistance is dependent on the square of the speed, referred to in SI units, $m/s$. The equation in 3.37 is expressed as Newtons per tonne mass.

$$F_r = A + Bv + Cv^2 \tag{3.37}$$

### 3.5.2 Gravitational component

The component referring to the gravitational effect on the vehicle is obtained by using trigonometric relations regarding the vehicle on a non-levelled track, as shown in figure 3.16.

The component is described in 3.38 can be either positive or negative whether the vehicle is climbing or descending, respectively.

$$F_g = mg\ sin\theta \tag{3.38}$$

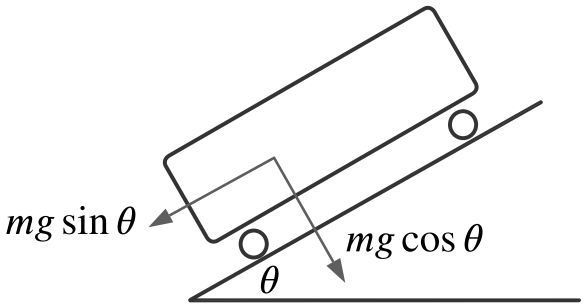


Figure 3.16: Gravitational force on a vehicle.

### 3.5.3 Curving Resistance

It can be difficult to measure and analyse the curving resistance due to uncertainties such as wheel and rail condition, lubrication and curve radius. However, in order to simplify this parameter, equation 3.39 is used [36], where the force is given Newtons per tonne of mass, and the curve radius, $r$, in meters.

$$F_c = \frac{6116}{r} \tag{3.39}$$

### 3.5.4 Plotting of the Resistance

To grasp a better understanding of the concepts described in section 3.5, a simple Matlab script was drawn in order to plot the resistive force against the speed. Since the topic of obtaining the coefficients of the running resistance is a complex one, with different doctorate thesis on mathematical models to compute them, such as Piotr Lukaszewicz's in 2001 [37], it was decided to obtain the parameters for a similar train as the one in study. It should be noted, however, that many different factors, such as the train weight, length, drag coefficients and even temporary conditions, namely rail and wheel conditions, can deeply alter the parameters. As such, the following study should be considered as an approximation of reality.

The coefficients used are from the EMU 3400 series from CP, which are commuter trains similar to series 2300/2400 [38]. They are presented in table 3.2.

In order to scale these values to the simulation and validation scale, the following approximations were made. Firstly, since each train has eight motors, the total resistive force was divided by this same number. This assumes that all motors are subject to the same force, which can be false in certain scenarios, such as when there is slip in one or more of the wheels. Secondly, a ratio between the train's motors power (393 kW) and the power of the motor to be used for validation purposes (66 kW) allows to have a scaled resistance. It was also assumed that the train wheels had the UIC standard 920 mm diameter [36]. Thus, the linear train speed can be obtained resorting to the rotational speed and wheel radius using 3.40.

$$v_{m/s} = r\frac{2\pi}{60}n_{rpm} \tag{3.40}$$

Table 3.2: Coefficients used for Plotting

| Coefficient | Value |
|---|---|
| A | 12.8 |
| B | 0.56 |
| C | 0.0558 |

The obtained plot can be observed in figure 3.17.

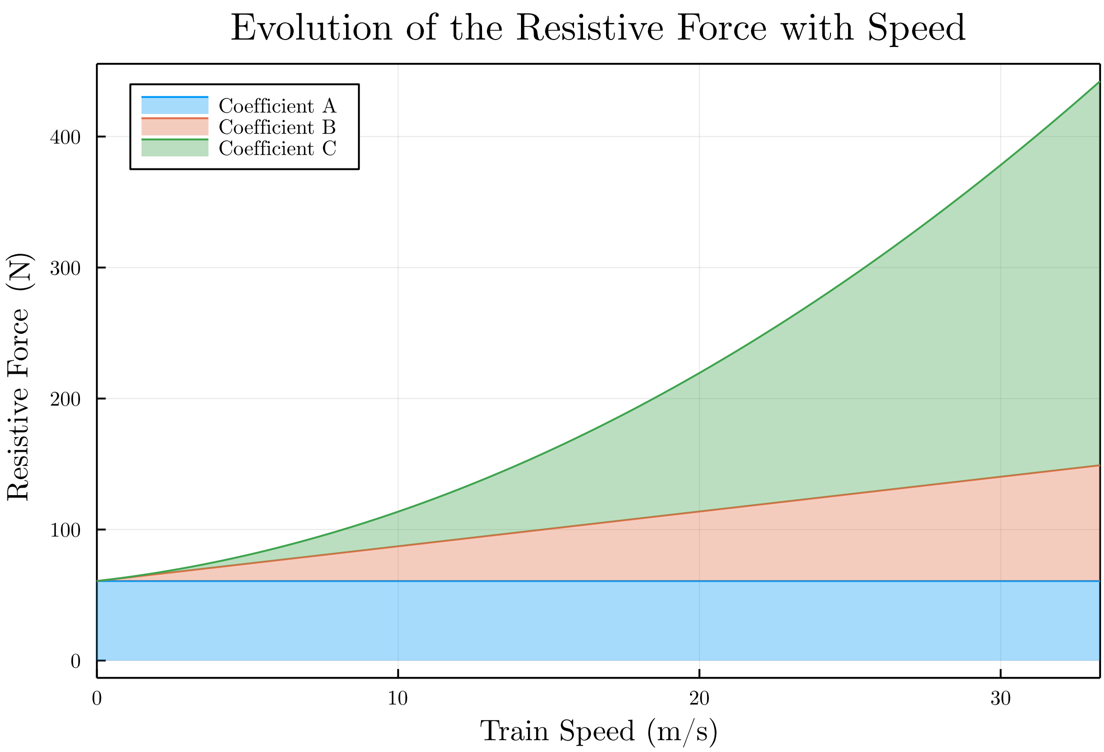


Figure 3.17: Resistive force plotted over the train's speed range.

Whilst in lower speed regions coefficient A dominates the total resistive force, the coefficient C gradually takes over the majority of the force exerted on the train, together with the coefficient B.

## 3.6 Thermal considerations

When designing a power converter, it is essential to account for the power losses of the semiconductors, which can amount to high quantities. The losses are dependent on a few operating factors, such as switching frequency or collector current.

Essentially, the power losses for an IGBT and diode group (which is the case in the study in question) can be drawn in equation 3.41. $P_{cond}$ and $P_{sw}$ stand for conduction and switching losses, respectively, while $P_b$ stand for leakage losses, usually neglected in this type of studies.

$$P_l = P_{cond} + P_{sw} + P_b \tag{3.41}$$

### 3.6.1 Conduction Losses

In order to model the conduction losses in the IGBT/diode pair, a DC voltage source, modelling the on-state collector-emitter voltage ($V_{ce}$), and a resistance in series, which models the on-state collector resistance, were used. To obtain these parameters, it is recommended to calculate a linear approximation of the collector current / collector-emitter voltage graph, under the designated gate-emitter voltage. Figure 3.18 visually demonstrates this usual method, where the collector resistance is obtained by the inverse of the slope of the curve, and the $u_{ce0}$ as the voltage value at zero current. The instantaneous power loss at the IGBT and diode is drawn in 3.42.

$$\begin{aligned} p_{ct}(t) &= u_{ce}(t) \cdot i_c(t) = u_{ce0} \cdot i_c(t) + r_c \cdot i_c^2(t) \\ p_{cd}(t) &= u_d(t) \cdot i_d(t) = u_{d0} \cdot i_f(t) + r_d \cdot i_d^2(t) \end{aligned} \tag{3.42}$$

The average power losses can be computed with the integral of the instantaneous power loss. This is shown in equation 3.43.

$$\begin{aligned} P_{ct}(t) &= \frac{1}{T_{sw}} \int_0^{T_{sw}} p_{ct}(t)dt = u_{ce0} \cdot I_{cav} + r_c I_{crms}^2 \\ P_{cd}(t) &= \frac{1}{T_{sw}} \int_0^{T_{sw}} p_{cd}(t)dt = u_{d0} \cdot I_{dav} + r_d I_{drms}^2 \end{aligned} \tag{3.43}$$

Where the currents with the suffixes *av* and *rms* are the average and root mean square of the signals, respectively. To attain the diode parameters, an analogous method should be used with the forward current / forward voltage graph.

### 3.6.2 Switching Losses

The switching losses happen at semiconductors devices due to their turning on and off intervals being a finite amount. As such, when both current and voltage are higher than zero, instantaneous power losses occur. It should be noted that these losses occur twice under each switching cycle (i.e., per cycle there are one turning on and one turning off power losses), and since the applications where the IGBTs are employed require high switching frequencies, it can be concluded that this parcel of power losses can amount to very high total losses.

In figure 3.19, simplified switching waveforms for a generic IGBT device are drawn. In the case of diodes, a very similar behaviour is to be expected. The filled areas, in blue, are the energy losses, which are the integral of the multiplication of voltage and current.

As such, the switching power losses can be calculated resorting to equations in 3.44.

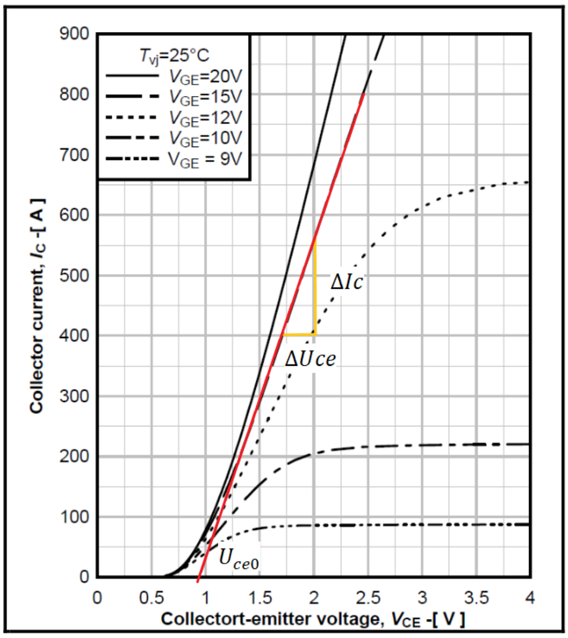


Figure 3.18: Method to obtain the on-state resistance and voltage. Edited from a Dynex IGBT datasheet [39].

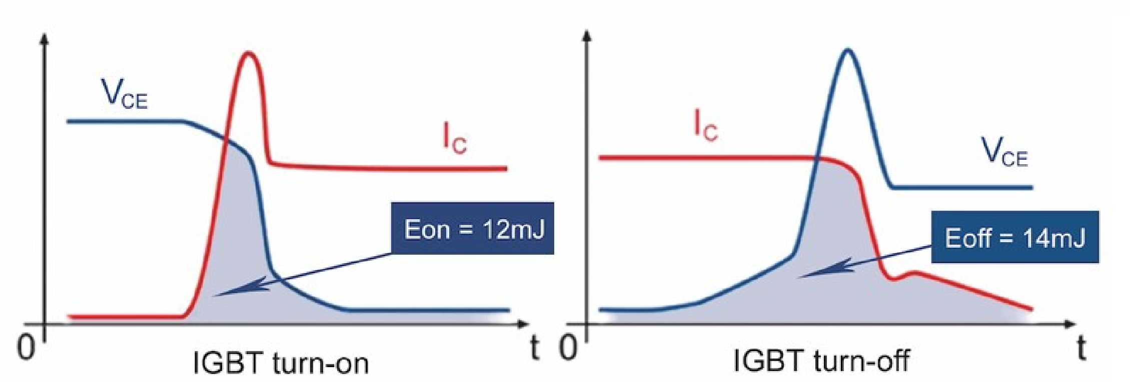


Figure 3.19: Simplified IGBT turn-on and off voltage and current waveforms. Edited from [40].

$$\begin{aligned} P_{swT} &= (E_{onT} + E_{offT}) \cdot f_{sw} \\ P_{swD} &= (E_{onD} + E_{offD}) \cdot f_{sw} \approx E_{onD} \cdot f_{sw} \end{aligned} \tag{3.44}$$

Where the switching-off losses in the diode are usually ignored.

Usually, the manufacturer indicates the turning on and off loss energies associated with the IGBT and the diode. These values should be obtained from the graphs that plot these variables against operating conditions, most notably the collector current and the junction temperature, whilst keeping in mind the conditions that the device will be subject to. In figure 3.20, a typical switching energy versus collector current plot is shown, with emphasis on the fact that these values change significantly depending on the junction temperature. It can be observed that the switching energy is higher at a higher temperature in most of the current range. As such, it can be concluded that keeping the device cool will increase its efficiency.

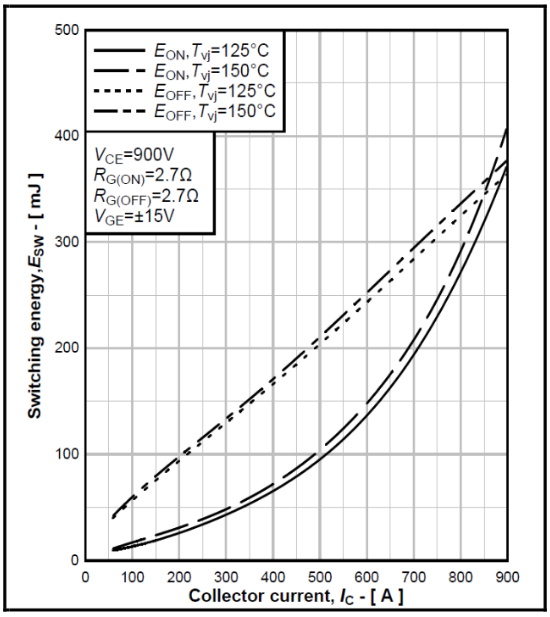


Figure 3.20: Switching energy of an IGBT plotted against the collector current and junction temperature. Taken from a Dynex IGBT datasheet [39].

### 3.6.3 Thermal Dissipation

After obtaining the total losses for the device using equation 3.41, one must proceed with the calculation of the thermal resistance needed to keep the device at an adequate temperature.

The usual procedure for this type of calculations is defining the thermal network of the setup. In the case of this study, a Foster [41] type of thermal network is used. This type simulates the flow of heat through the device using a series of RC circuits. Since there is not any data to determine the equivalent capacitors in the network, it was decided to omit these in the analysis done. In figure 3.21, a typical setup of IGBT and diode coupled with the case, heatsink and thermal paste is presented. The most important temperatures are also pointed at, namely junction temperature ($T_{junc}$), case temperature ($T_c$) and heatsink temperature ($T_h$).

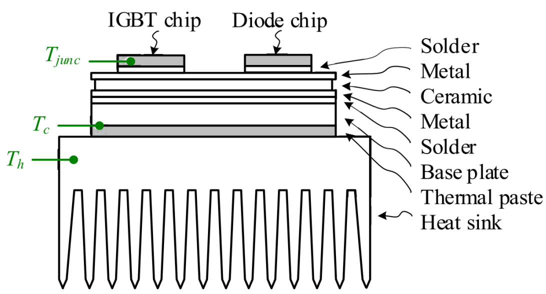


Figure 3.21: IGBT/diode module with thermal dissipation setup. Taken from [41].

The network to be studied is presented in 3.22. In it, the power dissipated by the IGBT/diode is represented by a current source. It flows from the devices to the case, and onward to the heatsink through the thermal paste. The thermal resistances of each part are represented by the equivalent electrical impedance. By solving the equations associated with this circuit, it is possible to obtain the desired temperatures at each point in the setup. It should also be noted that each device is a half-bridge, with two IGBT/diode pairs in it. For a three-phase inverter, three of these devices are required. Moreover, since they share the same heatsink, the case temperature is common to the devices.

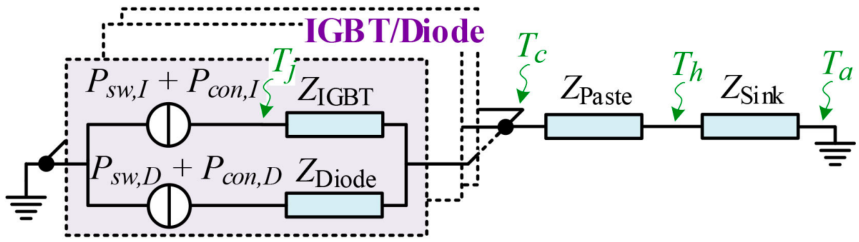


Figure 3.22: IGBT/diode modules coupled with the heatsink. Taken from [41].

The junction temperatures of the IGBT and diode can be obtained by solving the equations in 3.45.

$$\begin{aligned} T_{j,T} &= (P_{swT} + P_{ct}) \cdot (Z_{IGBT} + Z_{Paste} + Z_{Sink}) + T_a \\ T_{j,D} &= (P_{swD} + P_{cD}) \cdot (Z_{IGBT} + Z_{Paste} + Z_{Sink}) + T_a \end{aligned} \tag{3.45}$$

## 3.7 Final Remarks

In this chapter, a deeper theoretical analysis to different aspects relevant to the dissertation development was made. This study enabled a further understanding of the said topics, and to lay a foundation for the following chapter, where the control scheme is simulated.

# Chapter 4

# Software modelling and simulation

In this chapter, the software used to simulate and validate the control scheme for an Induction Motor is presented. A focus on the motor model and the power stage, an explanation of the control scheme developed and a discussion on the thermal simulation studies are done. Then, the results obtained are presented and explained, with a brief discussion regarding these.

It should be duly noted, however, that due to limitations in regards to the knowledge of the model of the actual motor equipping the series 2300/2400 train, it was decided to focus the dissertation on a scaled model. This way, in PSIM, the whole power and traction chain could be simulated and its control tuned to obtain the desired performance parameters; moreover, it is possible to emulate the expected behaviour when translating into an also scaled physical setup.

## 4.1 Subsystems

This section will be dedicated to the explanation of the subsystems used for simulating the system, namely the IM used and its testing. The power stage of the simulation model is also approached. The software used for the simulations was the Power Electronics simulation software, PSIM.

### 4.1.1 Induction Motor Model

To model the functioning of the Induction Motor, the "3-phase symmetrical squirrel-cage induction machine" block was used. It simulates the motor, using the equations shown in 3.20.

In order to validate the motor drive, it was decided to replicate a typical motor plus inverter setup at a scale, physically. With this in mind, it was deemed necessary to simulate the behaviour of the IM under the FOC schema. The motor available for the development of the dissertation works is a 66 kW 3-phase IM. Due to difficulties in accessing the motor, it was not possible to conduct the economic testing with the objective of obtaining the motor parameters. As such, a motor model with close electrical characteristics was chosen to be simulated, as a way to validate the control scheme. The parameters of the motor studied are presented in table 4.1.

Table 4.1: Induction Motor Parameters

| Parameter | Value |
|---|---|
| Rs (Ω) | 0.03552 |
| Ls (mH) | 0.335 |
| Lm (mH) | 15.1 |
| Rr (Ω) | 0.02092 |
| Lr (mH) | 0.335 |
| Poles | 4 |
| Nominal Frequency (Hz) | 50 |
| Nominal speed (rpm) | 1480 |

The torque-speed curve for the motor in study was obtained resorting to a Matlab script, where equations 3.17, 3.18, 3.19 were used. By plotting the torque computed at different slip points, the curve at figure 4.1 was obtained.

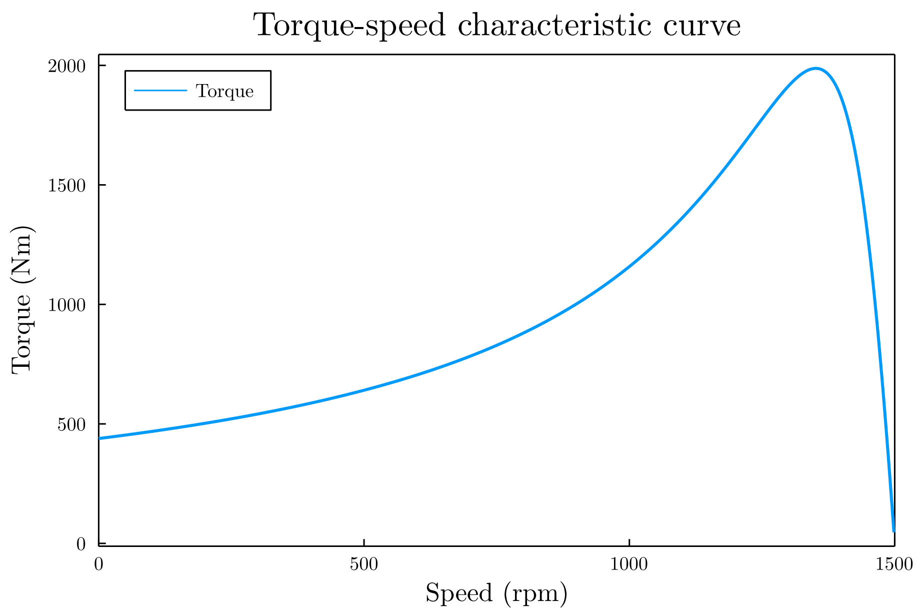


Figure 4.1: Torque-speed curve of the designed Induction Motor.

As can be observed in figure 4.1, the start-up torque of the motor sits at around 450 Nm, whilst the maximum torque is around 2000 Nm.

#### 4.1.1.1 Testing the IM

With the objective of validating the IM model to be used during the theoretical studies, a simulation was done, feeding the motor with a three-phase sinusoidal source at the rated voltage and frequency (400 V phase-to-phase, 50 Hz). It is expected to observe the motor's nominal speed at the steady state. The results are presented in figure 4.2.

After a transient period, the rotor's speed quickly stabilises to the nominal speed, at around 1480 rpm, whilst the torque produced by the motor never exceeds its theoretical maximum.

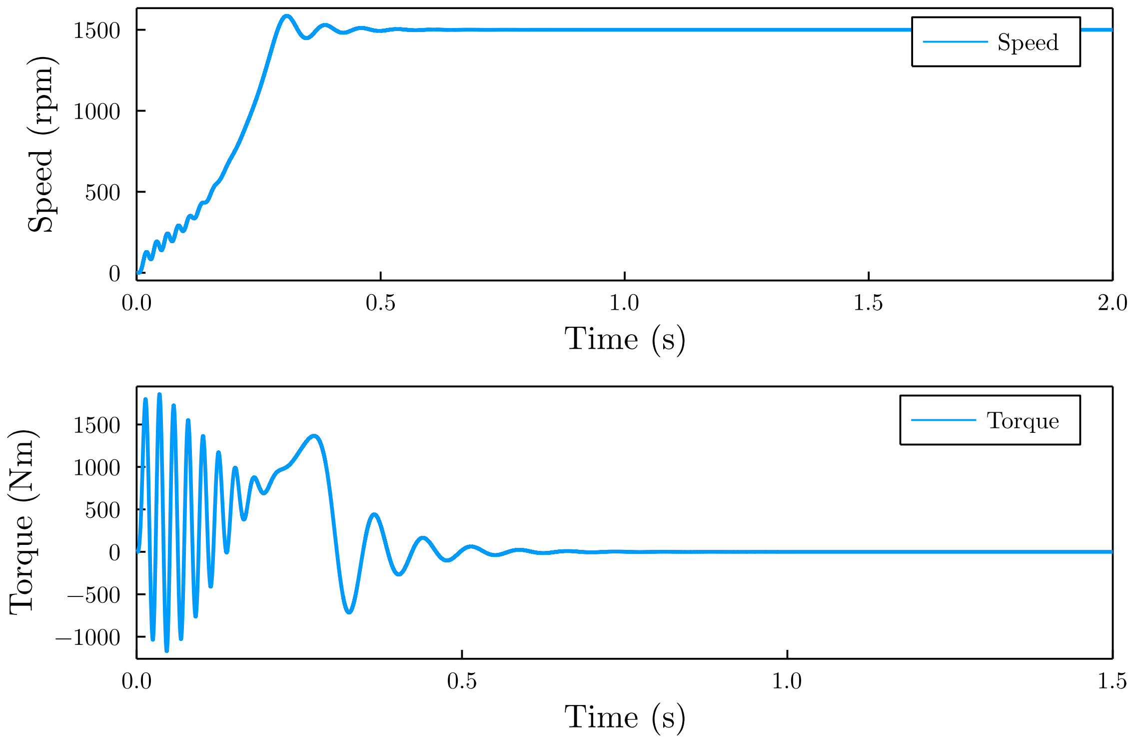


Figure 4.2: Speed and Torque of the IM with a three-phase, 400V AC source.

Another important test addresses the nominal *d*-axis stator current, which will be essential to determine its reference in the full operating range. In figure 4.3, the results of the same test applied in figure 4.2 are shown, with Park-Clarke transformation of the stator currents.

As can be noted, the *q*-axis current quickly stabilises to zero, whilst the *d*-axis current stabilises to around 62.5 A. This can be explained with the fact that the motor has no load, and after reaching its nominal speed, it no longer produces torque. Therefore, the *q*-axis current, responsible for the torque production, goes to zero, and the *d*-axis current, responsible for flux production, stabilises at the value which produces the nominal flux.

After these validations, it is possible to continue with the development of the control scheme.

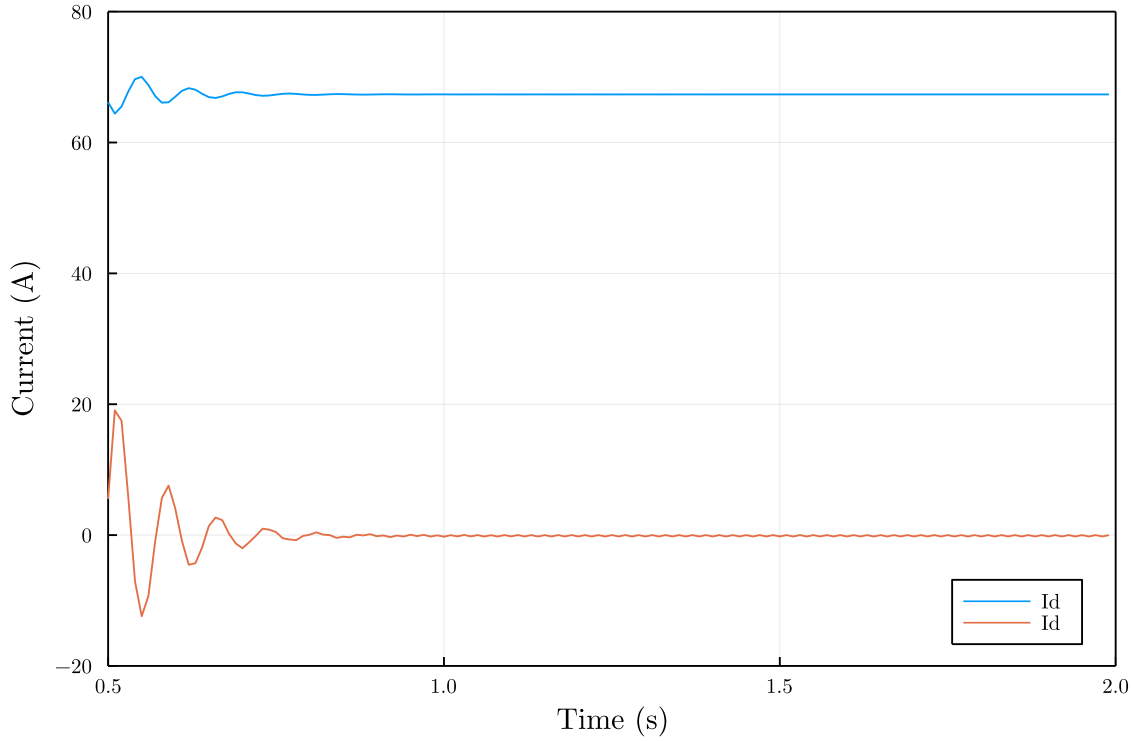


Figure 4.3: Nominal rotor flux and stator currents in the *d*-*q* frame.

### 4.1.2 Three-phase Voltage Source Inverter and Mechanical Load

A three-phase inverter, together with its gates controls and DC voltage source, was used. The outputs of this block are then connected to the stator of the Induction Motor model block. The motor's shaft is coupled to a mechanical load. Between these two blocks there are speed and torque measuring blocks. The setup can be consulted in figure 4.4.

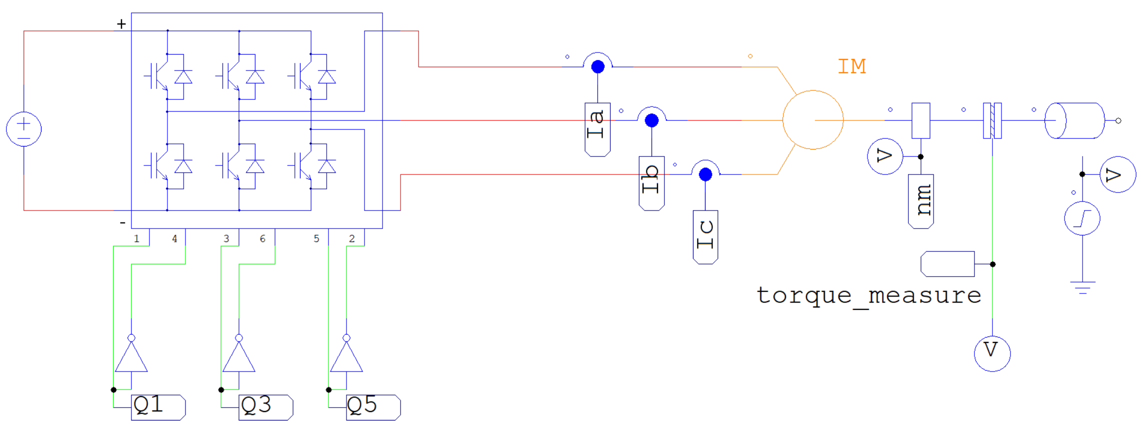


Figure 4.4: Power section of the simulation diagram.

## 4.2 Control of the Motor

In this section, a detailed overview of the control structure developed for the IM will be presented, together with thorough explanations of the design decisions made during the development process.

### 4.2.1 Reference Angle Estimation

As a consequence of IFOC, the estimation of the rotor flux angle is required for an accurate stator current control. The angle can be obtained through the integration of the rotor speed plus the slip speed. While the rotor speed is gathered with use of an encoder or resolver device, the slip must be calculated indirectly.

Since the rotor flux is aligned with the d-axis, its q-axis component is null, as shown in section 3.3. Thus, from equation 3.20, the rotor q-axis voltage can be written as eq. 4.1:

$$V_{qr} = R_r i_{qr} + \frac{d\lambda_{qr}}{dt} + (\omega - \omega_r)\lambda_{dr} = R_r i_{qr} + (\omega - \omega_r)\lambda_{dr} = 0 \tag{4.1}$$

Thus, the slip frequency can be obtained in eq. 4.2.

$$(\omega - \omega_r) = \omega_{sl} = -\frac{R_r i_{qr}}{\lambda_{dr}} \tag{4.2}$$

Where the rotor q-axis current can be written as eq. 4.3.

$$i_{qr} = -\frac{L_m}{L_r} i_{qs} \tag{4.3}$$

The rotor q-axis flux can also be written as eq. 4.4, where $p$ denotes the differential operator

$$\lambda_{dr} = \frac{L_m}{1 + T_r p} i_{ds}, \; T_r = \frac{L_r}{R_r} \tag{4.4}$$

Finally, the slip frequency is obtained by eq. 4.5.

$$\omega_{sl} = (\frac{1}{T_r} + p)\frac{i_{qs}}{i_{ds}} \tag{4.5}$$

If the rotor flux linkage is kept constant, then equation 4.5 can be simplified to eq. 4.6.

$$\omega_{sl} = \frac{1}{T_r}\frac{i_{qs}}{i_{ds}} \tag{4.6}$$

The rotor flux angle is estimated by the integration of the summation of the rotor angular speed and the slip frequency, as seen in eq. 4.7.

$$\theta = \int (\omega_{sl} + \omega_r) dt \tag{4.7}$$

The obtainment of the reference angle is essential to the referential transformations applied in the control scheme.

### 4.2.2 Flux and Torque Estimation

As described in section 3.3.1, a flux and torque estimation technique is essential to the control scheme. For its simplicity and robust behaviour in mid to high speed regions, the back-emf integration method was chosen. In figure 4.5, the PSIM schematic for the flux estimation can be found.

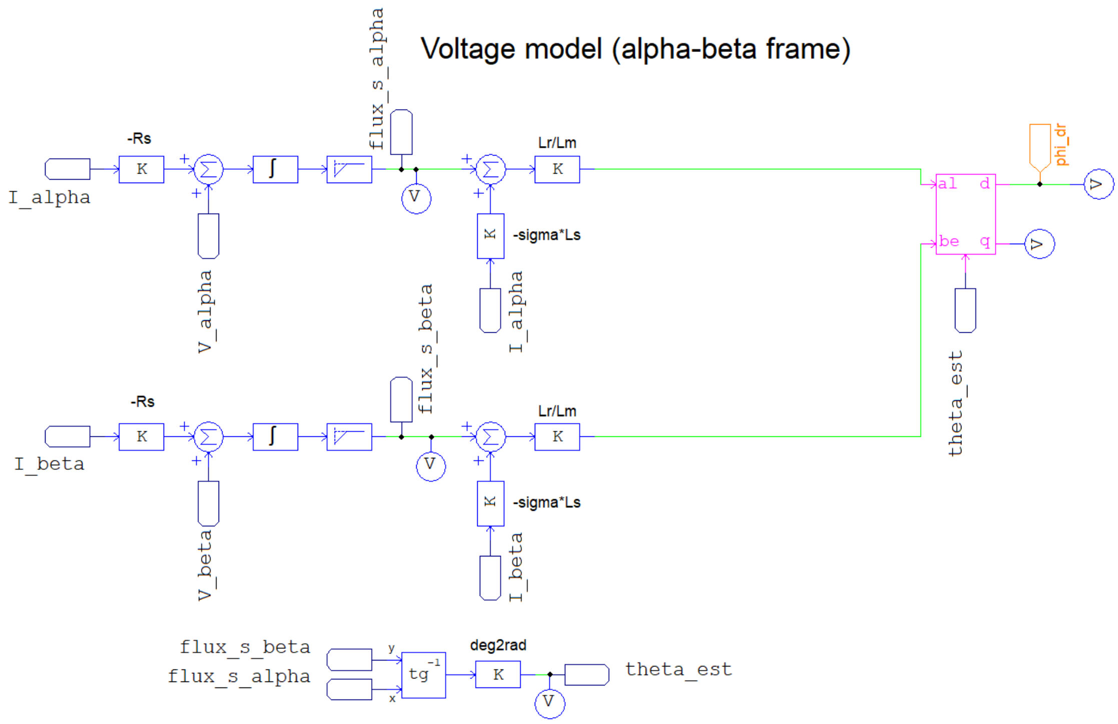


Figure 4.5: Flux estimation schematic in PSIM.

It should be duly noted that, even though a high-pass filter was used to compensate the integration drift and measuring offsets errors, it is also possible to use a low-pass filter in replacement of the setup, as shown in equation 3.27. The latter option is more suitable for a digital implementation.

With regards to the torque estimation, equation 3.26 was used to estimate it. The calculation also employed a compensation factor which fixes the attenuation of the high-pass filter present in the flux estimation scheme.

The biggest drawback of the back-emf estimation method is the low-speed region, where the method suffers from estimation errors due to low levels of back-emf. In figure 4.6, the issue is reported, where the flux estimation is inadequate in speeds under 50 rpm. This effect, in its turn, distorts the torque estimation, which leads to poor control performance in the aforementioned speed region. To fix this problem, the torque estimation used to control the motor switches depending on the speed at which the rotor is spinning. Under a certain rpm level, the torque estimation uses the nominal flux. After this level, the flux estimation is used. This prevents the described issue, whilst also avoiding high-speed deviation errors, which will be discussed in section 4.5.

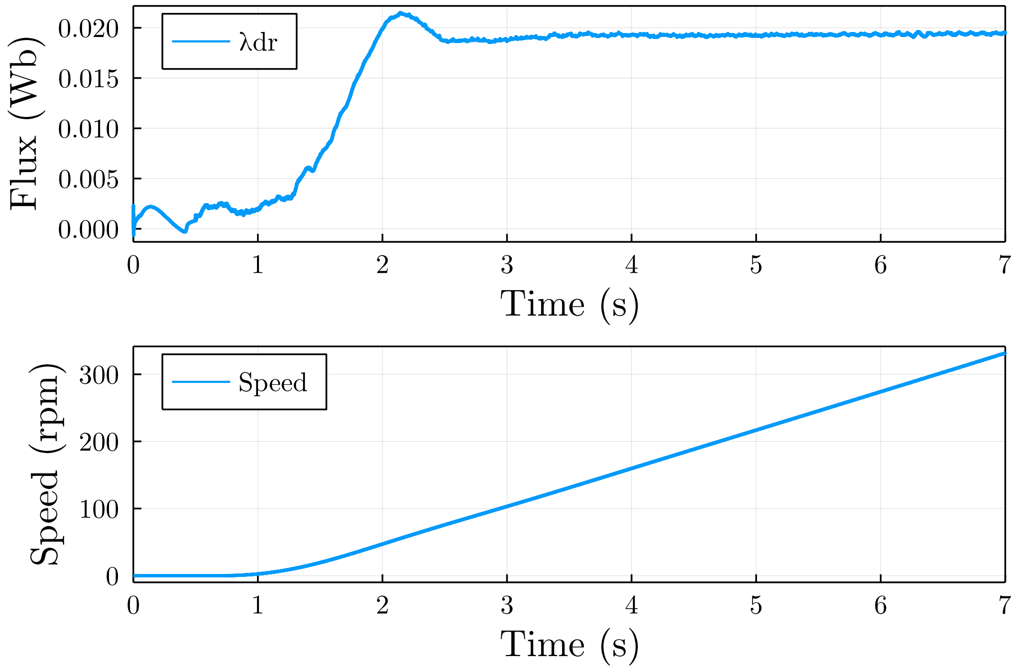


Figure 4.6: *d*-axis rotor flux simulation, together with the current rotor speed.

### 4.2.3 Discretization, Sampling and Switching Frequencies

With the objective of turning the simulation closer to the physical experiments setup, the control scheme was discretized based on a few principles. Firstly, since the switching frequency is limited to 1200 Hz, it was chosen to run the PI controllers at a frequency of at least 2400 Hz. This way, it is ensured that the SVPWM block is always updated with new voltage reference values, as opposed to getting the same references twice. Furthermore, the stator currents and speed must be sampled at a rate higher than twice of the rate of the control loop, to ensure a stable operation, obeying the Nyquist theorem.

The stator currents are filtered before being sampled. For this purpose, it was necessary to employ a 1st order Low-Pass filter, with a cut-off frequency set at 120Hz, equivalent to a decade before the switching frequency. This assures that the switching noise present at the currents is effectively eliminated. The Bode plot of the filters is presented in fig. 4.7. It can be noted that the filter applies a small phase shift (of 22.7 degree) to its inputs in the ranges of frequencies of the stator currents (around 50 Hz), considered to be adequate.

The control and acquisition loops were implemented in *C* code, in order to facilitate the transition from simulation to microcontroller implementation.

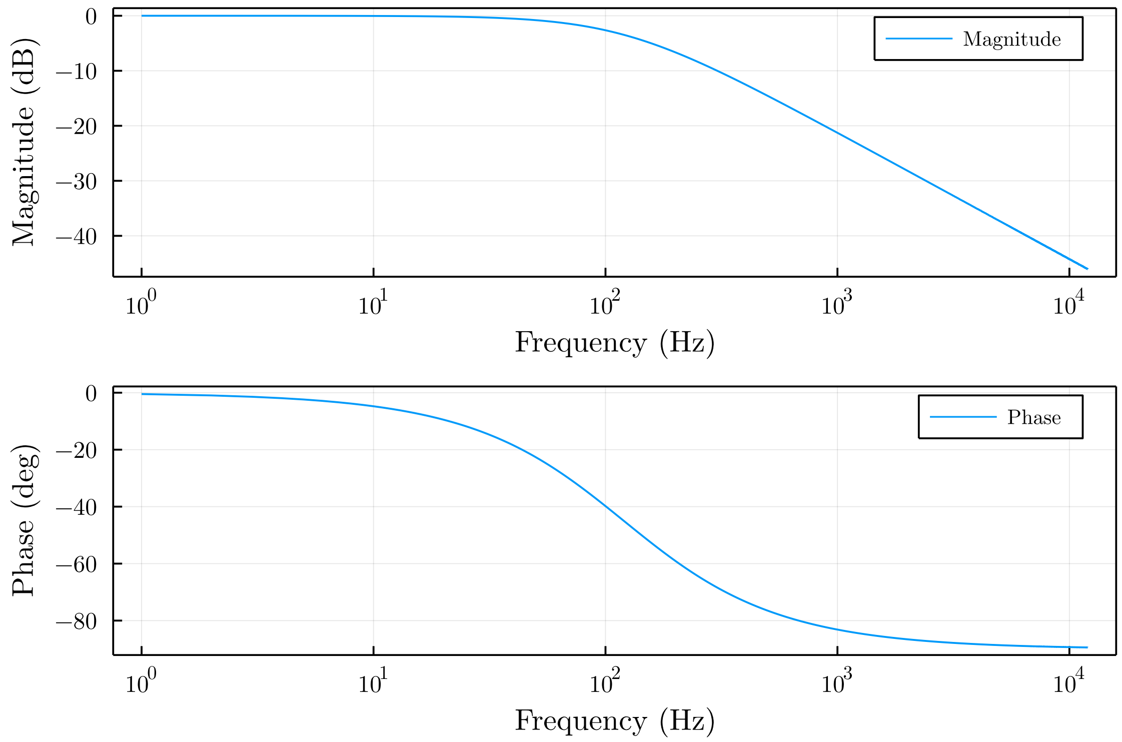


Figure 4.7: Bode plot of the Low-Pass filters used in the simulations.

#### 4.2.3.1 PI Controller Discretization

A typical continous parallel controller structure is presented in figure 4.8.

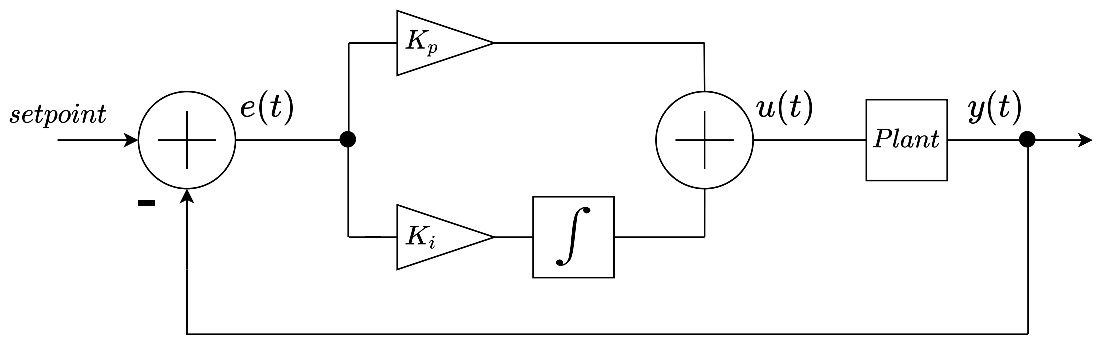


Figure 4.8: Typical parallel PI controller structure.

To discretize the PI controller, a trapezoidal error approximation was used. In figure 4.9, a graphical representation of the discretization process is presented, where the error between sampling periods is determined to be the area of the trapezoid marked between consecutive samples, demonstrated in equation 4.8, assuming the sampling time is constant (which is the case in the control routine employed).

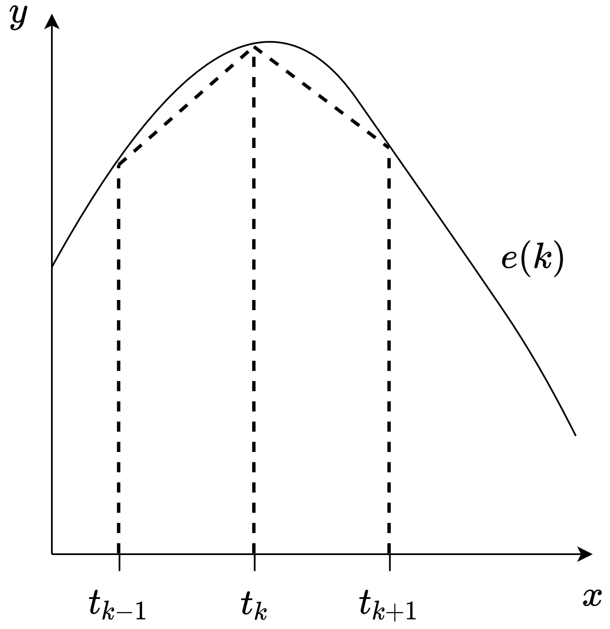


Figure 4.9: Error trapezoidal approximation graphical representation.

$$A = \frac{B+b}{2} \cdot h \leftrightarrow \int = \frac{e_k + e_{k-1}}{2} \cdot t_k \tag{4.8}$$

The expression for the output of the PI controller is obtained through the bilinear transformation of the continuous time domain expression, as shown in equations 4.9 and 4.10.

$$\frac{U(s)}{E(s)} = K_p + \frac{K_i}{s} \rightarrow s = \frac{2}{T_s}\frac{z-1}{z+1} \leftrightarrow \frac{U(z)}{E(z)} = K_p + K_i \frac{T_s}{2}\frac{z+1}{z-1} \tag{4.9}$$

$$\begin{aligned} U(z) &= z^{-1}U(z) + K_p(E(z) - z^{-1}E(z) + K_i \frac{T_s}{2}(E(z) + z^{-1}E(z)) \\ u[k] &= u[k-1] + K_p(e[k] - e[k-1]) + K_i \frac{T_s}{2}(e[k] + e[k-1]) \end{aligned} \tag{4.10}$$

When the controller's output absolute value is higher than the beforehand set limit, it gets limited to it, and the integral part will continue to grow, leading to poor performance under this scenario. This is called integrator windup, and can be solved with anti-windup schemes. In the case used, the anti-windup implemented eliminates the proportional and integral outputs of the PI controller. This means that the output of the PI controller is equivalent to its previous output, whenever the anti-windup scheme is activated.

### 4.2.4 Current and Torque Control

In figure 4.10, it is possible to observe a simplified schematic of the controller developed for the IM. Most notably, the torque and current controllers follow a cascaded control logic. In order to be able to maintain a good control over these variables, it is necessary to take caution with the bandwidth of the controllers. The outer controller must be significantly slower than the inner controllers, for the cascaded loop to be effective. In fact, while tuning the proportional and integral gains for them, this aspect was fundamental.

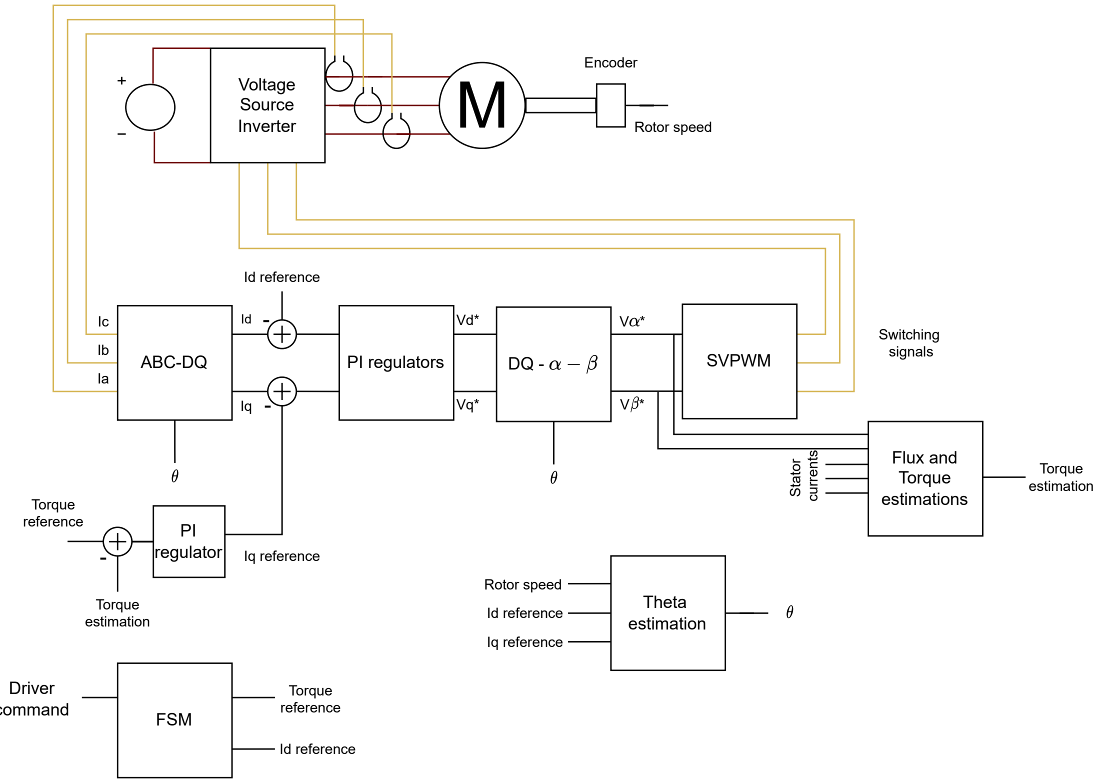


Figure 4.10: Field-Oriented Control schematic used.

It should be duly noted that the accuracy of the torque estimation is essential to the overall system behaviour. Typically, a control system reads a physical variable and calculates the error against its reference. In this case, since a torque sensor is not readily available nor is it present in the train, it was necessary to develop a torque estimation scheme.

### 4.2.5 Train Control

In figure 4.11 the FSM for controlling the movement of the train is presented, where the inputs from the train driver are transformed into torque and current references. It is known that the driver controls the torque produced by the motors by actuating a lever, which is represented in the FSM as a floating point value between -1 and 1, where -1 indicates maximum braking torque and 1 maximum accelerating torque. The value 0 is interpreted to lead to coasting the train, thus leading to a null torque command.

Each state has the following outputs:

- *State 0* : State used to model the stopped train. Torque reference is set to zero, and direct current reference ($Id_{ref}$), the flux setting component, set to its nominal value.

- *State 1* : State used to model the train under acceleration. Torque reference is set to the nominal torque times the command value, limited to the nominal torque, $Id_{ref}$ set to its nominal value.

- *State 2* : State used to model train acceleration at flux weakening region. Therefore, torque is limited to the constant power region (see figure 2.2, region 2); its value is dependant on the train current speed, and maximum power. $Id_{ref}$ follows a descendant trajectory depending on the ratio of the current speed and nominal speed ($Id_{ref} = \frac{n}{n_{rated}} \cdot Id_{nom}$).

- *State 3* : State used to model the train coasting. Torque reference is set to zero, whilst $Id_{ref}$ is set to its nominal value.

- *State 4* : State used to model braking mode. Torque reference is set to maximum torque times the command received, and the $Id_{ref}$ at its nominal value.

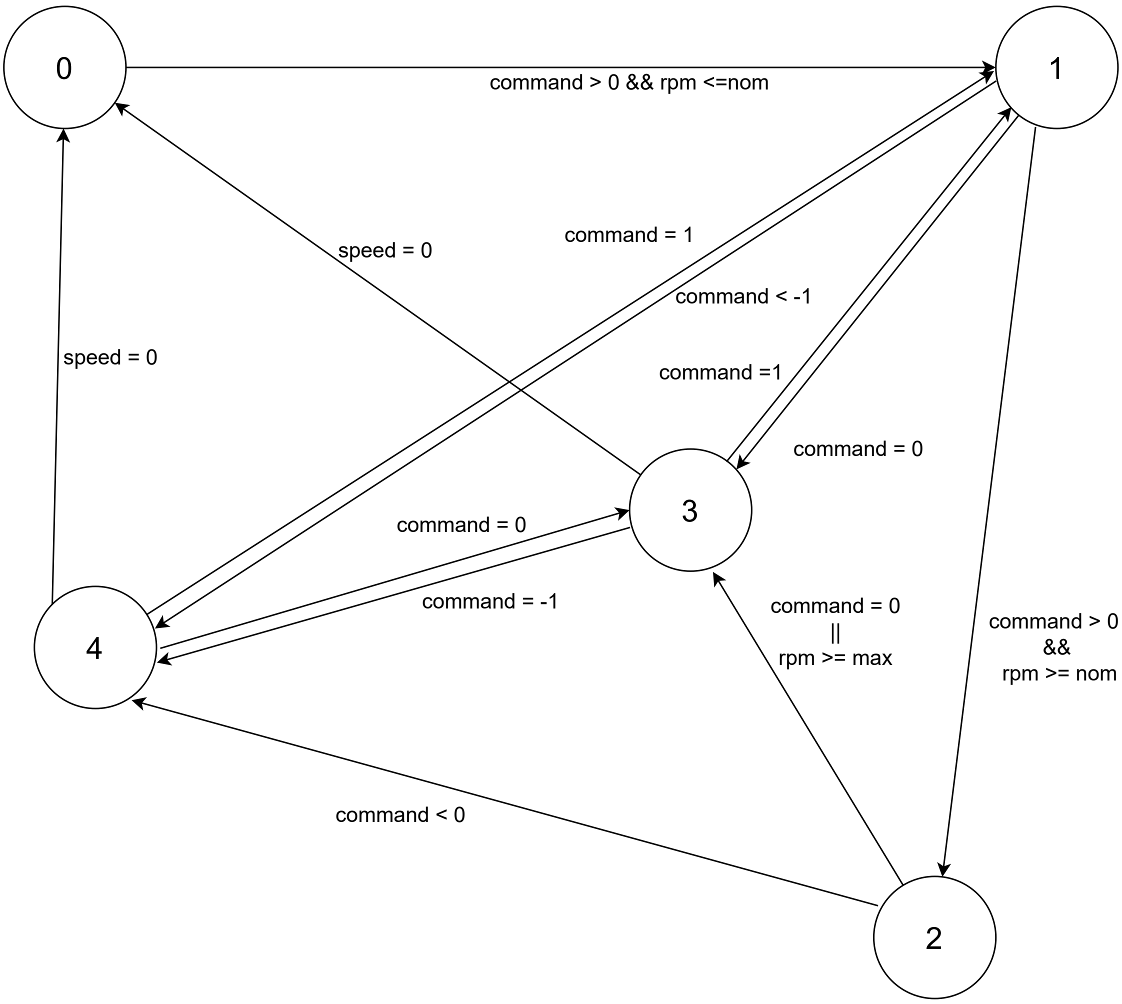


Figure 4.11: Finite state machine used to model different train states.

## 4.3 Thermal Study

In order to obtain the IGBT model very close to reality, the graphs plotting different variables should be used, such as the examples in figures 3.18 and 3.19. For this purpose, the PSIM software provides tools to replicate these curves into the software, in case the semiconductors to be simulated are not included in the default libraries. This assures the maximum accuracy in replicating the actual devices.

### 4.3.1 Setup for the Three-Phase Inverter

In the scope of the dissertation, a three-phase inverter was built following the 3D render presented in fig. 4.12.

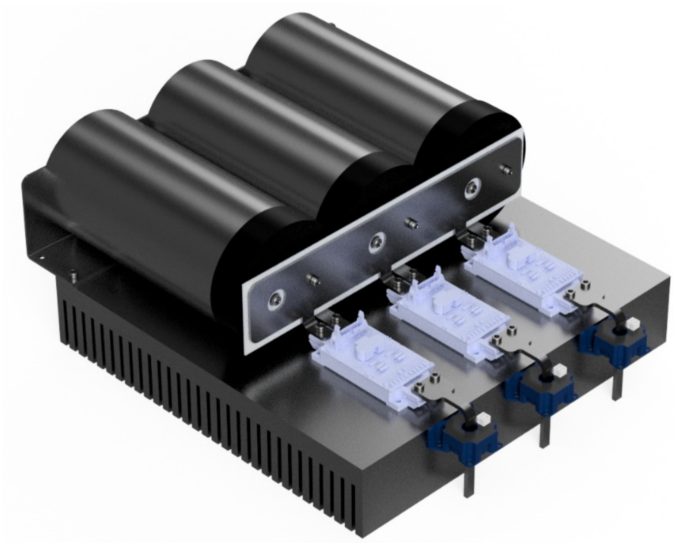

Figure 4.12: 3D render of the built three-phase inverter.

The half-bridge IGBT/diode modules used were Dynex's TG 450HF17M1-S300 [39]. The DC link capacitance was set to 1800 $\mu F$, with three 600 $\mu F$ capacitors in parallel. It is indicated that the maximum junction temperature of the package is 150°C. The values of the thermal resistances are presented, defined as the amount of heat contained in the said material when a unit of energy flows through it, in table 4.2.

Table 4.2: Thermal Resistances of the Devices used

| Resistance (°C/kW) | Diode | IGBT |
|---|---|---|
| Junction-Case | 95 | 55 |
| Case-Heatsink | 48 | 28 |
| Heatsink-air | 35 | |

### 4.3.2 Semiconductor and Thermal Network Model

The first step done to obtain the simulation results was to use the "thermal module" block, that simulates the IGBT, and joining them in a "H-bridge" configuration, as shown in figure 4.13. The heatsink thermal resistance was also added, with the ambient temperature represented as a DC voltage source, set to 40°C. The starting IGBT junction temperature was set to the same value. The six IGBT, in the field of thermal dissipation, are seen as six devices in parallel producing thermal power transfered to the heatsink. It should be noted that the thermal resistances of the junction-case and case-heatsink of each device are represented internally in the IGBT models. All thermal resistance values were set according to table 4.2.

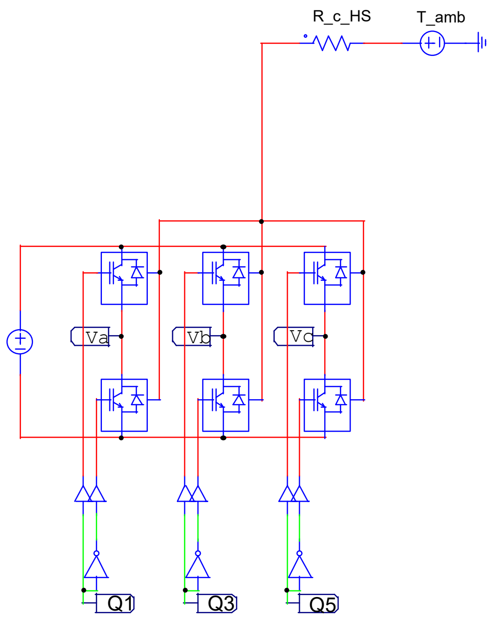


Figure 4.13: Three-phase H-bridge with the thermal modules, together with the heatsink thermal circuit.

## 4.4 Current Control Results

In figures 4.14 and 4.15, the simulations of the current controllers can be observed. They consist of setting the *d*-axis current reference to its nominal value (62.5 A) at the beginning of the simulation, and a *q*-axis current reference of 100 A at 1 s. This way, the response of each individual controller can be analyzed, as well as the cross-coupling effects. The controllers developed achieve their purpose of a stable operation, whilst having a quick settling time (at around 20 ms), and an acceptable overshoot (of around 25 %). Another result is the cross-coupling effect of the *q*-axis current in the *d*-axis one. When the *q*-axis current overshoots, this effect is noted in the opposite current, even though it is a very small effect.

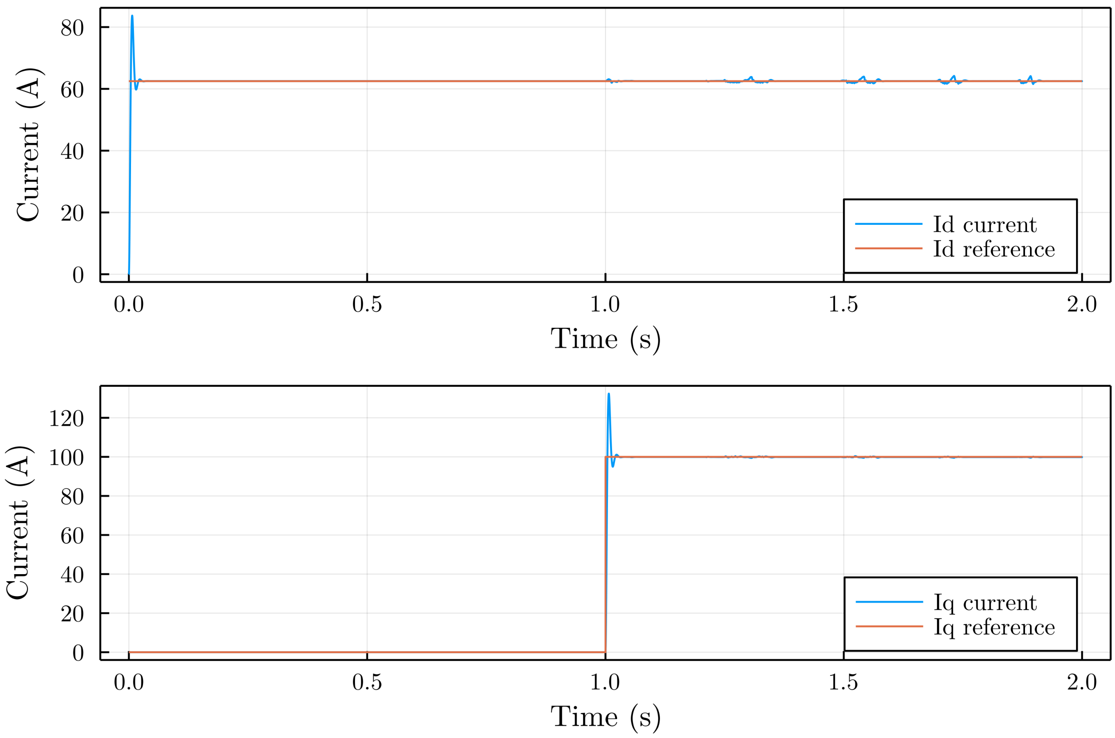


Figure 4.14: Current control in the *d*-*q* frame.

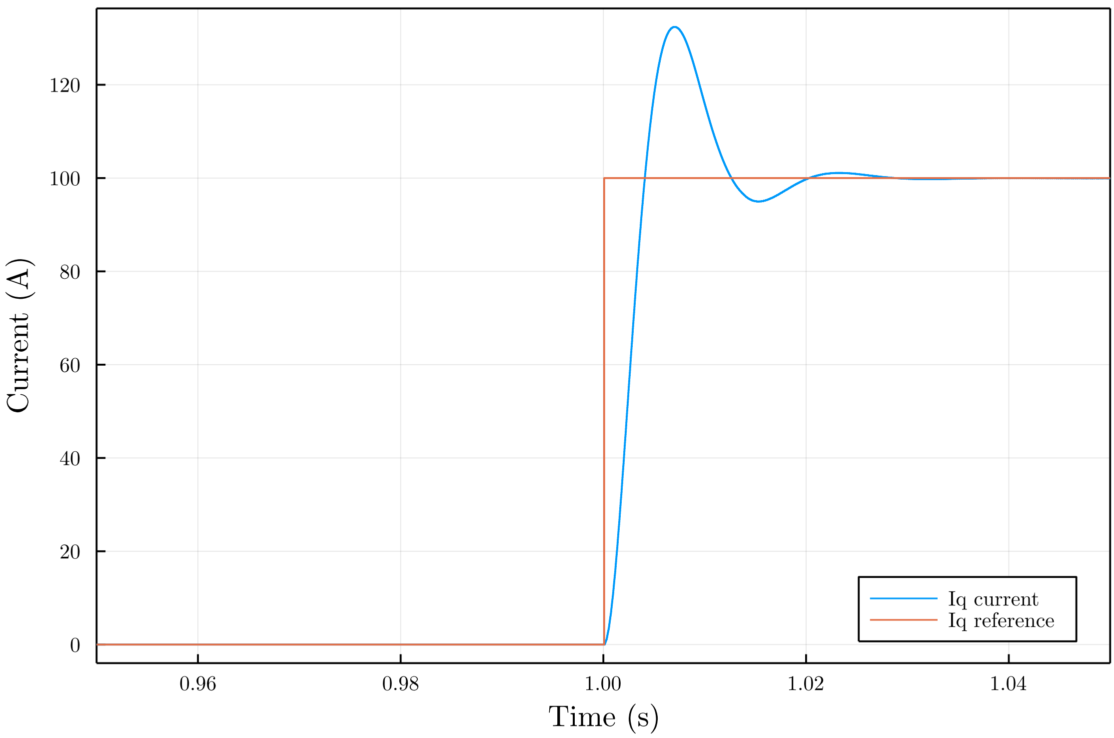


Figure 4.15: Detail of the transient response of the current controller.

## 4.5 Torque Control Results

To ensure a smooth operation in all speed regions, the following torque estimation strategy was developed. Since the flux estimation, under the back-EMF scheme, is poor at low speeds, it was decided to replace the torque estimation using this flux estimation with a constant flux, kept at its nominal value. This way, the torque behaviour is much more stable at lower speeds. It was also found that, at high speeds, the latter estimation was also not adequate, since the rotor flux value increases with higher speeds. These concepts can be seen in figure 4.16, where the pink line indicates the moment when the torque estimations are switched (i.e., when the flux estimation used for the torque estimation switches).

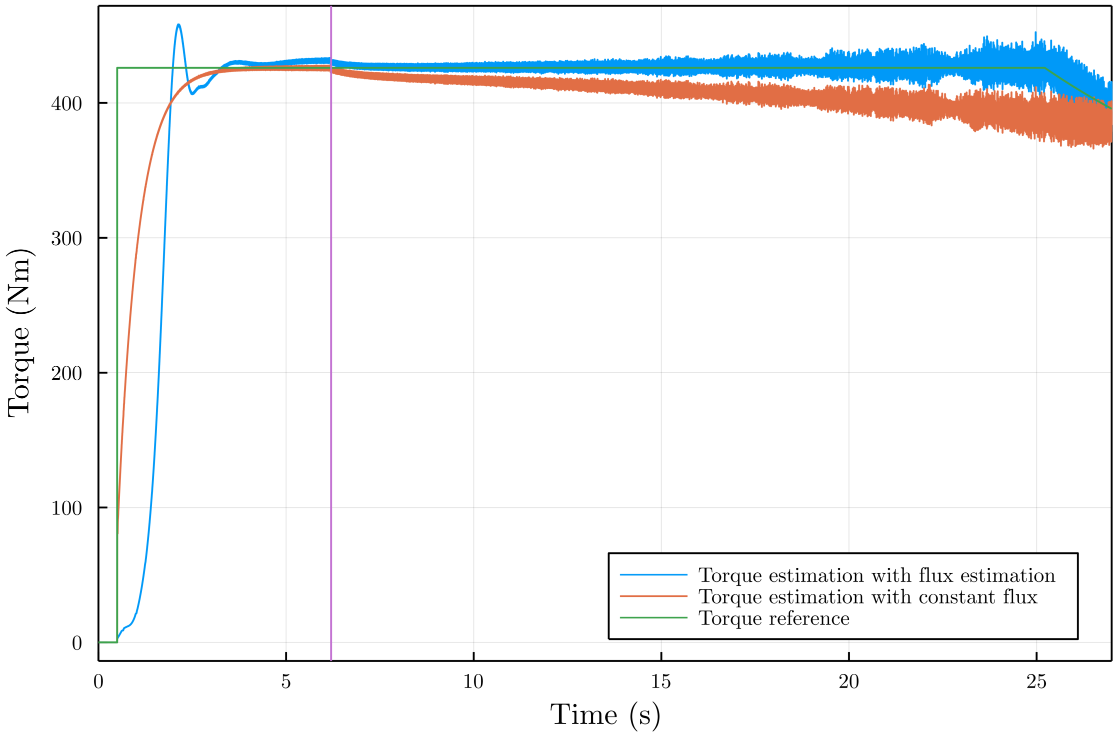


Figure 4.16: Different torque estimation techniques and their behaviour over time.

To test the torque control scheme, a command step to the nominal torque was applied at 0.5 s. The value for the torque was obtained resorting to equations 4.11 and 4.12, where the nominal motor power, $P_{rated}$, was set to 66 kW, and the nominal speed, $n_{nominal}$, to 1480 rpm. The mechanical load used was of a constant torque type, of 100 Nm, and had a moment of inertia value of 50 $kgm^2$.

$$P_{rated} = \frac{2\pi}{60} n_{nominal} T \tag{4.11}$$

$$66 \cdot 10^3 = \frac{2\pi}{60} 1480 \cdot T \leftrightarrow T = 425.85 \tag{4.12}$$

The results of the torque control are presented in figure 4.17. Firstly, the average value of the torque follows the reference in its entirety. The settling time was projected to be a maximum of 5 s, and the control fulfills it by achieving a settling time of 3 s. It can also be noted that the current controllers, whose result is in figure 4.14, are over a decade faster, resulting in a smooth cascaded control. Figure 4.18 shows the speed and electrical power produced by the motor during the simulation. When the rotor speed achieves the motor's rated speed, the field weakening region begins, where the power produced by the motor stays constant. In this region, the torque produced is commanded by equation 4.13.

$$T_{ref} = \frac{60}{2\pi n} \cdot P_{rated} \tag{4.13}$$

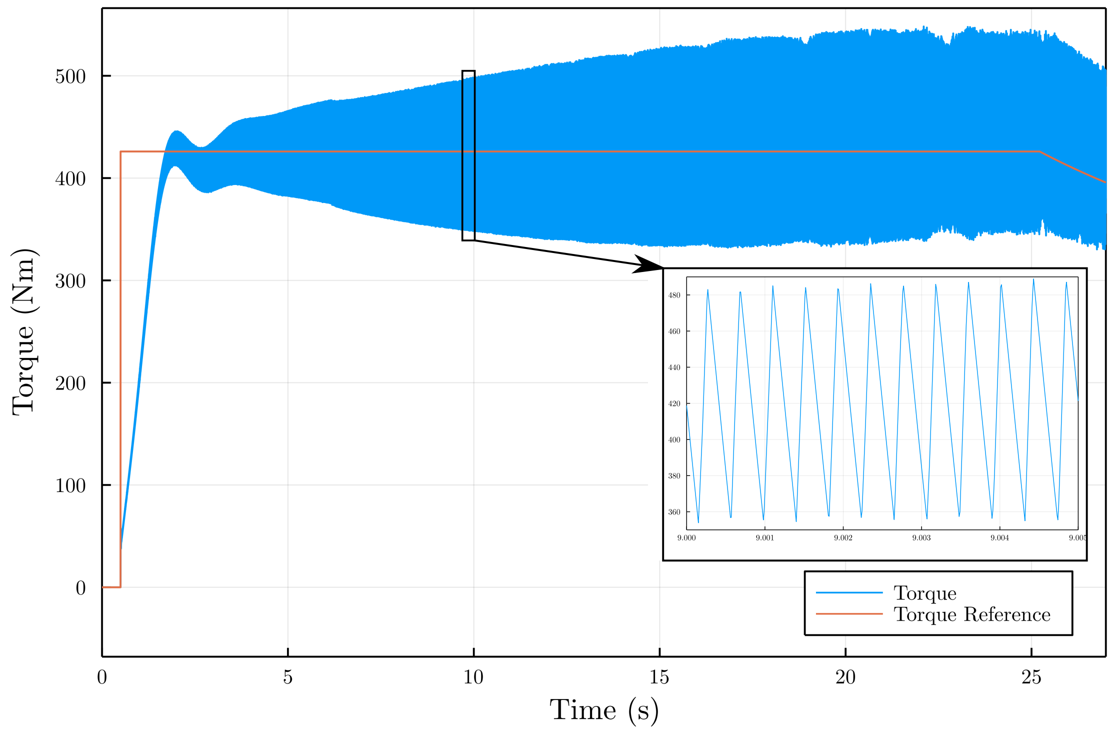


Figure 4.17: Torque produced by the the motor during a torque control simulation. Detail to the shape of the torque ripples.

The torque produced also presents a high amount of ripple, that generally increases with the increase in speed. At its worst, there is a peak-to-peak ripple of 200 Nm. This can be explained by the fact that the switching frequency is set to a relatively low value (1200 Hz), but also because the parameters of the motor do not enable a lower amount of torque at the current operating conditions.

To demonstrate this supposition, two arguments are presented. Firstly, a simulation with a higher switching frequency (2400 Hz, double the original frequency) is shown in figure 4.19. In it, there is a 105 Nm peak-to-peak torque ripple, which is approximately half of the ripple in the simulation with the lower frequency.

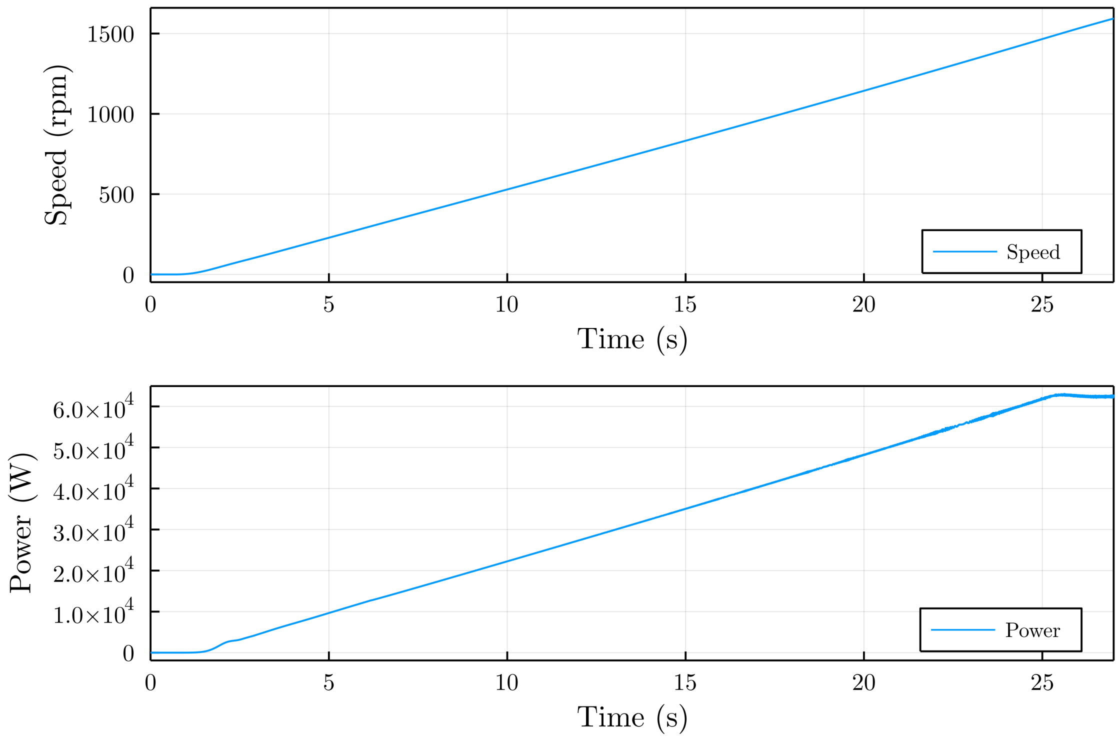


Figure 4.18: Speed and power of the motor during a torque control simulation.

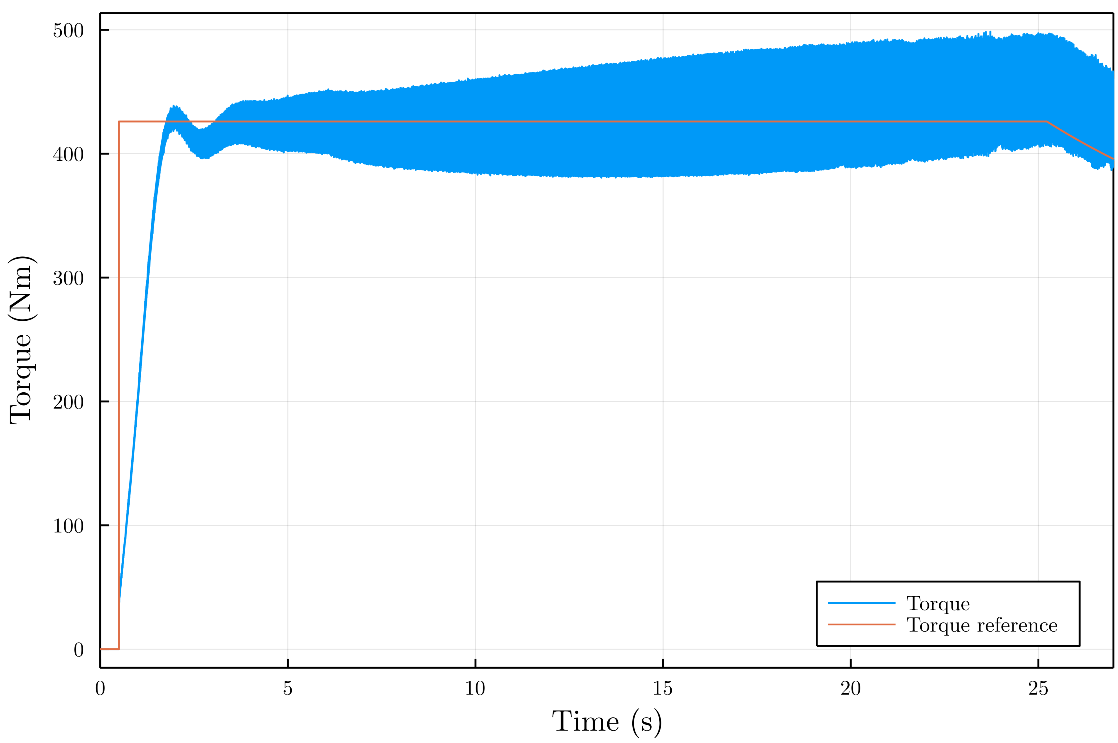


Figure 4.19: Torque control simulation with a higher switching frequency.

The second argument presented is based on the simulation with an estimation of the parameters of the IM intended to be used in the physical setup. By feeding only one phase of the motor, the rotor does not spin, thus providing an approximately equal setup as of the one in figure 3.6.

By calculating the impedance and phase shift of the current versus the voltage, it is possible to obtain the impedance phasor, which is equal to the total impedance seen in figure 3.6. It was assumed, based on IEEE Standard 112, that the rotor and stator reactance values are equal, and that the stator reactance is 3 % of the magnetizing reactance. The last step to obtain an approximation of the values of the parameters was to employ an iterative algorithm, where the current assumed parameters values were used to calculate the current value under the applied voltage, and the error between the calculation and the actual current value was minimised through iterative sequences.

The relevant IM parameters and characteristics are presented in table 4.3.

Table 4.3: Induction Motor Estimated Parameters

| Parameter | Value |
|---|---|
| Nominal Voltage (V) | 400 |
| Synchronous Speed (rpm) | 1000 |
| Nominal Frequency (Hz) | 50 |
| Rs (Ω) | 0.1875 |
| Ls (H) | 0.0061 |
| Rr (Ω) | 0.0267 |
| Lr (H) | 0.0061 |
| Lm (H) | 0.0157 |

Figure 4.20 demonstrates the reduced torque ripples with the simulation obtained with the estimated motor parameters. They are greatly reduced, whilst keeping the exact same control scheme used for the previous motor model, and using a switching frequency of 1200 Hz.

The two arguments presented indicate that the torque ripple seen in fig. 4.17 is external to the control scheme employed; it is suggested that it is due to the motor model, namely the stator time constant. While comparing the motor parameters from table 4.1 to the parameters in table 4.3, it can be noted that the stator time constant of the first one is 9.43 ms, whilst the second one is 32.53 ms. This indicates that the first model allows for faster current changes; it also indicates that it is more sensitive to lower switching frequencies. Thus, since the current oscillates faster, the torque will consequently oscillate faster as well.

This effect is clearly visualised in figure 4.21. In it, the torque ripples can be seen as an effect of the IGBTs gates signals. Depending on the signals and, consequently, the voltage applied at the IM's stator, the torque ascends or descends. This, in turn, oscillates at the switching frequency rate. The slope of the oscillation is a direct effect of stator time constant.

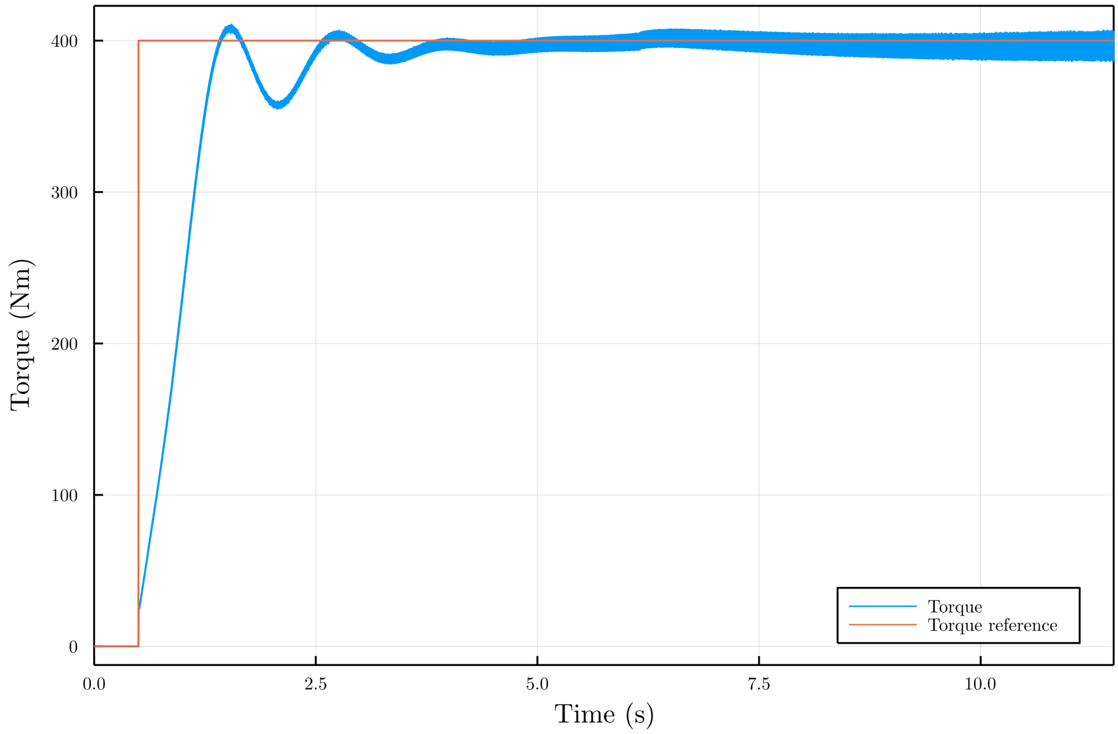


Figure 4.20: Torque produced by the the motor during a torque control simulation.

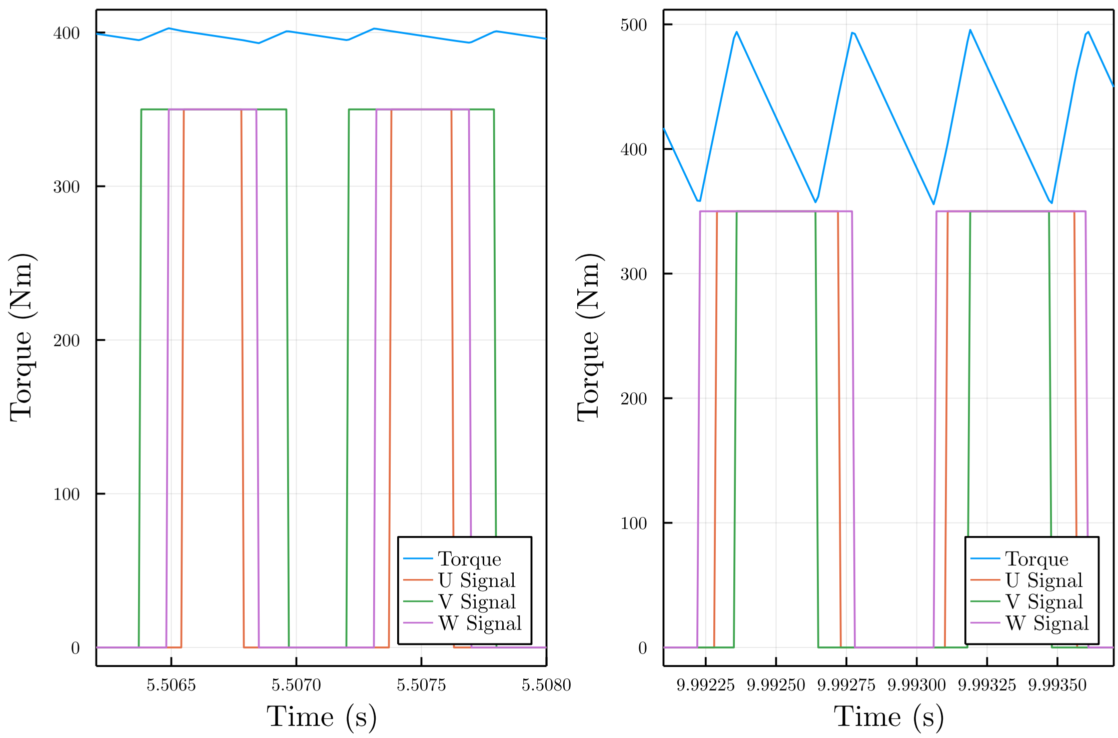


Figure 4.21: Torque produced by the the motor plotted against the three IGBT gates signals. On the left, the motor is the one described at table 4.3. On the right, the motor is described at table 4.1.

## 4.6 Regenerative braking and Train Control Results

To demonstrate the regenerative braking and functioning of the FSM presented in fig. 4.11, figure 4.22 displays the torque and its reference; figure 4.23 exhibits the speed the rotor is spinning at, complemented by the signal that actuates the train and the corresponding state. Lastly, in figure 4.24 the three-phase stator currents are shown, whilst figure 4.25 shows the currents at a higher detail, together with the outputs of the currents filters.

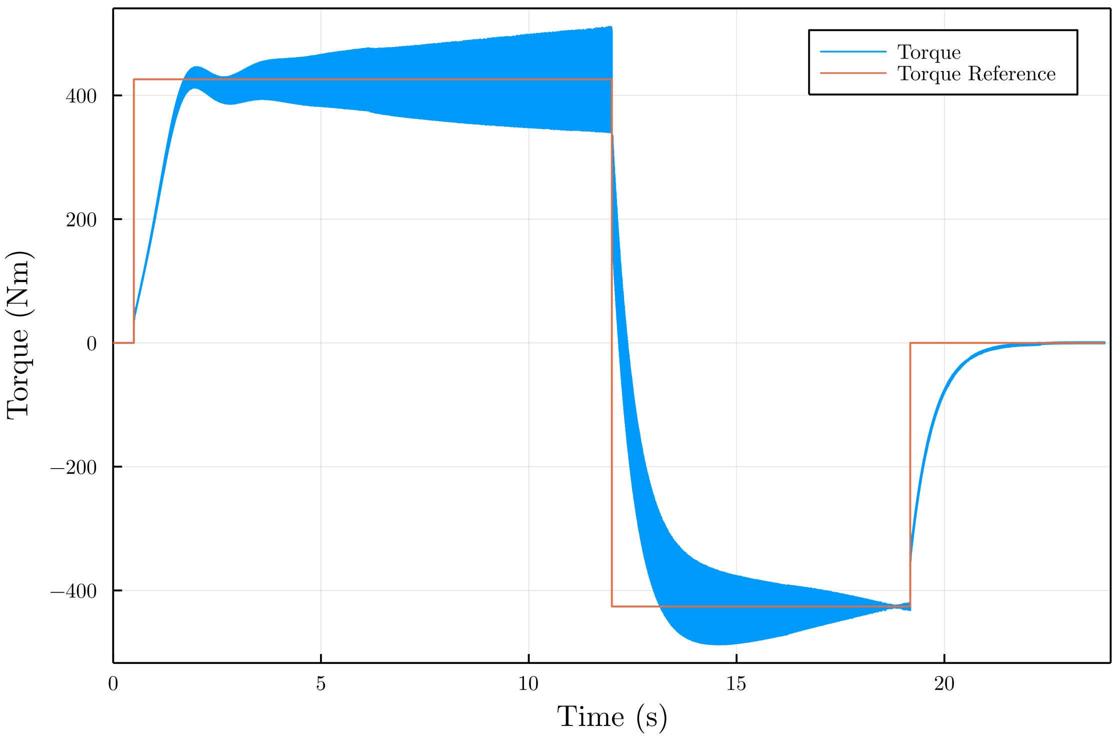


Figure 4.22: Torque produced by the the motor during a torque control simulation.

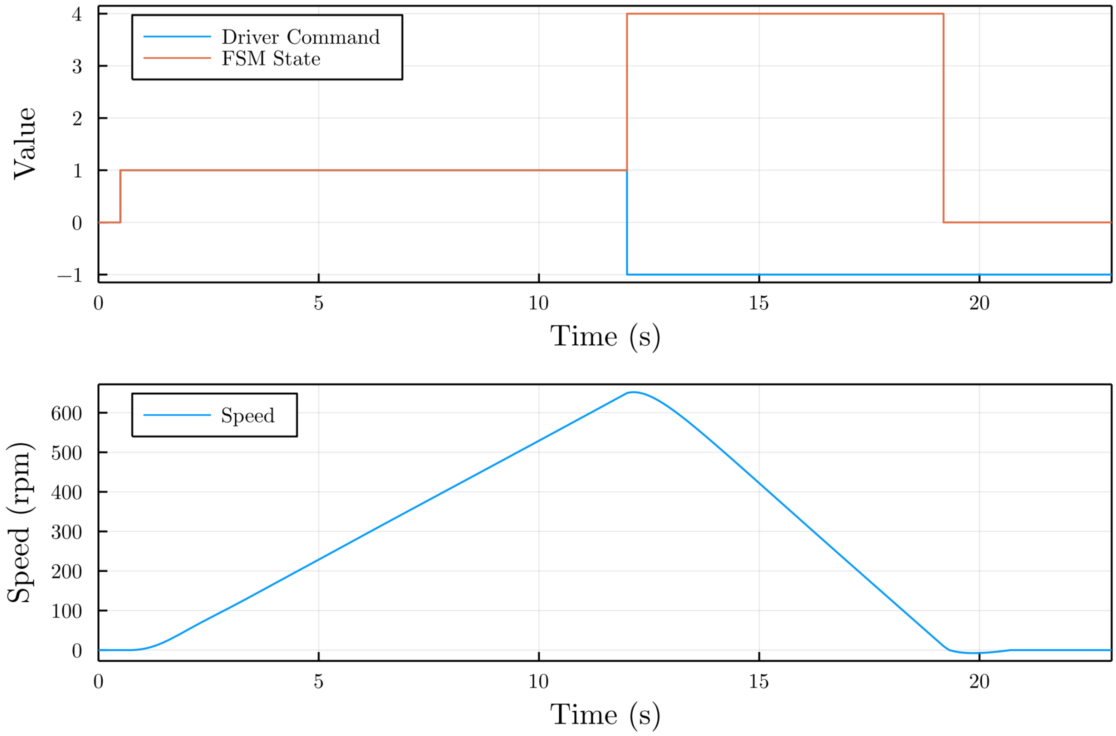


Figure 4.23: Speed at which the rotor spins, the driver command and the FSM state.

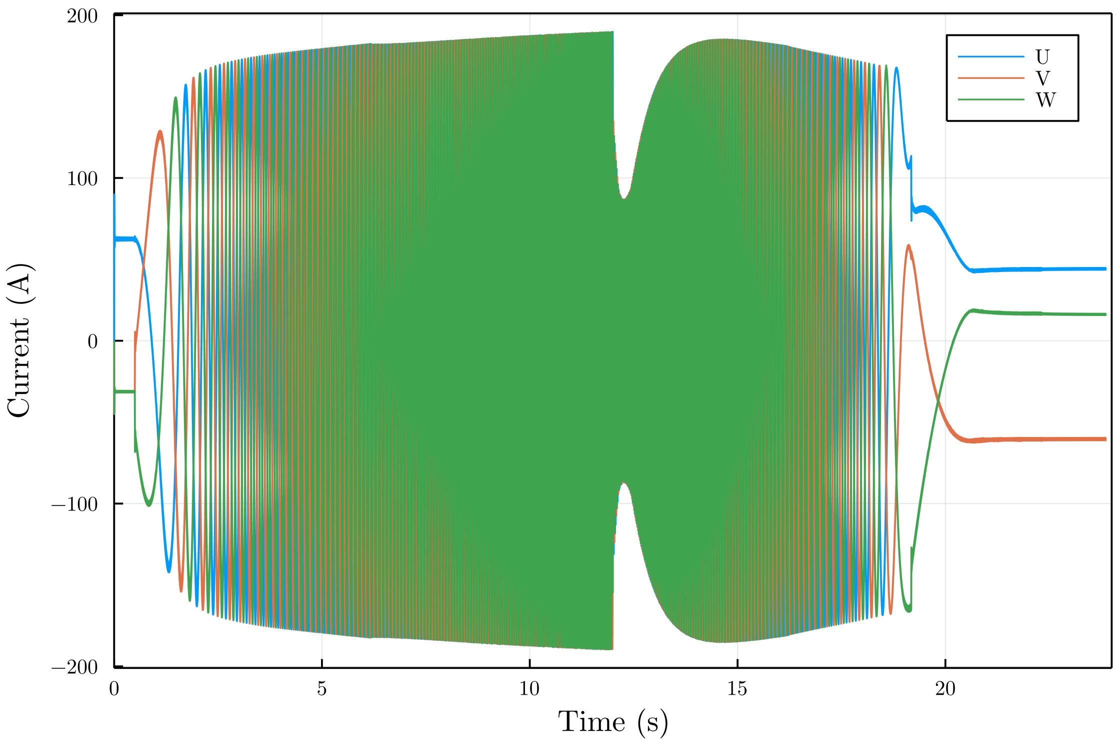


Figure 4.24: Stator currents during braking simulation.

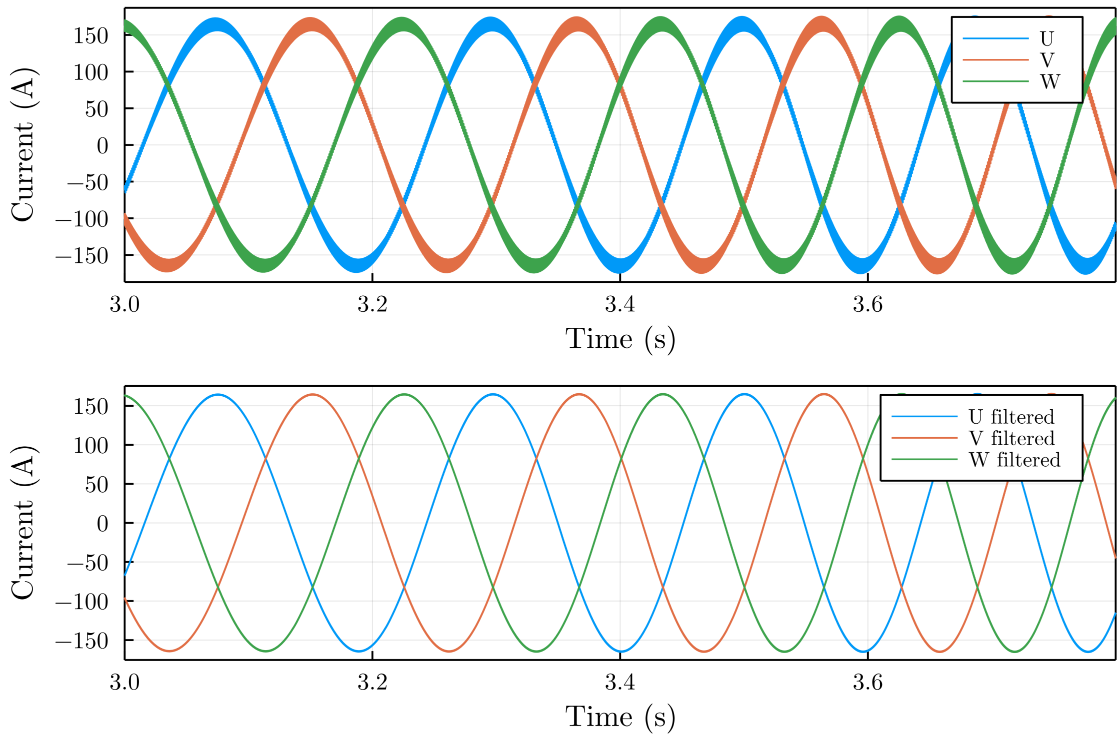


Figure 4.25: Closer look at stator currents during braking simulation. Top figure shows the unfiltered current, while bottom figure shows filtered currents.

The performance under regenerative braking is shown to be good, with the controllers ensuring a fast response, whilst keeping the system stable. In figure 4.23, the FSM functioning can be observed. After the driver command goes to -1, the FSM changes its state to number 4, which is reponsible for the braking state. After the speed reaches zero, the state is once more switched to the number 0, equivalent to the initial, or stopped, state.

The settling time from the zero torque command to nominal torque is the same as with the test in fig. 4.17, while the settling time from the nominal torque to minus nominal torque is slightly lower, at 2.3 s. The waveform of the response is also different; this can be explained by the fact that, at the second command step, the flux is already settled, while at the first command the flux rises and settles at the same time as the torque. Since the IM requires nominal flux to function adequately (expect in the field weakening region), its performance is changed whenever the flux is not at this value. Another aspect that can be noted is the torque ripples changing according to speed. As said previously, the ripples increase with the speed; until the 12 s mark, the speed increases and so do the torque ripples; after the torque reference is changed to a negative value, the speed decreases, and the torque ripples decrease accordingly.

The unfiltered currents demonstrate the correct functioning of the three-phase inverter and its control. The variation in frequency and amplitude of them follow the evolution of the speed and torque of the IM. The filtered currents show the signals that enter the controller do not have the switching frequency noise present in the unfiltered currents.

## 4.7 Thermal Studies Results

In figure 4.26, the results of the thermal studies are presented. The total power dissipated tops at 1280 W, and each IGBT produces around 213 W when the motor is developing its nominal power. The junction temperatures of both the transistor and diode are kept well below their safe threshold value of 150 °C, and the case (heatsink) temperature peaks at 85 °C. The transistor's junction temperature goes higher than the diode's, presumably due to higher power dissipation.

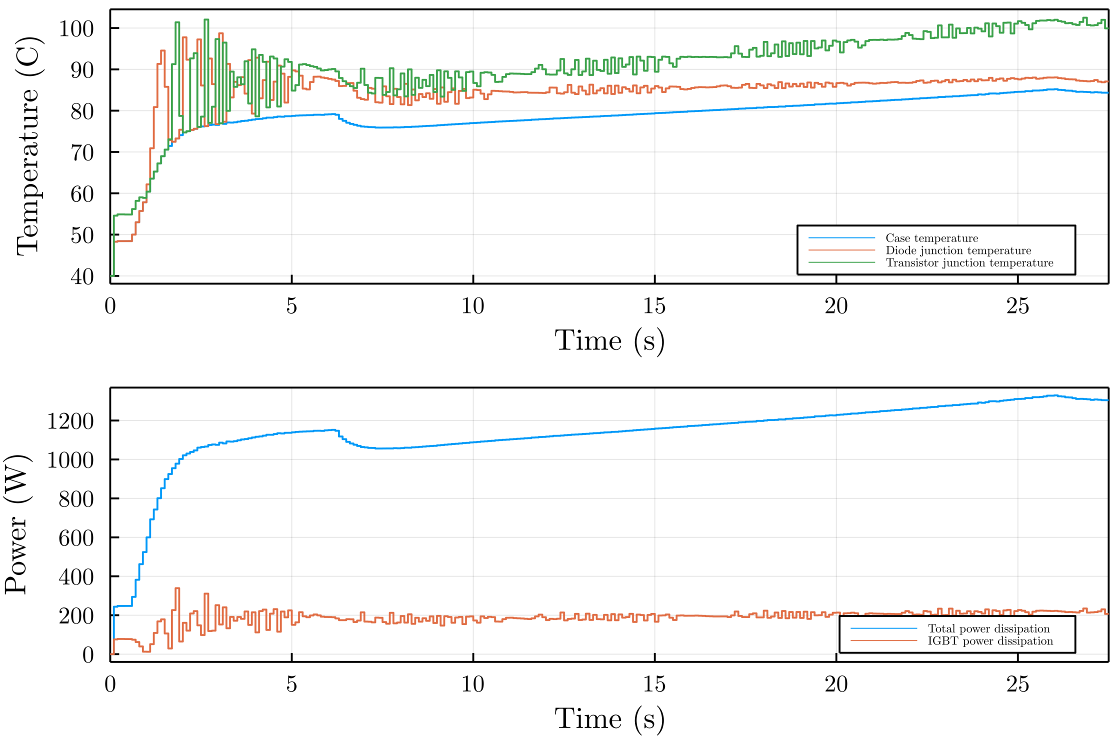


Figure 4.26: Power dissipated by the three-phase bridge (top) and Transistor, Diode and case temperatures (bottom).

With the power values drawn, it is possible to have remark on efficiency. If one defines it as the ratio between the power the IM is producing and the dissipated thermal power, then equation 4.14 establishes the efficiency.

$$\eta(\%) = \frac{66000 - 1280}{66000} \cdot 100 = 98.06\% \tag{4.14}$$

## 4.8 Final Remarks

In this chapter, through the detailed explanations of the control architecture assembled and the following results demonstration, a preliminary validation of the motor control scheme was performed. Indeed, the first step in controlling the motor is the stator's current control, having achieved a stable and fast control. The torque control closes the loop on the motor drive, setting also a fast response, but also not presenting any significant overshoot, ideal for a train application. Overall, the results obtained are considered to be within the stipulated performance benchmarks, thus being possible to continue with the studies; in chapter 5, an experimental validation is performed.

It can also be noted that, with the preliminary motor parameters obtained experimentally, the torque ripples drastically reduce; therefore, it can be concluded that the control results should improve in the future.

The thermal studies results validate the thermal management solution developed for the test bench, ensuring safe temperatures in all devices even at higher power outputs. The high efficiency value obtained proves once more the utility of the IGBT devices used as a serious alternative against the older GTO semiconductors.

# Chapter 5

# Physical validation

This chapter will focus on the experimental work during the dissertation period. The purpose of the developments was to physically validate the control scheme developed, detailed in chapter 4.

Firstly, a brief exposition on the hardware used is made, together with some descriptions of them. Afterwards, there is a focus on the main points of the microcontroller programming development. Lastly, the main results of the work developed are presented and discussed.

## 5.1 Test Bench

Within this section, the used experimental setup will be detailed. A few aspects will be explained, namely the Power Electronics topology, the VSI, its DC link voltage and the devices chosen to build it.

### 5.1.1 Induction Motor and Load Motor

The setup developed for the testing of the IM is presented in figure 5.1.

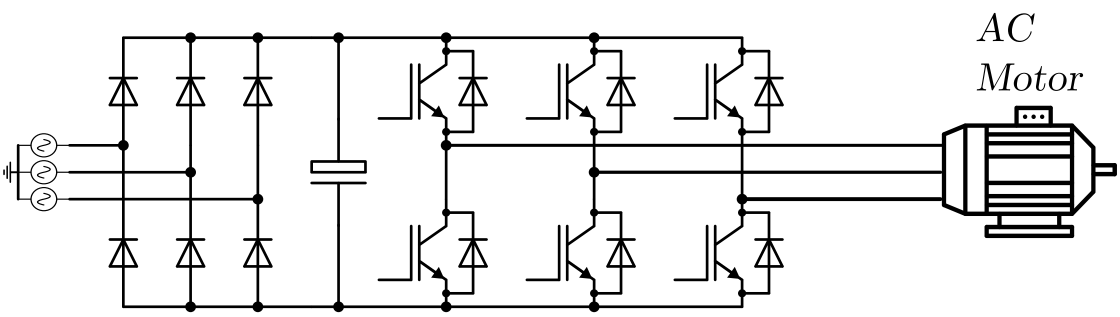


Figure 5.1: Setup for testing the IM.

The IM is fed through a created DC link voltage, that consists of a rectified and smoothed out voltage. The three-phase VSI, together with the microcontroller commands, impose the desired behaviour onto the IM.

### 5.1.2 Voltage Source Inverter

The three-phase Voltage source inverter was built around the Dynex IGBTs TG450S300, [39], which have a 1700 V 450 A rating. Since the motor to be used has a nominal current of 125 A (see equation 5.1), these devices are adequate to their use.

$$I_{nom} = \frac{66k}{400\sqrt{3} \cdot 0.87 \cdot 0.88} \tag{5.1}$$

For validating the code developed, it was decided to first use a passive load, detailed in section 5.4. Moreover, to obtain lower and, consequently, safer voltage values, the setup in figure 5.2 was used.

The DC link voltage was built around the three-phase grid voltage, whose voltage is adjusted through a three-phase variac, and then rectified with a diode bridge. This voltage is then smoothed out with the 3 DC link capacitors (600 $\mu F$ each). The schematic used can be observed in figure 5.2.

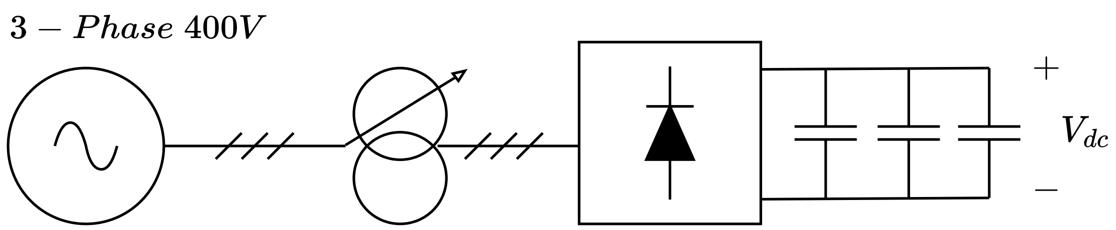


Figure 5.2: Schematic used for obtaining the DC link voltage.

### 5.1.3 Semiconductors Drives

The IGBT drives used were the Power Integrations SCALE-2, [42]. They were configured in a Half-Bridge mode, where the A input is the gate signal for the IGBTs (it is negated and applied a dead-time to it for the lower IGBT), and the B input acts as an enable, thus raising the security levels of the application. The gate resistors were chosen based on the IGBT used and the recommendation on the driver's datasheet.

### 5.1.4 Sensorization

To measure the three-phase currents, three LEM LF 205-S sensors were used. They are 200A rms current transducers.

To condition and acquire the signals, a PCB from a different project was adapted for this purpose. The main purpose of the circuit is to provide a midpoint offset to the signals acquired. Since negative currents would result in negative measurements, and the XMC4500 only accepts voltages in the ranges of 0-3.3 V in its ADC ports, this step is crucial for the correct utilization of the microcontroller. It was also necessary to adjust in the code the bias and gain of these signals, by comparing the measurement taken with an oscilloscope with the debug screen of the program. The DC voltage was also acquired and monitored. Moreover, the PCB ensured the transmission of the IGBT driver signals through fiber optic, simulating the setup in the train. Another PCB was developed to transform these optic signals into electrical signals, suitable for the drivers.

## 5.2 Microcontroller Programming

Following the C code developed for the PSIM simulations, it was necessary to implement different strategies to adapt to the microcontroller integrated development environment.

The main differences between the two software in question are the way filters are implemented and routines/timing interrupts.

In this section, relevant topics will be approached regarding the development of the software.

### 5.2.1 ADC Filtering

Due to the level of noise contained in the ADC acquisitions, namely the switching frequency ripple present in the VSI's output currents, it was necessary to employ digital filtering in these same measurements.

In order to apply filters in the digital domain, a few concepts must be tackled. The $z$-domain transfer function of a typical digital filter is seen as equation 5.2.

$$H(z) = \frac{b_0 + b_1 z^{-1} + b_2 z^{-2} + \ldots + b_N z^{-} N}{1 + a_1 z^{-1} + a_2 z^{-2} + \ldots + a_M z^{-M}} \tag{5.2}$$

The order of the filter is determined by the highest value of M or N.

The equation in 5.2 can also be described by a difference equation, as shown in eq. 5.3

$$y[n] = b_0 x[n] + b_1 x[n-1] + \ldots + b_M x[n-M] - a_1 y[n-1] - \ldots - a_N y[n-2] \tag{5.3}$$

The values $b_0, b_1, ..., b_M$ and $a_1, a_2, ..., a_N$ are the filter coefficients, and allow for the tuning of the digital filters up to the desired performance, alongside the order. If at least one $a$ coefficient is not null, then the calculation of the present output depends on the values of the previous outputs. This leads to the filter being an infinite-impulse-response (IIR); if all of the $a$ coefficients are null, then the filter is said to be a finite-impulse-response (FIR). While a IIR usually fulfils its specifications with a lower amount of coefficients, i.e., lower order, the FIR is always stable. Thus, for applications where memory and processing power are limited, IIR are the preferred choice. However, FIR filters can be designed to have a linear phase response, leading to lower signal distortion.

Since the limited processing power of the microprocessor chosen for this development is a heavy factor in the timeliness of the process being executed, it was decided to choose a IIR filter. The typical structure for a digital filter implementation can be found in fig. 5.3. This is called the Direct Form I, and is a common way to implement filters. It requires the storage of the past inputs and outputs on a buffer. It should also be noted that, with an increase in the filter order, not only does the size of the buffer increase, but the computational load increases as well.

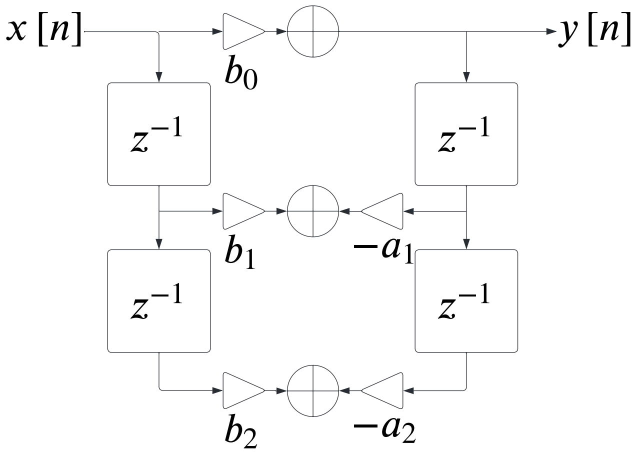


Figure 5.3: Direct Form I of a digital filter.

### 5.2.2 Filter Coefficients

To obtain the filter coefficients, two main points were considered: the filter order and the design type.

The sampling rate was set to 5 kHz, and the cut-off frequency at 120 Hz, a decade below the switching frequency.

Firstly, a comparison between a Butterworth and a Chebyshev type filters is shown in fig. 5.4. The coefficients for the filters were obtained with the help of the built-in functions of MATLAB, that return the coefficients based on the sampling and cut-off frequencies. Both filters were set to the same order, 2.

In terms of phase response, the Butterworth filter applies a slightly lower delay in comparison with the Chebyshev response. The main difference is in the passband, where the Butterworth shows greater gain stability. Since the signals to be filtered are not of a fixed frequency (as can be seen in figure 4.24), it was decided to use the Butterworth type filter, to keep the signals in the passband frequencies with an even gain.

Lastly, to understand the impact that the order had on the frequency response of the filter, a plot with Butterworth type filters, designed with different orders, is presented in fig. 5.5.

In the case of the magnitude, it can be noted that the attenuation slope is much greater with a higher order. However, as stated previously, it also leads to a higher computational burden. Taking into account the filter with order 2 achieves a -50 dB at the 1200 Hz frequency, a decade above the cut-off frequency, it was deemed that this order would be sufficient for the application. Furthermore, the order 2 filter achieves a lower amount of phase shift at the fundamental frequencies of the signals being filtered.

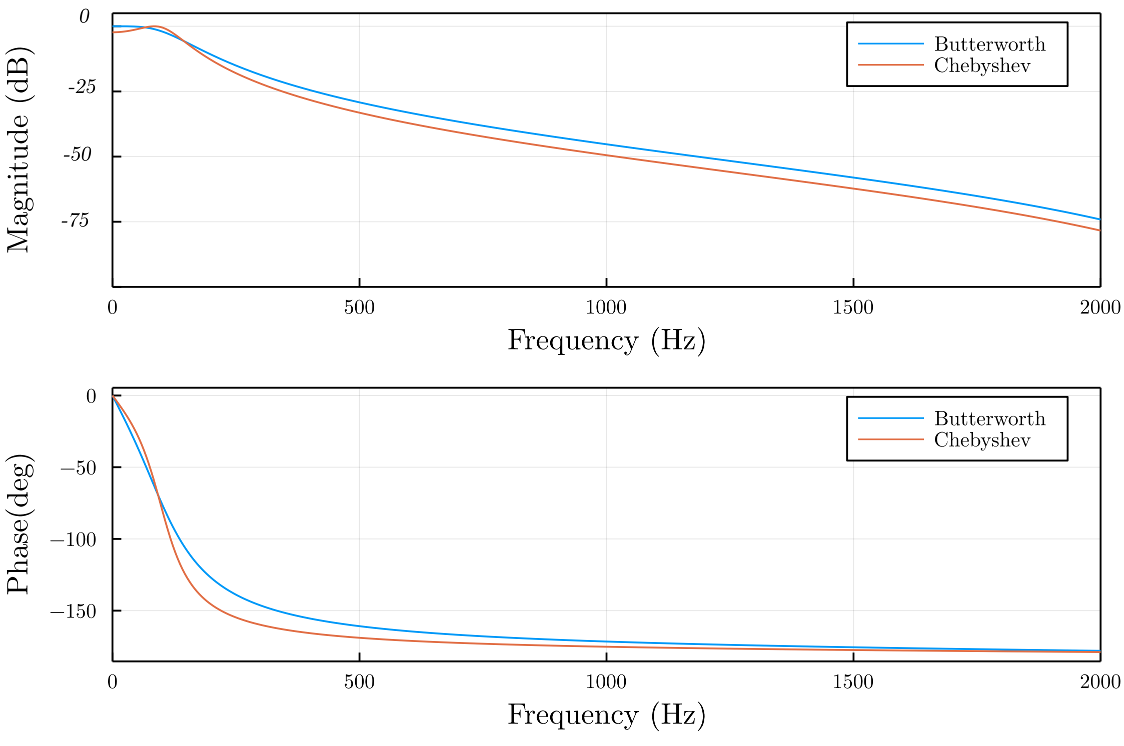


Figure 5.4: Comparison between Butterworth and Chebyshev Low-pass filters.

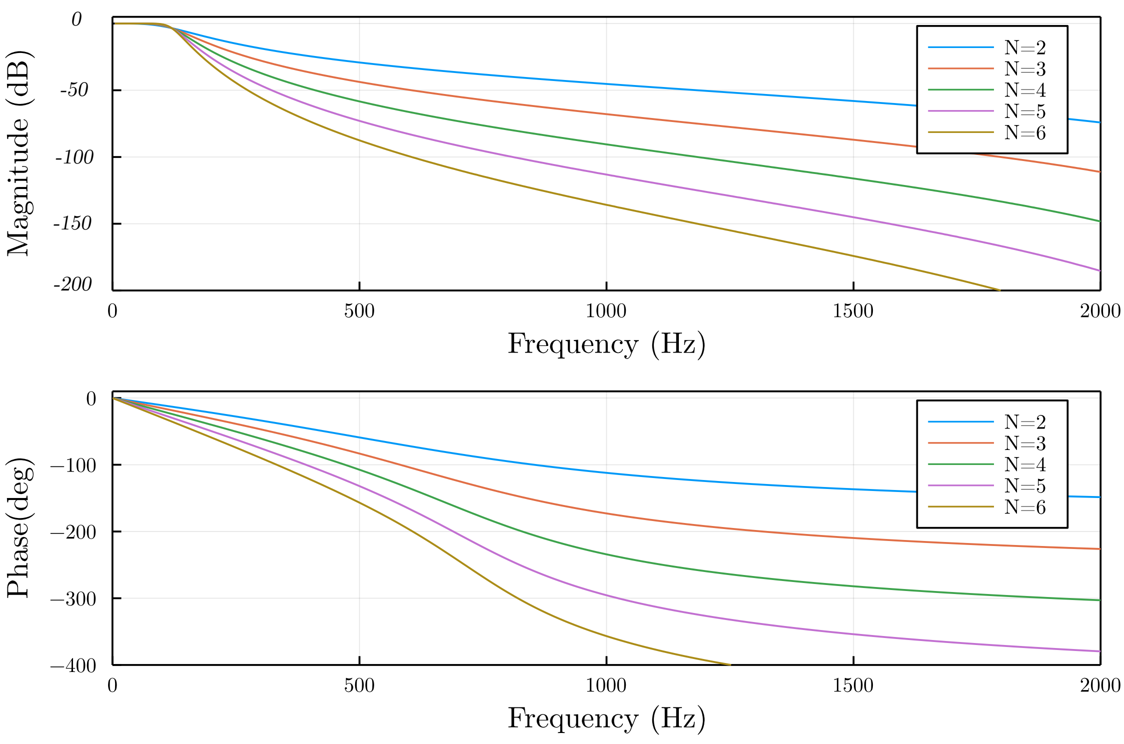


Figure 5.5: Impact of the different filter orders.

### 5.2.3 Interrupt Routine Configuration

In order to organise and scale all of the sub-routines present in the code developed, it was necessary to assign interrupts for each code block. At 5 kHz, there is the signal acquisition, filtering and the Park-Clarke transformations. At 2.5 kHz, the control sub-routine triggers, where the current control PI controllers are updated and the inverse Clarke to Park transformation is done. At 1.2 kHz, which is the switching frequency, a sub-routine tied to the event period match of the phase $U$ of the SVPWM output block is executed. This ensures that the SVPWM block is updated always at the beginning of its switching frequency, instead of possibly being updated in between switching cycles.

It should be noted that the acquisition cycle is double the frequency of the control cycle, and the control cycle is slightly over double frequency of the SVPWM updating cycle, assuring correct sampling, obeying to the Nyquist theorem.

The loops designed for the microcontroller can be schematically observed in figure 5.6, with the help of three flowcharts.

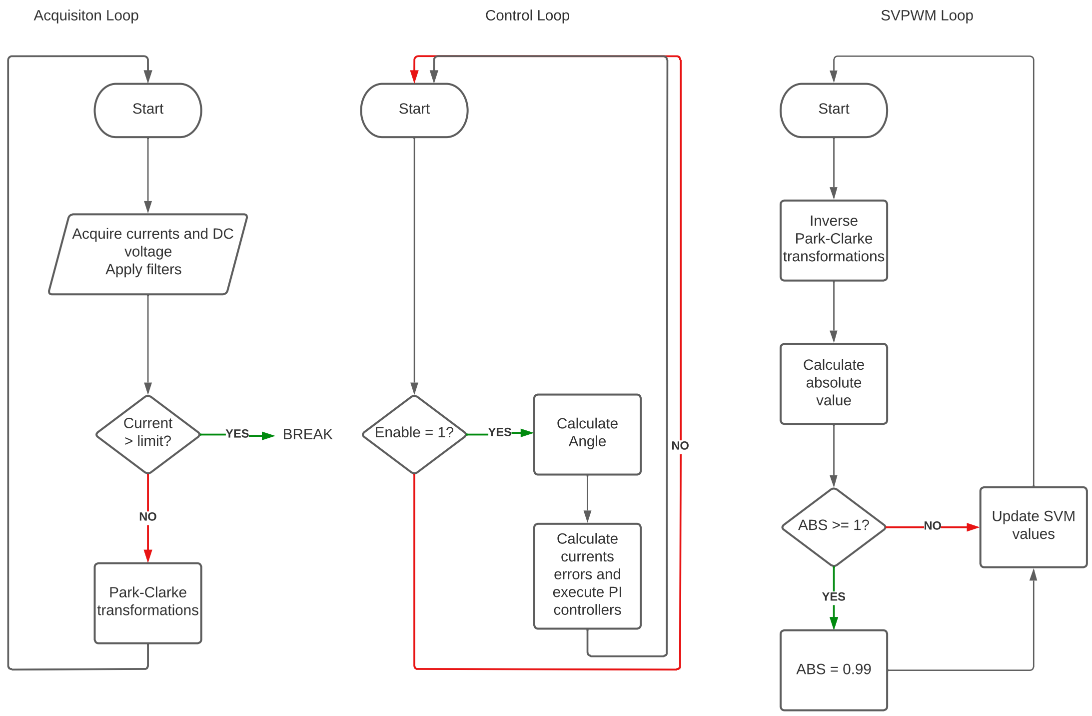


Figure 5.6: Flowcharts for each code loop.

## 5.3 Validation testing

This subsection will present the results obtained during the process of validating the code developed for the microcontroller.

### 5.3.1 PWM Test

With the help of an oscilloscope, it was possible to collect the waveforms of the outputs of the microcontroller. These consist of the three signals for the drivers of the IGBT. The inputs of the SVPWM block in the IDE are the amplitude and angle of the modulated signal. The amplitude was kept constant, while the angle oscillated between zero and $2\pi$ at a set frequency. The waveforms of a switching cycle can be observed in figure 5.7.

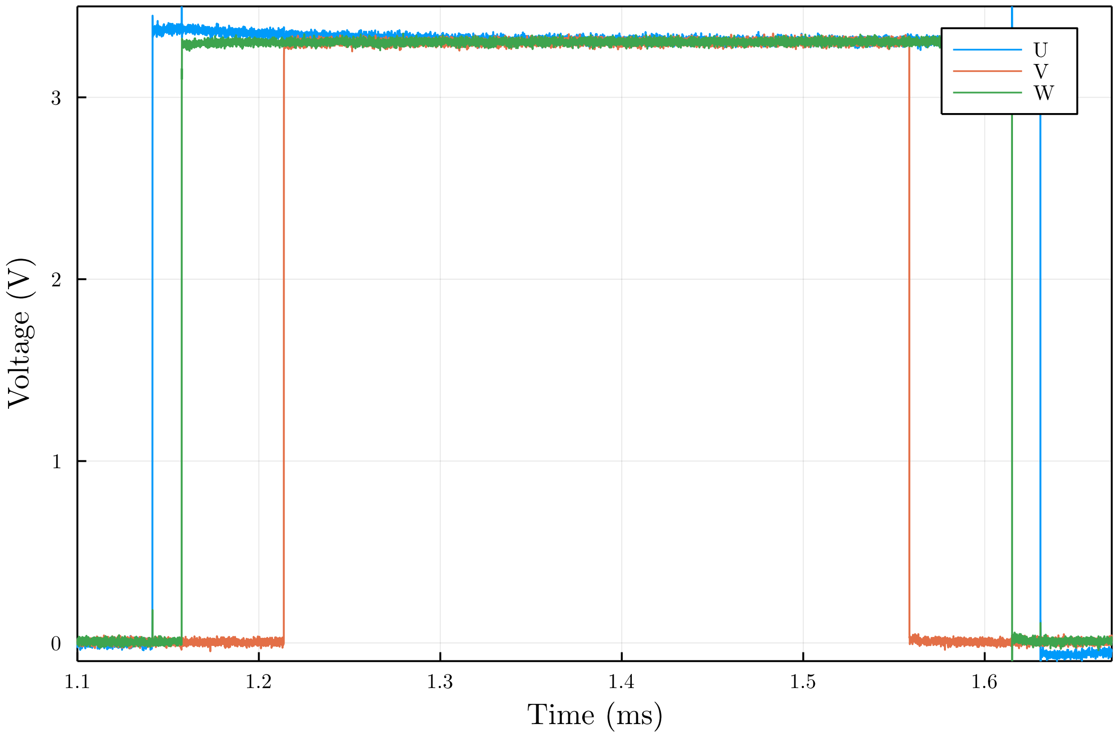


Figure 5.7: Three gates signals, outputs of the SVPWM block. Waveforms extracted with the help of an oscilloscope.

### 5.3.2 Acquisition Test

After connecting the three-phase inverter to a passive load, namely an RL load, the next step was to apply the PWM signals to the IGBTs, and test the acquisitions of the microcontroller's ADC. The code was arranged in a similar manner to the PWM test, with the objective of obtaining a 50 Hz current at the load. In figure 5.8, the filtered and unfiltered current can be observed. At 50 Hz, the filter should introduce a 36 degree delay to the sample, which is observed in the same figure. The waveform is also not attenuated.

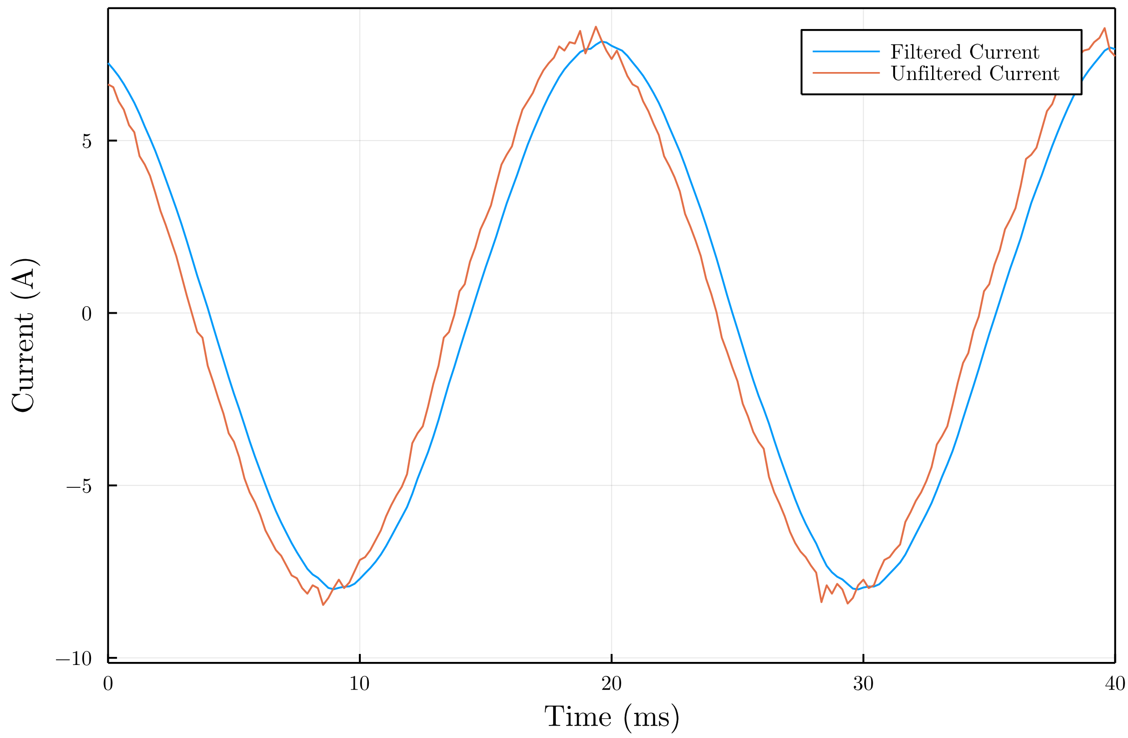


Figure 5.8: Filtered and Unfiltered currents.

### 5.3.3 Referential Transformations Test

Figure 5.9 shows the three-phase sinusoidal load currents and the correct Park-Clarke transformations applied to the filtered currents. These were done with the use of the same angle applied to the SVPWM block, at 50 Hz.

In fig. 5.10, the inverse Park transform test was performed. The *d*-*q* voltages were both set to 0.5 V, and the $\alpha - \beta$ voltages were obtained. They are phase-shifted 90 degrees, in agreement with the theory, and equal to the current results obtained in figure 5.9.

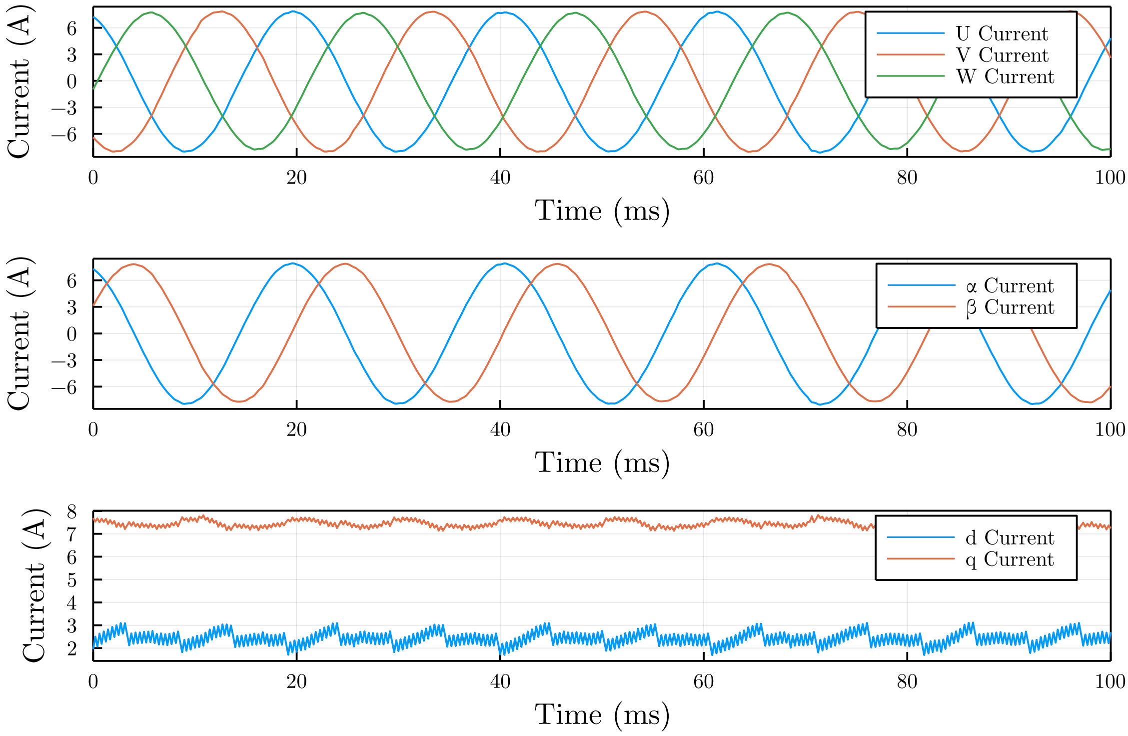


Figure 5.9: Park-Clarke transformation test.

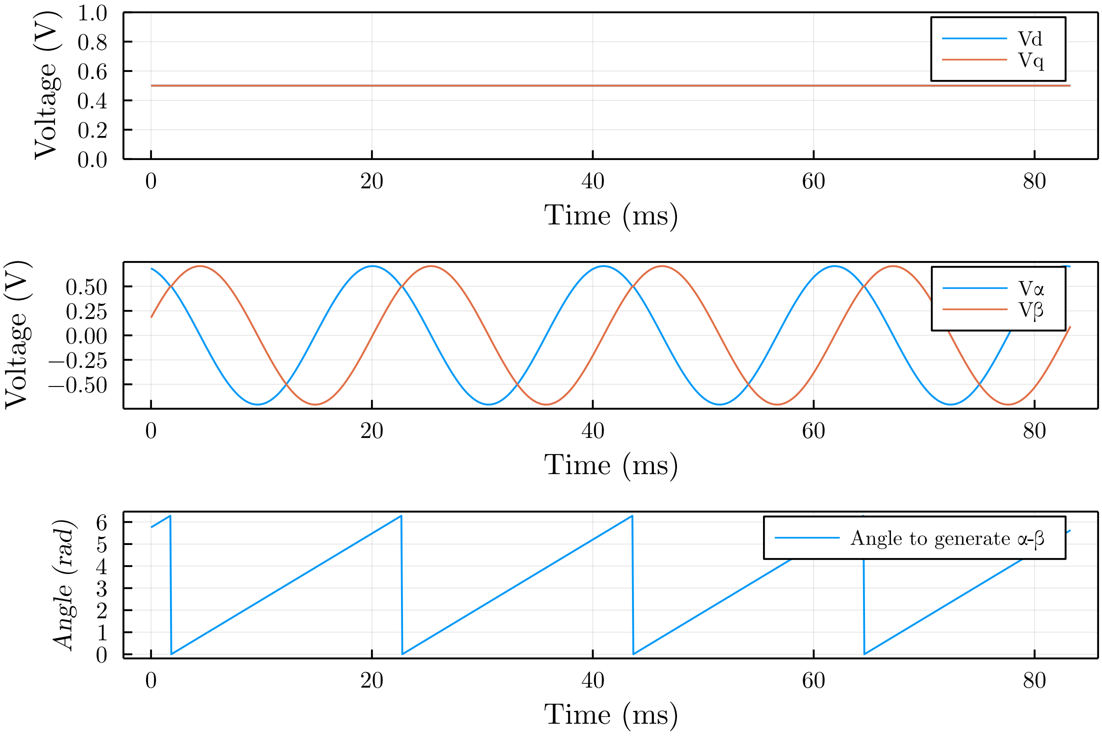


Figure 5.10: Inverse Park transformation test.

## 5.4 RL Load Current Control Results

A setup for a preliminary current control was concluded based on the diagram in fig. 5.11. In it, the DC voltage source was provided by a three-phase variable AC transformer, rectified by a three-phase diode bridge together with the DC link capacitors, as shown in fig. 5.2. The load consists of a 5 mH, 50 Hz inductance, in series with a 20 Ω resistor, in a three-phase configuration. The resistors' endpoints were connected in a star alignment. This allowed for a similar setup as an IM's stator, thus providing with a close validation, with a few differences which will be explained later in this subsection. In fig. 4.10, referring to the FOC schema developed, the angle used for the Park-Clarke transformations is estimated by use of the speed and rotor time constant. Since this load is passive, it was decided to use an angle with a constant frequency, set at the inductance's recommended one.

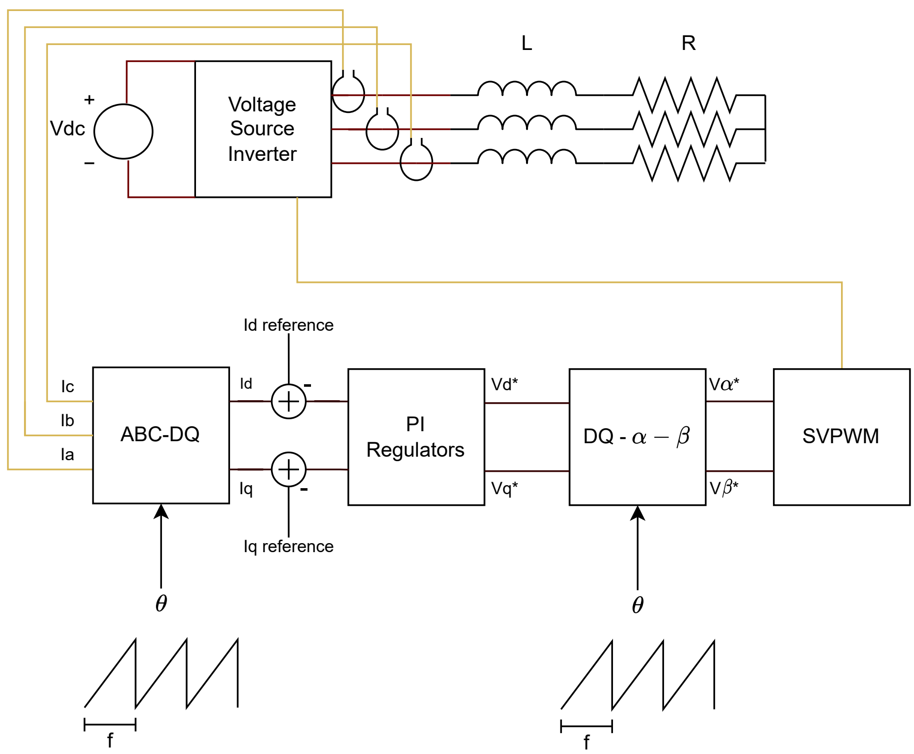


Figure 5.11: RL load current control setup.

After setting the *d*-*q* current references, the results are presented in figure 5.12. Afterwards, the next test consisted of controlling the current without the resistor in the load. Its results are in figure 5.13.

The results in fig. 5.12 show that the controllers were tuned for a slow response, in order to avoid any overshoot. The settling time of both currents is 2.9 s. The $I_q$ and $I_d$ currents follow their setpoints with good precision, whilst having a small ripple: 8.8 % in the case of the $I_q$, and 19.4 % in the case of $I_q$; these results can be attributed to two different factors: firstly, the low switching frequency of 1200 Hz; then, the noise present in the current sensors, since they are built

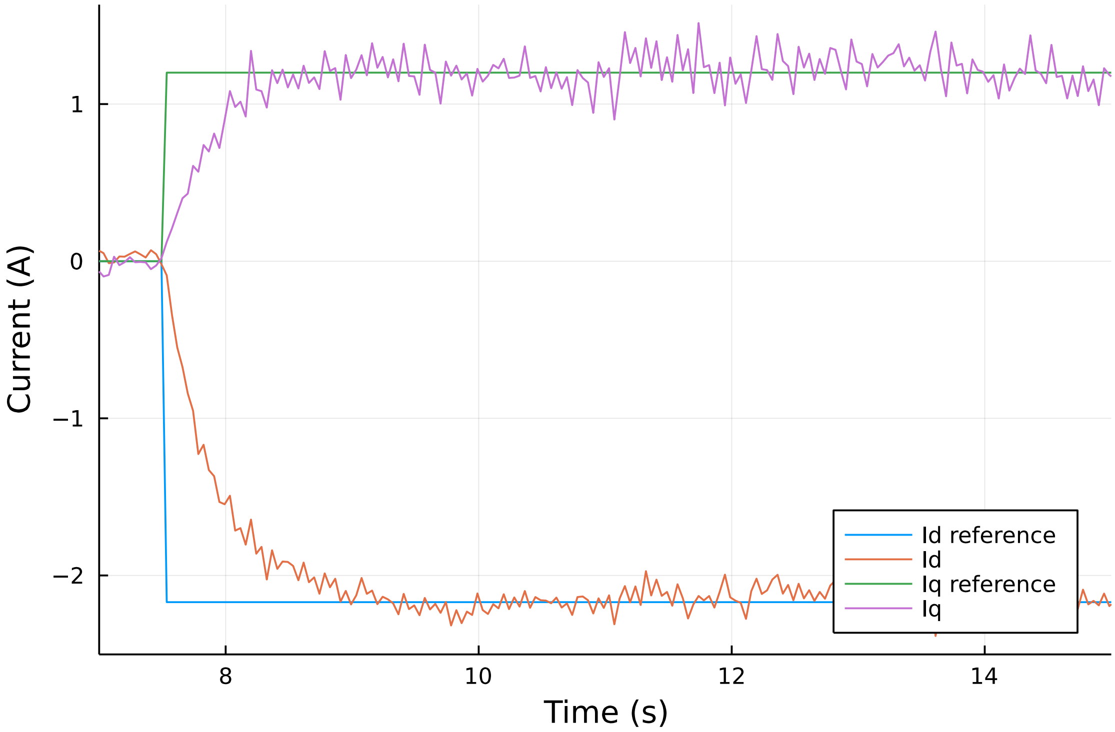


Figure 5.12: Current control in the *d*-*q* frame, in the RL load.

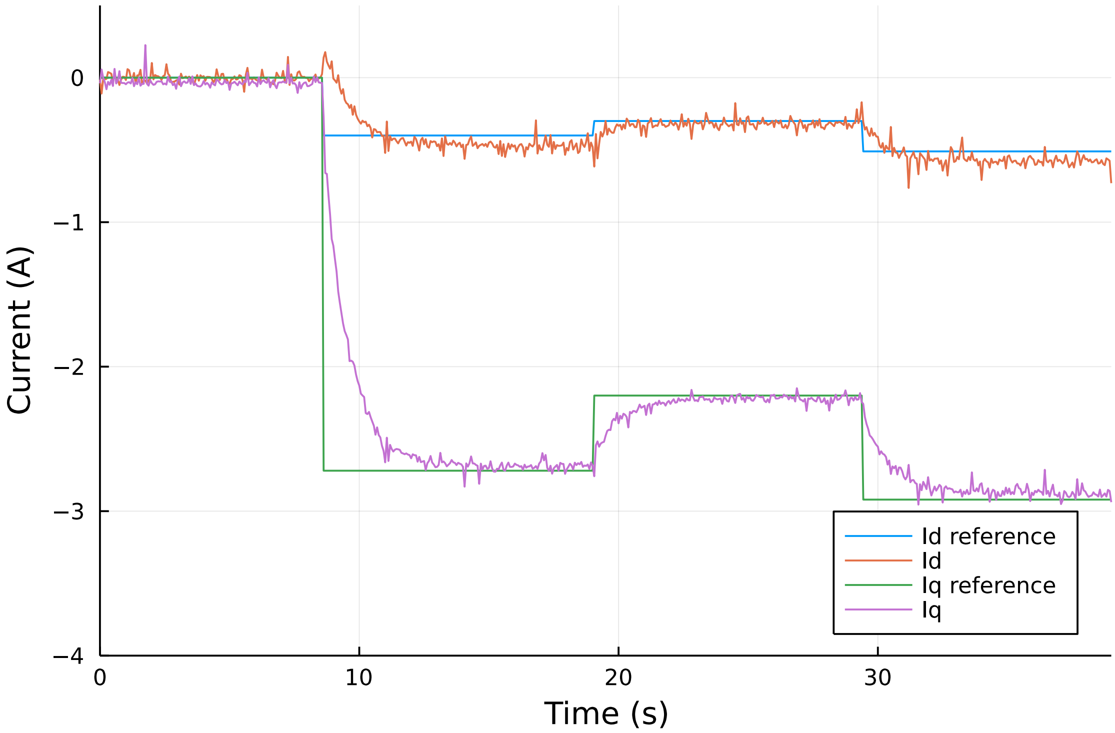


Figure 5.13: Current control in the *d*-*q* frame, in the L load.

for currents of 200 A rms and are measuring currents in the single digit range, gets amplified in the *d*-*q* frame.

Controlling the current with the load without the resistors enabled a further approximation of reality, since the resistance in the IM's stator is usually very low, as can be seen in table 4.1. Thus, the only resistance in the load would be resultant of the DC resistance of the inductors and their connectors. Moreover, it was also possible to obtain higher currents with the same DC voltage level. The controllers had to be tuned again to achieve a stable operation and good transient responses. Again, they were tuned for a slow response, in order to avoid any overshoot. The settling time, from zero to their first reference, is of 6 s. $I_q$ follows its references with great precision, whilst $I_d$ presents a steady-state error in some of its references, namely the first and third; the errors are of 13 % and 8.9 %, respectively.

Next, whilst the currents were stable, a variation was introduced in the DC link voltage to test the controllers' reaction to this step. Figure 5.14 shows the results. The controllers were further tuned to decrease the settling times.

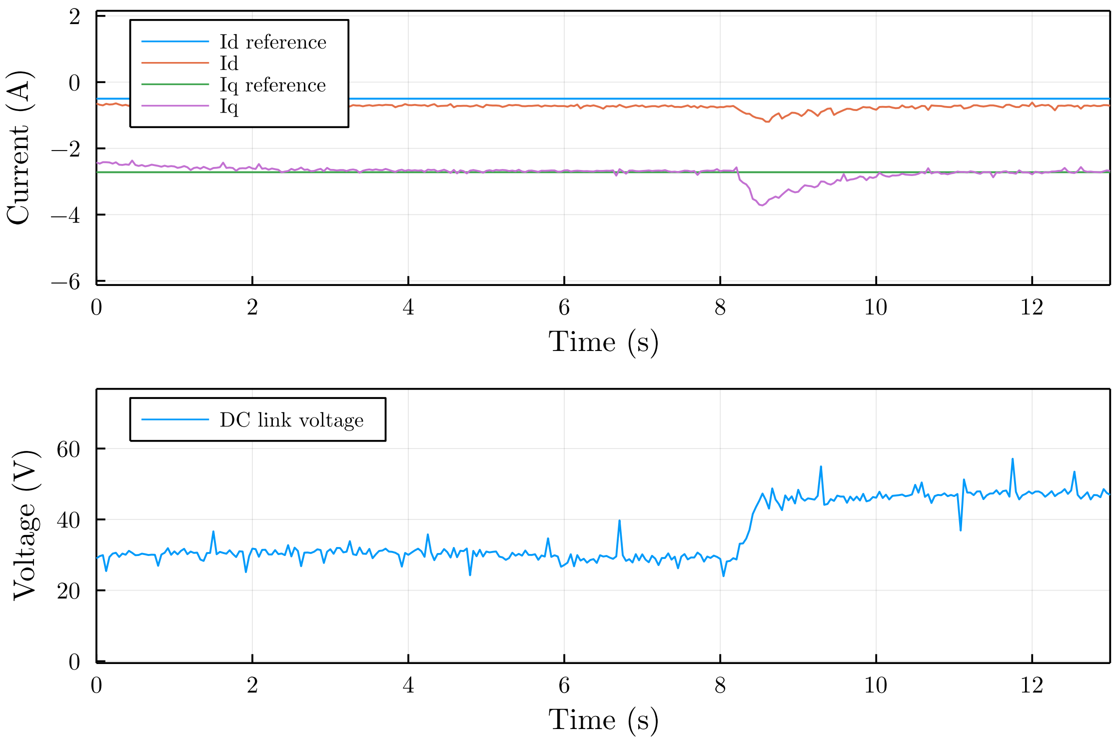


Figure 5.14: On top, the current references and their values. On the bottom, the DC link voltage value.

As can be noted, the controllers re-set the currents to their steady-state values quickly, with a settling time of 1.7 s, after a voltage change from 30 V to 50 V (which is equivalent to a 60 % increase). This implies that the control scheme developed is immune to voltage changes and the controllers react quickly to keep the system stable. It should be noted, however, that the $I_d$ current does not stabilise at its setpoint before the voltage change; however, it stabilises back to its previous steady-state value, after the voltage change.

## 5.5 Final Remarks

Through the developments detailed in this chapter, a preliminary experimental validation was executed. A three-phase current control of a load similar to an IM's stator was achieved, paving way to a full validation; this validation involves a plethora of steps namely the ADC configuration, filtering and referential transformations, all programmed in the chosen microcontroller.

# Chapter 6

# Conclusion

In this chapter, a final overview of the development of the dissertation is exposed. In it, the main results are analysed and discussed; afterwards, some suggestions for future developments are mentioned.

## 6.1 Final Remarks

Through the development of the dissertation works, a deep analysis of a TCU in a railway scenario was done. The first step was to define its requirements, taking into account the environment where it would operate. The first major challenge in the system was the low switching frequency imposed externally due to EMI requirements. This fact would directly impact the design of the control system of the IM.

The control scheme developed for a torque control of an IM, using FOC, is considered to have a good performance, taking into account the restrictions. The current control is precise and fast, whilst the torque control was tuned to be slower than the inner loop, achieving the goals set. The impact of the switching frequency was also shown, with great improvements in regards to the amount of torque ripples obtained with a higher frequency. These torque ripples, while undesirable, are a result of the motor's stator impedance values and the low switching frequency imposed. Additionally, since, in the end case, a train presents a high mass, and thus imposing a large moment of inertia on its movements, these ripples are smoothed out.

The FSM developed was proven to be adequate for its purpose of controlling the torque and current references, whilst the performance of the control scheme under regenerative braking was shown to be good, with fast response times and stable behaviour.

Through the thermal simulations, the thermal management solution was proven to be sufficient for the setup arranged. This tool can prove to be important in replicating the actual train setup.

Concerning the physical validations, taking into account that due to external factors out of the student's control (such as the global supply chains issue) a validation with a real IM was not possible, it was adequate to test the main parts of the controller developed with a similar setup. The microcontroller programming was proven to be ready for a scaled test; in fact, a preliminary study on current control in a three-phase RL load was achieved, with results considered to be positive.

## 6.2 Future Works

The main point where the dissertation could continue in the future is in the physical validation of the controller developed. This would not only make available the platform for testing the microcontroller programming, but also to able to demonstrate the control of the IM in different scenarios (such as acceleration at the nominal torque, coasting and braking).

The obtaining of the motor's parameters in agreement with the IEEE standards would be essential in revisiting the software modelling and simulation; it was shown that, with the preliminary torque control results, the ripples would decrease dramatically, thus it is expected that with the full model the results can further improve. Additionally, as can be seen in equation 4.6, the rotor flux angle estimation is deeply dependant on the rotor time constant. This, in its turn, can significantly deviate from its value due to a temperature rise in the machine. Therefore, the angle can suffer from precision errors in some operating conditions; it is suggested to develop a parameter estimation scheme, whose functionality can predict the IM's resistances value based on temperature readings.

Regarding the thermal studies, it would be interesting to develop a few key points: firstly, instead of the PSIM software, it could prove to be important to use a 3D modelling software with thermal validation capabilities, such as Altium. This can enable a deeper study in finding hotspots, determining an ideal heatsink size and/or shape and even validate different cooling options such as a water-loop with external radiators. Then, it can be relevant to, in the test bench, take temperature readings and compare these to the simulation results.

## Appendix A

# PSIM Schematic

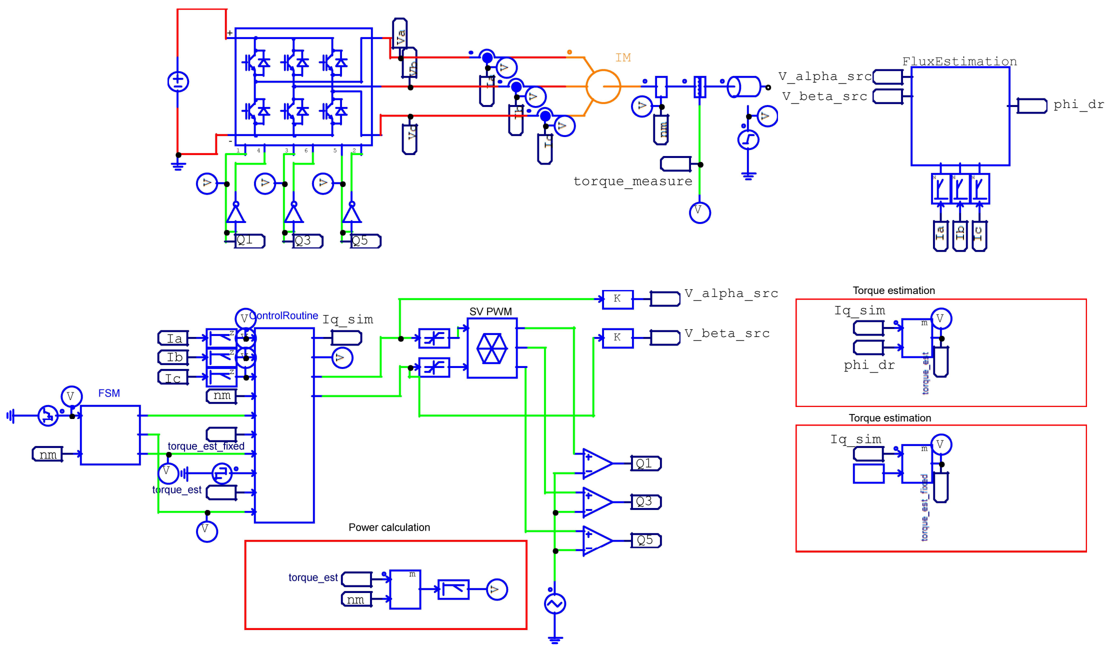


Figure A.1: PSIM software schematic developed.

## Appendix B

# Physical Setup

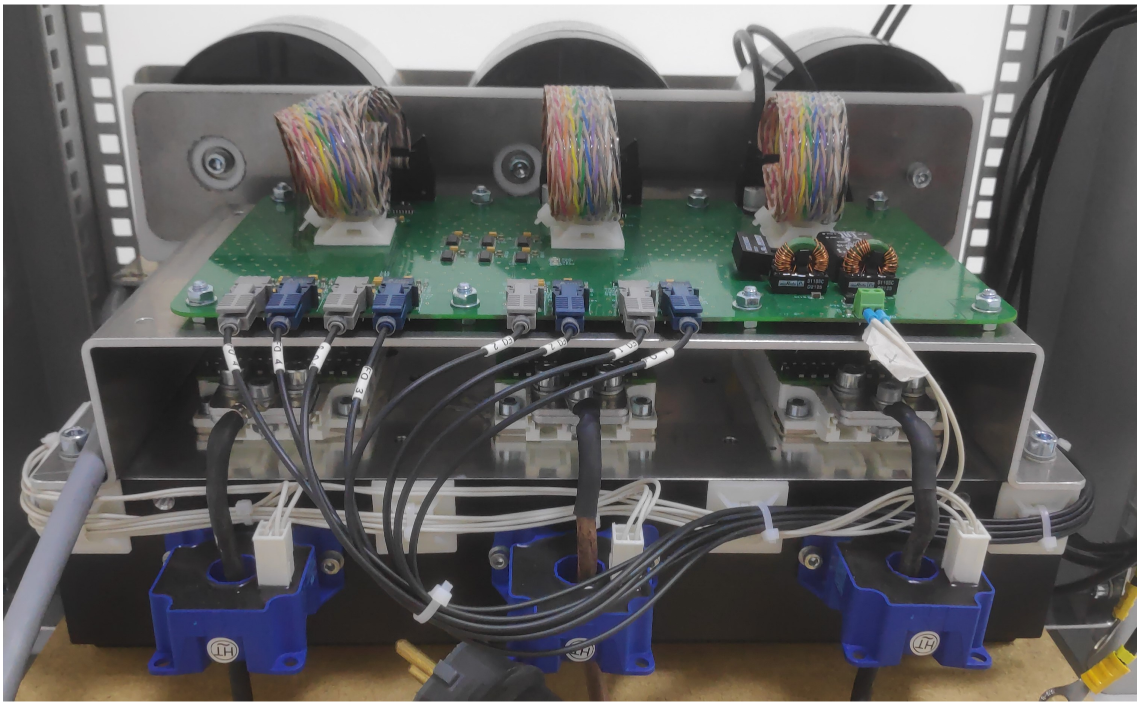

Figure B.1: Picture of the three-phase VSI, notably showing the current sensors, the IGBTs and their respective drives, and the PCB for handling the fiber optics communications.

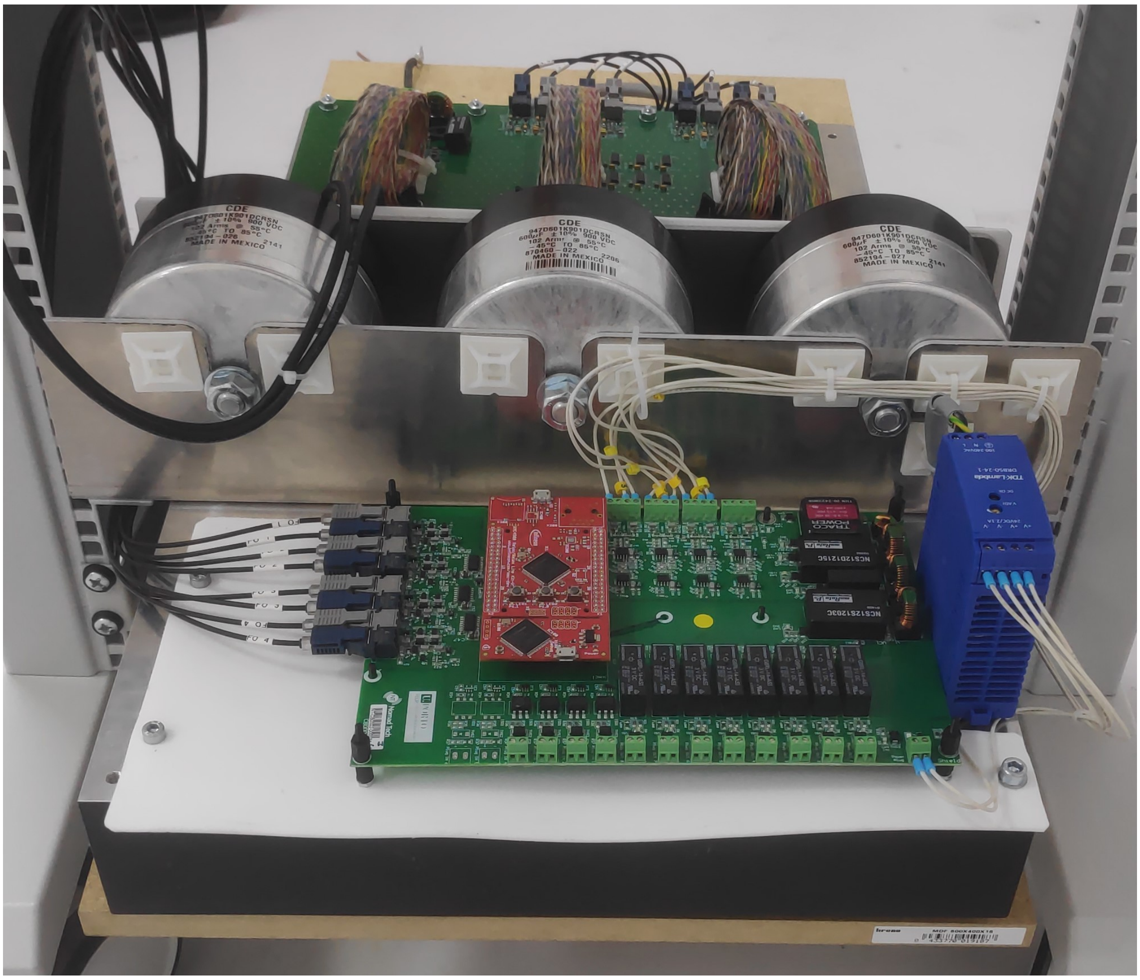

Figure B.2: Another angle of the three-phase VSI, showing the PCB where the acquisition processing is done, with the XMC 4500 microcontroller. The DC link capacitors can also be seen.

Figure B.3: Inductors used to test current control scheme.

# Bibliography


[1] D. Ronanki, S. A. Singh, and S. S. Williamson, "Comprehensive Topological Overview of Rolling Stock Architectures and Recent Trends in Electric Railway Traction Systems," *IEEE Transactions on Transportation Electrification*, vol. 3, no. 3, pp. 724–738, Sep. 2017, ISSN: 2332-7782. DOI: 10.1109/TTE.2017.2703583.

[2] S. Nategh, A. Boglietti, Y. Liu, *et al.*, "A Review on Different Aspects of Traction Motor Design for Railway Applications," *IEEE Transactions on Industry Applications*, vol. 56, no. 3, pp. 2148–2157, May 2020, ISSN: 1939-9367. DOI: 10.1109/TIA.2020.2968414.

[3] S. Nategh, D. Lindberg, R. Brammer, A. Boglietti, and O. Aglen, "Review and Trends in Traction Motor Design: Electromagnetic and Cooling System Layouts," in *2018 XIII International Conference on Electrical Machines (ICEM)*, Sep. 2018, pp. 2600–2606. DOI: 10.1109/ICELMACH.2018.8506817.

[4] *AGV (train)*, in *Wikipedia*, Aug. 1, 2021. [Online]. Available: https://en.wikipedia.org/w/index.php?title=AGV_(train)&oldid=1036576214 (visited on 12/16/2021).

[5] S. M. de Pancorbo, G. Ugalde, J. Poza, and A. Egea, "Comparative study between induction motor and Synchronous Reluctance Motor for electrical railway traction applications," in *2015 5th International Electric Drives Production Conference (EDPC)*, Sep. 2015, pp. 1–5. DOI: 10.1109/EDPC.2015.7323219.

[6] S. Nategh, A. Boglietti, Y. Liu, *et al.*, "A Review on Different Aspects of Traction Motor Design for Railway Applications," *IEEE Transactions on Industry Applications*, vol. 56, no. 3, pp. 2148–2157, May 2020, ISSN: 1939-9367. DOI: 10.1109/TIA.2020.2968414.

[7] V. K. Arun Shankar, S. Umashankar, S. Paramasivam, P. Sanjeevikumar, and K. Venkatesh, "Investigation of Direct Torque Control-Based Synchronous Reluctance Motor Drive for Pumping," in *Advances in Systems, Control and Automation: ETAEERE-2016*, A. Konkani, R. Bera, and S. Paul, Eds., Singapore: Springer Singapore, 2018, pp. 319–327, ISBN: 978-981-10-4762-6. DOI: 10.1007/978-981-10-4762-6_30.

[8] A. Fathy Abouzeid, J. M. Guerrero, A. Endemaño, *et al.*, "Control Strategies for Induction Motors in Railway Traction Applications," *Energies*, vol. 13, no. 3, 2020, ISSN: 1996-1073. DOI: 10.3390/en13030700.

[9] R. Ikeda, S. Yusya, and K. Kondo, "Study on Design Method for Increasing Power Density of Induction Motors for Electric Railway Vehicle Traction," in *2019 IEEE International Electric Machines Drives Conference (IEMDC)*, May 2019, pp. 1545–1550. DOI: 10.1109/IEMDC.2019.8785087.

[10] John Daniel. "Basic features of a steam locomotive." (2013), [Online]. Available: http://www.greatwestern.org.uk/basic12.htm (visited on 02/21/2022).

[11] K. Kondo, "Anti-slip control technologies for the railway vehicle traction," in *2012 IEEE Vehicle Power and Propulsion Conference*, Oct. 2012, pp. 1306–1311. DOI: 10.1109/VPPC.2012.6422493.

[12] C. Uyulan, M. Gokasan, and S. Bogosyan, "Re-adhesion control strategy based on the optimal slip velocity seeking method," *Journal of Modern Transportation*, vol. 26, no. 1, pp. 36–48, Mar. 1, 2018, ISSN: 2196-0577. DOI: 10.1007/s40534-018-0158-x.

[13] P. Pichlík and J. Zdeněk, "Overview of Slip Control Methods Used in Locomotives," *TRANSACTIONS ON ELECTRICAL ENGINEERING*, vol. 3, no. 2, pp. 38–43, 2 2014, ISSN: 1805-3386. [Online]. Available: https://ojs.cvut.cz/ojs/index.php/TEE/article/view/6465 (visited on 12/03/2021).

[14] D. Frylmark and Stefan Johnsson, "Automatic Slip Control for Railway Vehicles," Linkopings Universitet, Feb. 6, 2003.

[15] D. Hwang, "Anti-slip control system of Korean High-Speed Train," *WIT Transactions on The Built Environment*, vol. 50, 2000. DOI: 10.2495/CR000591.

[16] D. Ronanki, S. A. Singh, and S. S. Williamson, "Comprehensive topological overview of rolling stock architectures and recent trends in electric railway traction systems," *IEEE Transactions on Transportation Electrification*, vol. 3, no. 3, pp. 724–738, 2017. DOI: 10.1109/TTE.2017.2703583.

[17] T. Uzuka, "Trends in high-speed railways and the implications on power electronics and power devices," in *2011 IEEE 23rd International Symposium on Power Semiconductor Devices and ICs*, May 2011, pp. 6–9. DOI: 10.1109/ISPSD.2011.5890777.

[18] K. Ishikawa, K. Terasawa, T. Sakai, S. Sugimoto, and T. Nishino, "Development of Rolling Stock Inverters Using SiC," *Hitachi Review Vol. 66 (2017)*, vol. 2, p. 6,

[19] T. Sawa and T. Kume, "Motor drive technology - history and visions for the future," in *2004 IEEE 35th Annual Power Electronics Specialists Conference (IEEE Cat. No.04CH37551)*, vol. 1, Jun. 2004, 2–9 Vol.1. DOI: 10.1109/PESC.2004.1355703.

[20] Typhoon HIL. "DQ to ABC." (), [Online]. Available: https://www.typhoon-hil.com/documentation/typhoon-hil-software-manual/References/dq_to_abc.html (visited on 12/26/2021).

[21] Sang-Hoon Kim, *Electric Motor Control DC, AC, and BLDC Motors*, 1st. Elsevier, 2017, ISBN: 978-0-12-812138-2.

[22] David Irwin and Bogdan Wilamowski, *Power Electronics and Motor Drives*, 1st. CRC Press, 2011, ISBN: 978-1-4398-0285-4.

[23] S. K. Kakodia and G. Dynamina, "A Comparative Study of DFOC and IFOC for IM Drive," in *2020 First IEEE International Conference on Measurement, Instrumentation, Control and Automation (ICMICA)*, Jun. 2020, pp. 1–5. DOI: 10.1109/ICMICA48462.2020.9242909.

[24] H. Maghfiroh, C. Hermanu, and M. Nizam, "Sensorless Control of Railway Traction Motor in The Energy Point of View," in *2019 6th International Conference on Electric Vehicular Technology (ICEVT)*, Nov. 2019, pp. 267–271. DOI: 10.1109/ICEVT48285.2019.8993990.

[25] Y. Zhang, H. Yang, and B. Xia, "Model-Predictive Control of Induction Motor Drives: Torque Control Versus Flux Control," *IEEE Transactions on Industry Applications*, vol. 52, no. 5, pp. 4050–4060, Sep. 2016, ISSN: 1939-9367. DOI: 10.1109/TIA.2016.2582796.

[26] M. Zaky, M. Khater, H. Yasin, and S. Shokralla, "Review of different speed estimation schemes for sensorless induction motor drives," *JEE*, vol. 8, pp. 102–140, Jan. 1, 2008.

[27] K. Zhao and X. You, "Speed estimation of induction motor using modified voltage model flux estimation," in *2009 IEEE 6th International Power Electronics and Motion Control Conference*, May 2009, pp. 1979–1982. DOI: 10.1109/IPEMC.2009.5157719.

[28] A. R. Haron and N. R. N. Idris, "Simulation of MRAS-based Speed Sensorless Estimation of Induction Motor Drives using MATLAB/SIMULINK," in *2006 IEEE International Power and Energy Conference*, Nov. 2006, pp. 411–415. DOI: 10.1109/PECON.2006.346686.

[29] M. Yano and M. Iwahori, "Transition from slip-frequency control to vector control for induction motor drives of traction applications in Japan," in *The Fifth International Conference on Power Electronics and Drive Systems, 2003. PEDS 2003.*, vol. 2, Nov. 2003, 1246–1251 Vol.2. DOI: 10.1109/PEDS.2003.1283156.

[30] T. M. M. F. Pereira, "Design of a PMSM Drive for an Electric Vehicle Application," Oct. 14, 2016. [Online]. Available: https://repositorio-aberto.up.pt/handle/10216/87477 (visited on 12/29/2021).

[31] F. Sevilmiş and H. Karaca, "Simulation and analysis of SVPWM based VSI for wind energy systems," in *Proceedings of the 2014 6th International Conference on Electronics, Computers and Artificial Intelligence (ECAI)*, Oct. 2014, pp. 73–78. DOI: 10.1109/ECAI.2014.7090151.

[32] A. Duarte. "O renascimento da CP," Escola Portuguesa. (Dec. 31, 2020), [Online]. Available: https://escolapt.wordpress.com/2020/12/31/o-renascimento-da-cp/ (visited on 06/16/2022).

[33] A. Fitzgerald, A. E. Fitzgerald, C. Kingsley, and S. Umans, *Electric Machinery*. McGraw-Hill Companies,Incorporated, 2003, 736 pp., ISBN: 978-0-07-366009-7. Google Books: YBKk4kWSle0C.

[34] A. Nied, J. de Oliveira, R. de Farias Campos, R. P. Dias, and L. C. de Souza Marques, "Soft starting of induction motor with torque control," *IEEE Transactions on Industry Applications*, vol. 46, no. 3, pp. 1002–1010, 2010. DOI: 10.1109/TIA.2010.2045335.

[35] Rollingstone. "E-cracked Solutions: Implementation of Space Vector Modulation (SVM) Inverter," e-cracked Solutions. (Jul. 2, 2011), [Online]. Available: http://electrotech4u.blogspot.com/2011/07/implementation-of-space-vector.html (visited on 04/08/2022).

[36] Simon Iwnicki, *Handbook of Railway Vehicle Dynamics*, 2nd ed. CRC Press, 2019, ISBN: ISBN9780429469398.

[37] P. Lukaszewicz, "Energy Consumption and Running Time for Trains : Modelling of running resistance and driver behaviour based on full scale testing," 2001. [Online]. Available: http://urn.kb.se/resolve?urn=urn:nbn:se:kth:diva-3185 (visited on 04/20/2022).

[38] V. Morais, "Tools and Strategies for Power Flow Management in Smart Railways," Jul. 22, 2021. DOI: 10.13140/RG.2.2.33336.88327.

[39] "TG 450HF17M1-S300 Dynex Semiconductor." (), [Online]. Available: https://www.semic.info/tg-450hf17m1-s300-7/ (visited on 06/17/2022).

[40] "Driving SiC FETs and IGBTs." (), [Online]. Available: https://www.powersystemsdesign.com/articles/driving-sic-fets-and-igbts/32/10776 (visited on 04/21/2022).

[41] Y. Liu, L. Tolbert, P. Kritprajun, *et al.*, "Aging Effect Analysis of PV Inverter Semiconductors for Ancillary Services Support," *IEEE Open Journal of Industry Applications*, vol. 1, pp. 157–170, Jan. 1, 2020. DOI: 10.1109/OJIA.2020.3028647.

[42] "2SP0115T2A0-17 | Power Integrations, Inc." (), [Online]. Available: https://www.power.com/products/scale-2-plug-and-play-drivers/2sp0115t/2sp0115t2a0-17 (visited on 06/14/2022).